Hypothesis-free detection of genome-changing events in pedigree sequencing

Kiran V Garimella
Green Templeton College
University of Oxford

A thesis submitted for the degree of
Doctor of Philosophy

Michaelmas 2015

Dedication

Acknowledgements

Acknowledgements

Abstract

In high-diversity populations, a complete accounting of *de novo* mutations can be difficult to obtain. Most analyses involve alignment of genomic reads to a reference genome, but if the haplotypic background upon which a mutation occurs is absent, events can be easily missed (as reads have nowhere to align) and false-positives may abound (as the aligner forces the reads to align elsewhere). In this thesis, I describe methods for *de novo* mutation discovery and genotyping based on a so-called "pedigree graph" - a de Bruijn graph where all available sequencing data (trusted and untrusted data alike) is represented. I constrain genotyping efforts to locations containing "novel kmers" - sequence present in the child but absent from the parents. I then apply Dijkstra's shortest path algorithm to perform the genotyping, even in the presence of sequencing error. In simulation, this approach provides a vastly more sensitive and specific set of *de novo* variants than traditional methods.

Contents

List of Figures

List of Tables

List of Algorithms

1 Motivation

1.1 Introduction

Increasingly frequent reports of antimicrobial resistance and immune escape have lead to worries about a "post-antibiotic era": a time when common pathogens no longer respond to drugs and for which no effective vaccines exist.[1] For influenza A, a single serine to asparagine amino acid substitution (S31N) alters the properties of the M_2 ion channel,[2] interferes with the action of the adamantane class of antiviral drugs, and has reached fixation in the population.[3] In *Mycobacterium tuberculosis*, a four-year *in vitro* drug challenge experiment on nine drug-susceptible isolates from a single patient demonstrated the strain could acquire resistance to nearly all first-line and most second-line drugs through just 12 single nucleotide polymorphisms (SNPs).[4] *Staphylococcus aureus* is the most common cause of post-operative infection worldwide and is increasingly unresponsive to β-lactam treatment and drugs in the penicillin group (methicillin, dicloxacillin, nafcillin, oxacillin, etc.). Sequencing of methicillin-susceptible (MSSA) in the penicillin group and resistant (MRSA)[1] strains reveals the acquisition of resistance genes via mobile genetic elements and horizontally transferred genomic islands (e.g. the SCC*mec* cassette chromosome upon which the methicillin and other β-lactam antibiotic resistance gene, *mecA*, resides).[5]

De novo mutations (DNM), genomic variants arising anew in a sample and absent from progenitors, underlie many medically relevant pathogenic phenotypes. The examples above all involve virulence phenotypes arising from spontaneous point mutations, structural variants, or horizontal gene transfer - all mutational methods that occur outside methods of traditional reproduction. They are critical tools for pathogenic evolution and come in myriad forms.

[1] The term "methicillin resistant" is used in the literature, though it is taken to mean all drugs - including more stable variants of methicillin used in modern clinical practice

Table 1.1: Phenotypes of *P. falciparum* isolates used for genetic crosses.

	3D7	HB3	DD2	7G8	GB4	803
pyrimethamine sensitivity	-	+				
chloroquine sensitivity		+	-			
infects mosquitoes easily		+	-			
infects *Aotus nancymaae*				-	+	-
artemisinin sensitivity					+	-

1.2 *De novo mutations (DNMs) in Plasmodium falciparum*

Experimental crosses of *Plasmodium falciparum* parasites, the causative agent for the most deadly form of malaria, have enabled the discovery of a number of inherited and *de novo* virulence factors. The contrasting phenotypes for various strains of *P. falciparum* are listed in Table 1.1. For inherited factors, crossing of the pyrimethamine-resistant 3D7 and sensitive HB3 strains[6] revealed a nonsynoymous point mutation in the *dhfr-ts*[2] gene, inhibiting binding of (and thus conferring resistance to) the drug.[7] Analysis of the HB3 x DD2 cross,[8] the latter of which is resistant to chloroquine, localized the determinant to a previously undetected gene on chromosome 7, labelled *pfcrt*[3], a member of a new family of transporters. Additional investigation into differences in mosquito infection efficacy revealed down-regulation of the *pfmdv-1*[4] gene,[9,10] disruption of which results in marked reduction of mature and functional male gametocytes.

For uninherited factors, cytoadherence and antigenic properties of parasites facilitate evasion from host immune attack, and can differ substantially from the properties of their progenitors. In 2000, Freitas-Junior *et al.* showed that some 3D7 x HB3, HB3 x DD2, and HB3 x HB3 progeny harbored non-parental forms of subtelomeric *var* genes, key members of an antigenic gene family.[11] These altered forms were likely generated during mitosis by non-allelic homologous recombination[5] (NAHR) of telomeres from two different chromosomes.[12] The resulting genes are novel, functional, and never before observed by the host immune system.

These DNMs are critical tools for malaria to evade drug and immune pressure. NAHR can further diversify a pathogen's antigenic repertoire, enabling continued evasion of immunological actors. Duplications of a transporter gene may enable faster drug clearance in a parasite, thus conferring resistance. Spontaneous point mutations may alter the binding site of a drug to a receptor, thus conferring immunity.

[2] dihydrofolate reductase-thymidylate synthase
[3] *P. falciparum* chloroquine resistance transporter
[4] *P. falciparum* male gametocyte development gene 1
[5] sometimes referred to as "ectopic" (aberrant) recombination in the literature

1.2.1 *A reference-based approach for DNM discovery and genotyping*

With the advent of sequencing technologies, it is now straightforward to discover many DNMs. Long reads (~500 bp) from the first-generation sequencing technology, Sanger sequencing, can be stitched together *in silico* by considering the overlaps of sequences generated from many copies of the genome.[13] This has enabled the reconstructions of full-length genomes and subsequent gene annotations for a single representative (or "reference") individual in a population. Second-generation sequencing is leveraging economies of scale to reduce sequencing costs by several orders of magnitude.[14] The reads it produces are shorter (~100 bp) and more error-prone, but billions of them can be produced quickly. Like the long reads, the short read data can also be assembled into a new genome, albeit with more errors and gaps, owing to the difficulty of overcoming large repetitive regions with short genomic fragments.[15] Alternatively, assuming the sequence for the reference genome and a new individual are highly similar, it is far more common (and computationally more efficient) to align the reads to the reference.[16] String matching algorithms that allow mismatches, insertion, and deletions to appear in the alignments allow millions of sequnced reads to be placed on the reference genome quickly. Separate tools can then examine the alignments, looking for the presence of non-reference alleles, and using statistical approaches to call and genotype variants with high accuracy.[17]

Variant calling software has been successfully applied to many sequencing datasets for the discovery of DNMs. These variant callsets have provided insight into the development of drug resistance,[18] the genetic architecture of some common diseases,[19] and mutational rates in humans and chimpanzees with a strong paternal age effect.[20–23] Many groups have released sophisticated software packages to facilitate these analyses and detailed instructions on their use.[24,25]

1.2.2 *A reference-free approach for assessing DNM sensitivity*

Specificity and sensitivity are crucial metrics to consider for any variant callset. There are many approaches to establishing the specificity of a DNM callset. For select variants (typically on the order of ~100 variants from a callset), Sanger sequencing, Sequenom assays, and even targeted third-generation sequencing (i.e. PacBio sequencing, which can generate reads up to ~50,000 bp as of this writing) have been used successfully to validate mutations. Establishing sensitivity is much more difficult. In theory, one would need complete and error-free reference genomes for both parents and each child in which the mutation calls are made. Except for the smallest genomes, such an approach is prohibitively expensive.

Instead, it may be possible to establish the sensitivity of the reference-based protocol by considering how DNMs alter the genome of a sample with respect to its progenitors. Consider a site where a DNM - say, a single SNP - has occurred, as depicted in Figure 1.1. Although a single base of the genome has been altered, when the genome is divided into fixed-length words of length k, or "kmers", we find k kmers that are present in the child but absent in the parents. In this manner, DNMs can be considered generators of "novel" kmers - kmers present in the child but absent in the parents. These kmers can be used as a signal to indicate the presence of a *de novo* variant. By choosing k to be reasonably large so as to avoid analyzing short sequences that pervade the genome (half to two-thirds the length of a read will suffice), we can simply count continuous stretches of novel kmers as a proxy for the number of DNMs.

This approach gives us a powerful, reference-free mechanism to verify the results of the reference-based analysis. Sequencing of the whole genome is independent of any reference sequence that may already exist for the sample, and given sufficient coverage (Table 1.2 shows the requirements, assuming 76 bp reads and a 23 megabase genome), the raw data from a sequencing experiment should contain the full set of DNM-generated novel kmers, regardless of any mapping issues.[26] Taking the reads that map, calling *de novo* variants, and extracting the novel kmers from the immediate vicinity should theoretically reproduce that set. Comparing the expected (reference-free) set to the observed (reference-based) kmer set should thus provide the sought sensitivity measure.

1.3 DNM sensitivity of the reference-based approach

We now demonstrate these ideas on real data sets that will be used throughout this dissertation: experimental crosses between malaria parasites (*Plasmodium falciparum*).

The datasets that we'll be referring to in this work are summarized in Table 1.3. For simplicity, we shall focus on the samples from the 3D7xHB3 cross.

1.3.1 Data processing

We first generated the list of expected novel kmers by processing the raw sequencing data for each sample with the *de novo* assembly software, Cortex[27] at $k = 47$, standard settings for other parameters, and no error cleaning. We produced the initial list of putative novel kmers by selecting kmers present in a child but absent in both parents. We further produced a "confident" list of novel kmers by imposing a kmer coverage threshold, automatically determined by a custom algorithm designed to find a local minimum on the LOESS regression of the coverage distribution, as shown in Figure 1.2. Finally, we produce a "trusted" list of novel kmers by removing kmers originating from possible

Table 1.2: Theoretical percentage of the genome recovered at a target depth of coverage.

coverage	numReads	numNucleotides	pctGenome
1	302631	2.3e+07	63.21
2	605263	4.6e+07	86.47
3	907894	6.9e+07	95.02
4	1210526	9.2e+07	98.17
5	1513157	1.15e+08	99.33
6	1815789	1.38e+08	99.75
7	2118421	1.61e+08	99.91
8	2421052	1.84e+08	99.97
9	2723684	2.07e+08	99.99
10	3026315	2.3e+08	100.00
11	3328947	2.53e+08	100.00
12	3631578	2.76e+08	100.00
13	3934210	2.99e+08	100.00
14	4236842	3.22e+08	100.00
15	4539473	3.45e+08	100.00
16	4842105	3.68e+08	100.00
17	5144736	3.91e+08	100.00
18	5447368	4.14e+08	100.00
19	5750000	4.37e+08	100.00
20	6052631	4.6e+08	100.00

Table 1.3: The *P. falciparum* datasets that will be referred to throughout this work.

	3D7xHB3	HB3xDD2	7G8xGB4	803xGB4
progeny	17	30	38	29
read length	76	76	76	100
fragment size	300 ± 30	248 ± 46	294 ± 17	224 ± 8
coverage	105 ± 34	102 ± 48	105 ± 30	176 ± 54

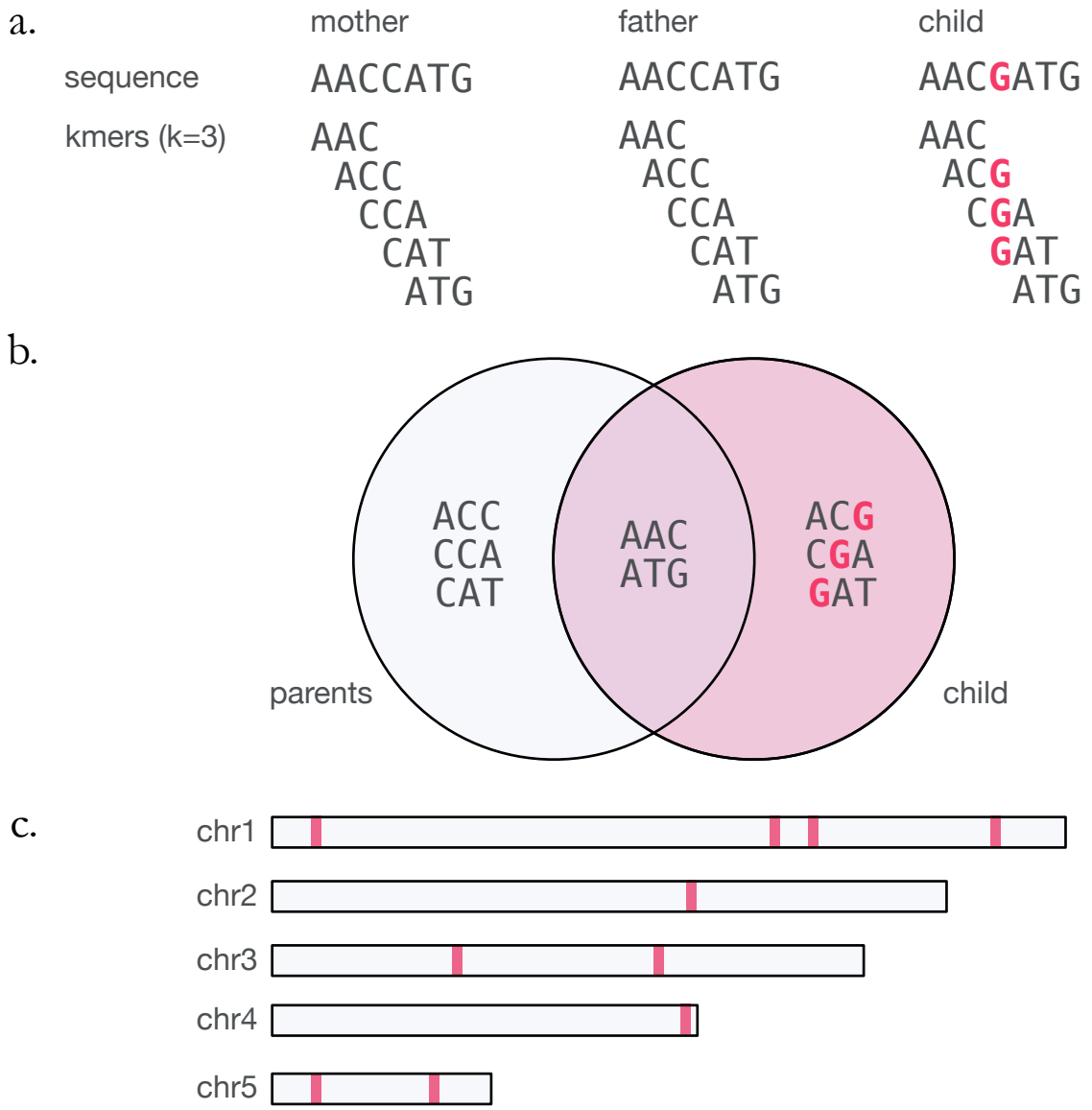

Figure 1.1: a. Parental and child sequences at the site of a *de novo* mutation, and the kmers generated at $k = 3$. b. The resulting Venn diagram of kmers found exclusively in the parents, the child, or common to both. c. Novel kmers found around the genome indicate the presence of a *de novo* mutation.

contaminants, as determined by performing a BLAST search on the confident list and removing all non-*Plasmodium* hits. These steps ensure that the list of trusted novel kmers is very restrictive.

We aligned each sample's reads to the PlasmoDB 9.0 release of the *Plasmodium falciparum* genome[28,29] using BWA-MEM.[30] We followed data processing guidelines as specified in the Genome Analysis Toolkit (GATK) best-practices documentation,[24,31] flagging

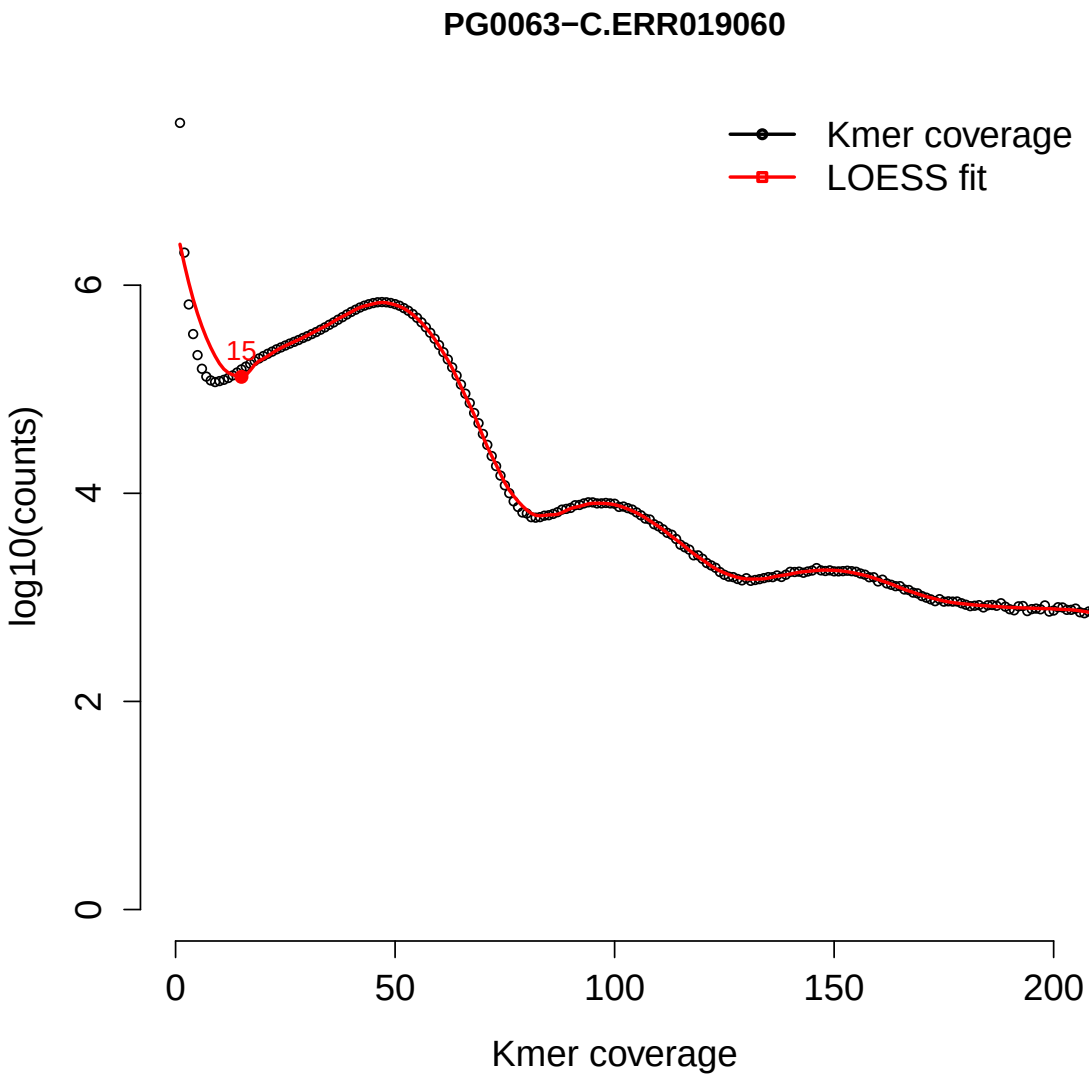

Figure 1.2: Kmer coverage distribution for a single 3D7xHB3 progeny, PG0063-C. Red line indicates non-parametric LOESS fit upon which the local minimum is detected.

duplicate reads so that they are ignored downstream, and recalibrating base quality scores using the MalariaGen data release on the crosses as a truth set.[?] As recent guidance by the authors indicates the GATK's variant calling software has internalized the local indel realignment functionality, we opted to forego running this step separately. We called variants across all 18 samples (parents and progeny) simultaneously using the GATK's HaplotypeCaller with standard settings and a ploidy of 1.

A complete and perfect variant callset details the alterations that must be performed on the reference sequence in order to generate the genome of the sequenced sample. Unfortunately, it is typically not possible to obtain a perfectly sensitive and specific callset.

False positives and false negatives proximal to true positives may interfere with our ability to generate the true underlying haplotype sequence. To bypass this problem, we did not filter the variant callset. Instead, we combinatorically generate all possible subsets of variants found within 100 bp of each other using a recursive strategy to leave single elements out of a given set of kmers, presented in Algorithm 1. This will certainly generate vastly more kmers than truly exist in the sample's genome. However, as we are only interested in verifying that the variant-induced kmers are present in our trusted novel kmer set, this approach has the benefit of providing maximum sensitivity.

Algorithm 1 Given a set of variants, generate all possible subsets of variants

```
1:  function generateAllPossibleSubsets(variants)
2:      loos ← []
3:      for i ← 0 to length(variants) do
4:          loo ← []
5:          for j ← 0 to length(variants) do
6:              if i ≠ j then
7:                  loo.add(variants[j])
8:          if loo.size() ≥ 0 then
9:              loos.add(loo)
10:         if loo.size() ≥ 1 then
11:             generateAllPossibleSubsets(loo)
12:     return loos
```

1.3.2 *Results*

Figure 1.3 shows the results of our reference-based vs reference-free analysis. Per sample, our restrictive reference-free analysis has generated hundreds of trusted novel kmers to explain. However, the reference-based analysis recapitulates only a fraction of these - only about 13% on average.

Attempting to explain where these missing kmers have gone, we searched the reads for every trusted novel kmer. More than 80% of reads containing these kmers were found to map to multiple homes in the genome (summarized per sample in Figure 1.4).

1.4 *Discussion*

1.4.1 *Failure of the mapping approach*

The preponderance of reads containing novel kmers fail to map uniquely to the reference genome, explaining why we should find such a massive discrepancy between the novel kmers we expect versus explain - reference-based calling approaches cannot call variants

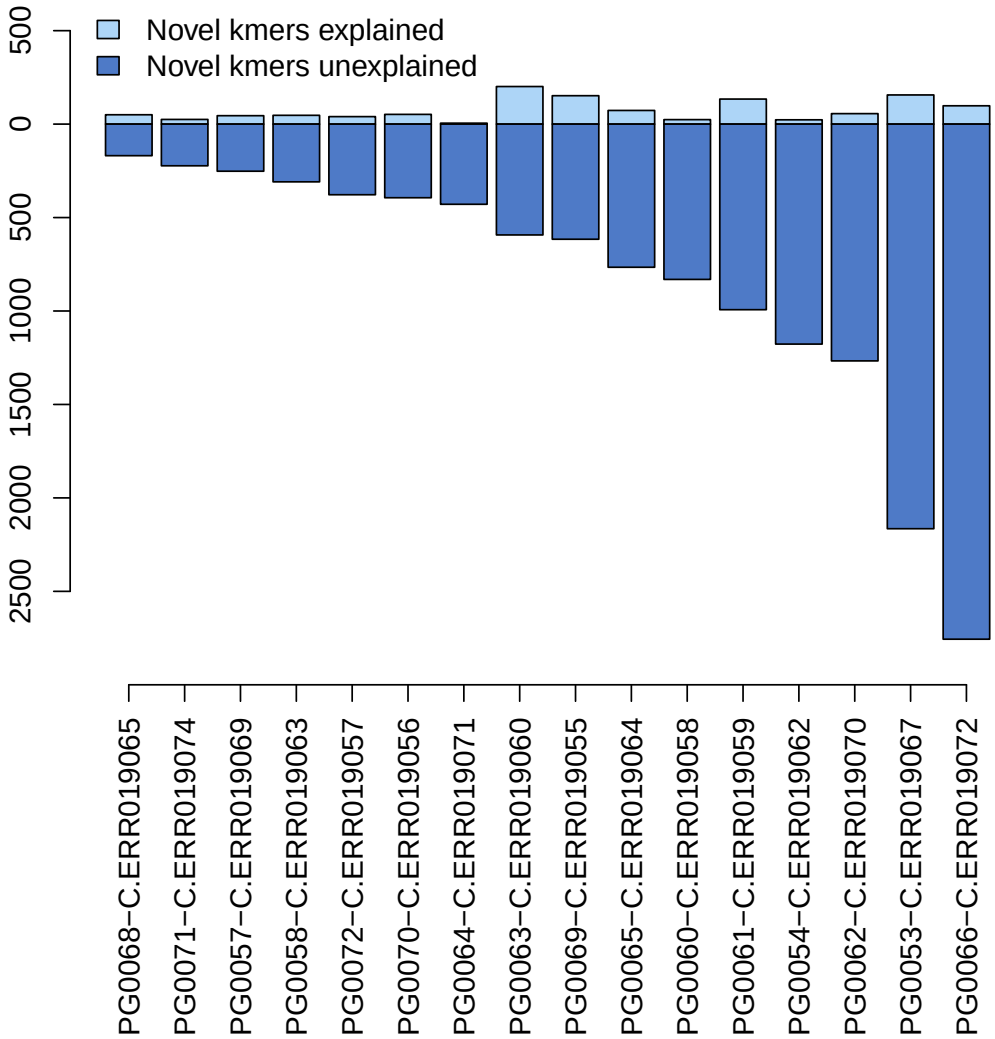

Figure 1.3: Novel kmers observed in the reference-based analysis vs trusted novel kmers expected from the reference-free analysis.

on unplaced reads. That there should be so many reads that fail to map is perhaps not surprising, given the divergent nature of the reference genome to other samples. Figure 1.5 shows the overlap between kmer sets between the 3D7 and HB3 genomes. More than 20% of the total set of kmers between these two samples is unique to each sample.

These unique kmers are not simply repetitive, intergenic, or otherwise uninteresting kmers. They often reflect interesting biology. Figure 1.6 shows one example: three *var* genes from 3D7's 60-member antigenic repertoire. These genes do not overlap with the HB3 repertoire. One of the 3D7xHB3 progeny, has inherited one of the 3D7 *var* genes in full, but curiously exhibits mosaic recovery of two others. This is known to be an NAHR

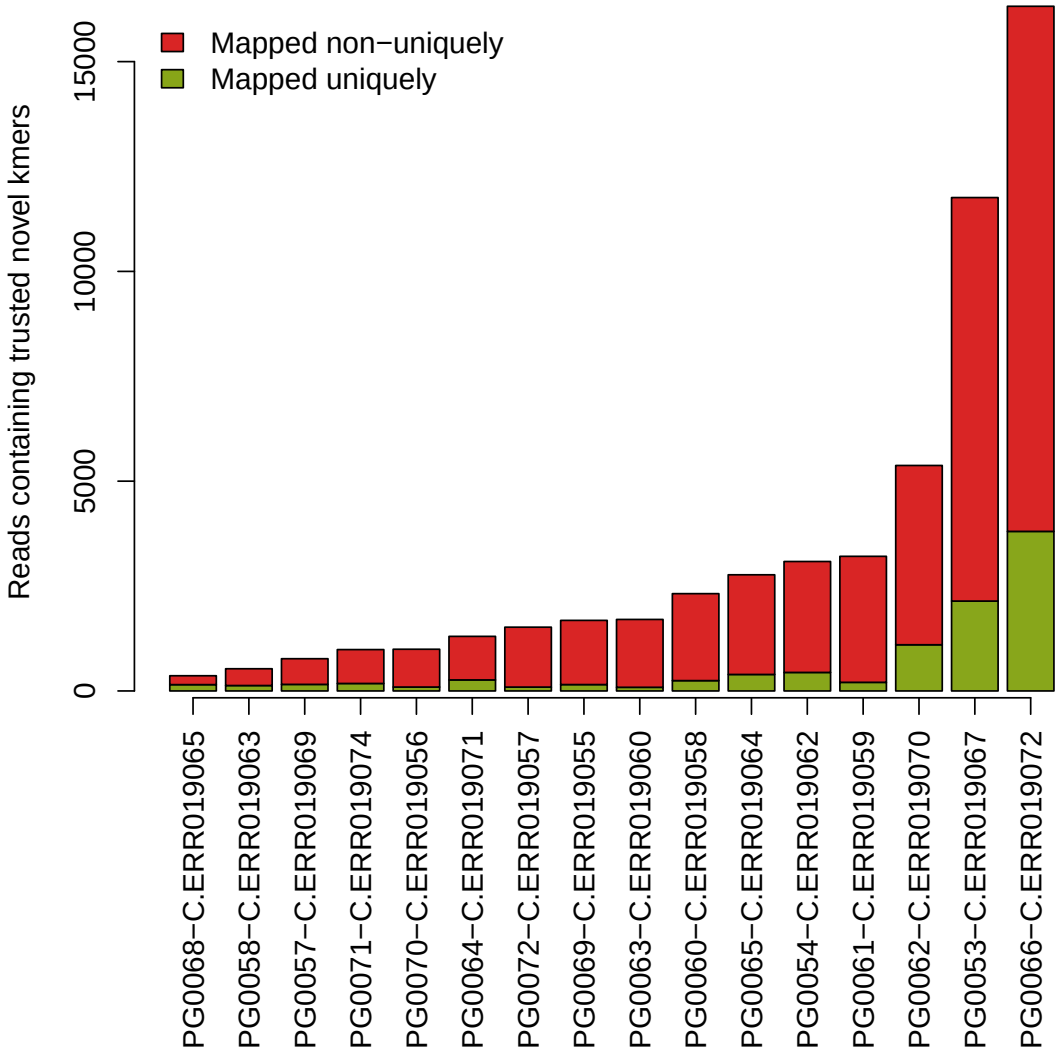

Figure 1.4: Reads that map once to the reference genome versus mapping multiple times, conditioned on the read containing a trusted novel kmer.

event between the telomeres of chromosomes 1 and 2, likely to have occured during mitosis, preserving the domain architecture and yielding a functional product.[32]

Alignment of short reads to a single reference and subsequent application of variant callers is a poor strategy for *de novo* variant discovery in *P. falciparum* (and likely higher-order species as well) for a number of reasons:

1. **Absent or divergent loci in genome**

   The underlying assumption that two genomes from the same species should be very similar is inappropriate for highly diverse populations (e.g. pathogens) or

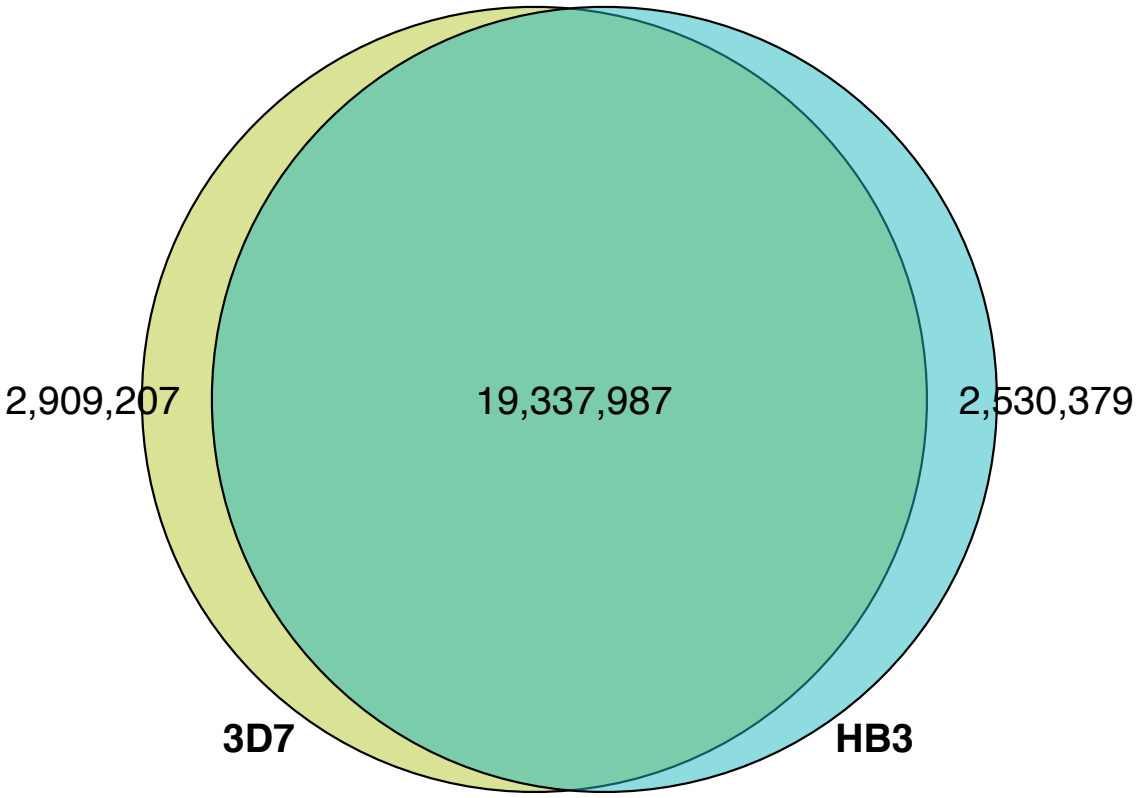

Figure 1.5: Venn diagram of kmers present in the 3D7 and HB3 genomes at $k = 47$. Both forward and reverse-compliment kmers are considered the same.

hypervariable regions (e.g. immune loci in mammals). If a haplotype present in the sample is too dissimilar to the reference, or perhaps even completely absent, read aligners may return incorrect results. Reads may align to the wrong location, the resultant mismatches mistaken for real mutations. Alternatively, they may fail to align at all, thus obscuring evidence of real variation.

2. **Incomplete or errorful reference sequences**
   Reference sequences are often incomplete and/or contain errors due to technical artifacts. Chaisson *et al.* provide an excellent review on the various errors that may arise.[34] Regions of the genome may fail to amplify during library preparation, leading to coverage dropout and subsequent gaps in the assembly. Insufficiently long reads used in the reference genome construction may lead to the misestimation of lengths of repetitive regions, causing repeats to have a collapsed representation relative to the true genome. Segmental duplications, gene families, or other loci with high sequence identity may generate ambiguous read overlaps that cannot be resolved without very long reads.

3. **Difficult to include prior information about variation in a species**
   Read aligners must make a decision as to how many apparent mismatches to permit with respect to the reference sequence. However, these software packages typically operate per-read, without information on prior population variation throughout the genome.

4. **Inability to include improved or project-specific data**
   Improvements in sequencing technology, or new platforms altogether, can yield supplementary datasets that adds missing information to a genome or repairs a misrepresented locus. There is no natural framework for incorporating these additional datasets to the alignment framework.

1.4.2 De novo assembly as an alternative approach

Consider Table 1.2 again, which demonstrates that we can expect to recover the full genome at as little as 10-fold coverage. For small genomes (*P. falciparum* is approximately 23 megabases in length), modern sequencing experiments can routinely return excess of 100-fold coverage. It is therefore clear that deeply-sequenced samples will have reads representing the entirety of the genome despite our inability to align all of them to the genome. Rather than relying on mapping to an imperfect and incomplete reference, we can attempt to assemble the genome *de novo* - from the sequenced data itself, ignoring the availability of a reference sequence.

The problem of performing *de novo* assembly essentially reduces to computing read-to-read alignments, rather than read-to-reference alignments. As each read represents recovery of some small region of the genome, the supersequence of overlapping reads (the aligned nucleotides flanked by the non-overlapping sequences from each read) represent some larger linear stretch of the genome. Brute-force computation of all possible pairwise alignments is $\mathcal{O}(N^2)$ in the number of reads, which is impractical for second-generation sequencing datasets with tens or hundreds of millions of reads. Fortunately, there are many ways to compute and represent these overlaps efficiently. We shall focus on one $\mathcal{O}(N)$ method in this work: assembly via construction of a de Bruijn graph.

Formal definitions can be found in Chapter 4. Informally, a graph is simply a data structure representing a collection of objects (termed "vertices" or "nodes") and connections ("edges" or "links"). In a de Bruijn graph, each vertex is a unique element. Applied to sequencing, a de Bruijn graph encodes linear stretches of sequence, while each edge represents an overlap with the connected vertices. Commonly, each read is decomposed into fixed-length words of an arbitrary length k, or "kmers". As each kmer is sequentially

extracted from a read and added to the graph as vertices, edges between adjacent kmers in the read are stored as well. Overlapping reads will share kmers, and since each kmer can only appear once in the graph, adding kmers and edges from the overlapping read effectively records the alignment without needing to literally compute all possibilities. Figure 1.7 depicts a simple 16 bp genome, sequenced with 7 bp reads, and the resulting de Bruijn graph constructed at a kmer size of 3.

Construction of this data structure is challenging. First, errors in second-generation sequencing data are very common, and therefore the graph produced from raw sequencing data will contain many branches that are not in the actual genome (examine Figure 1.7 again, observing the highlighted base - a sequencing error - and the resultant perturbation to the otherwise linear graph). These can be mitigated (but perhaps not completely solved) by error-cleaning algorithms that remove low coverage kmers, as presumably in high coverage data, random errors are rare and can be detected and discarded. Second, long repetitive stretches of the genome that feature the same kmers multiple times will be collapsed into a single copy, as de Bruijn graphs only store each kmer once. Finally, homology in the genome can cause two separate regions of the genome to appear proximal to one another in the graph. This may result in a vertices with multiple outgoing edges, causing unresolvable ambiguity when traversing the graph.

Nevertheless, such an approach should resolve many of the deficiences of an alignment-based approach. Absent or divergent loci should be recovered. The uncleaned graph should be complete (barring any regions of the genome that suffer from an amplification bias that prevents them from being sequenced). Prior information about variation in the species (or in this case, just the parents) are included by assembling the parents and comparing to them directly, rather than indirectly via the reference. Finally, additional information can be added at graph construction time or by adding a separate color to the graph encoding the supplementary data.

1.5 Overview of this work

In this dissertation, we present a novel multi-color graph-based approach to *de novo* mutation detection and allele identification. We show how knowledge of the pedigree enables us to identify so-called **novel kmers** - kmers present in children and absent from parents - that serve as an exceedingly strong signal as to the presence of *de novo* variation. We use these kmers to analyze subgraphs in the genome likely to represent DNMs and navigate color-specific paths and trails to determine the precise allele. We also demonstrate how the novel kmers act as "sign posts" during graph traversal, indicating that a traversal is following a fruitful path. This simultaneously constrains th runtime of

the algorithm and allows us to overcome sequencing error that could not otherwise be overcome. We demonstrate that this approaches yields vastly superior sensitivity and specificity to DNMs than conventional methods, and can easily access events that occur on the haplotypic background of the non-reference parent.

In Chapter 2, I present a review on mutational mechanisms that generate *de novo* mutations, their rates, factors that influence their generation, and known events in various species.

Chapters 3 and 4 detail the software packages I have written for this work, the former including descriptions of the realistic variant read simulations, the latter detailing the graph genotyping algorithm.

Chapters 5 and 6 present results from applying the algorithm to real data. The former chapter focuses on the aforementioned *P. falciparum* crosses. The latter addresses a *Pan troglodytes* pedigree.

Finally, Chapter 7 discusses the work in a larger context and details various improvements that can be made in future work.

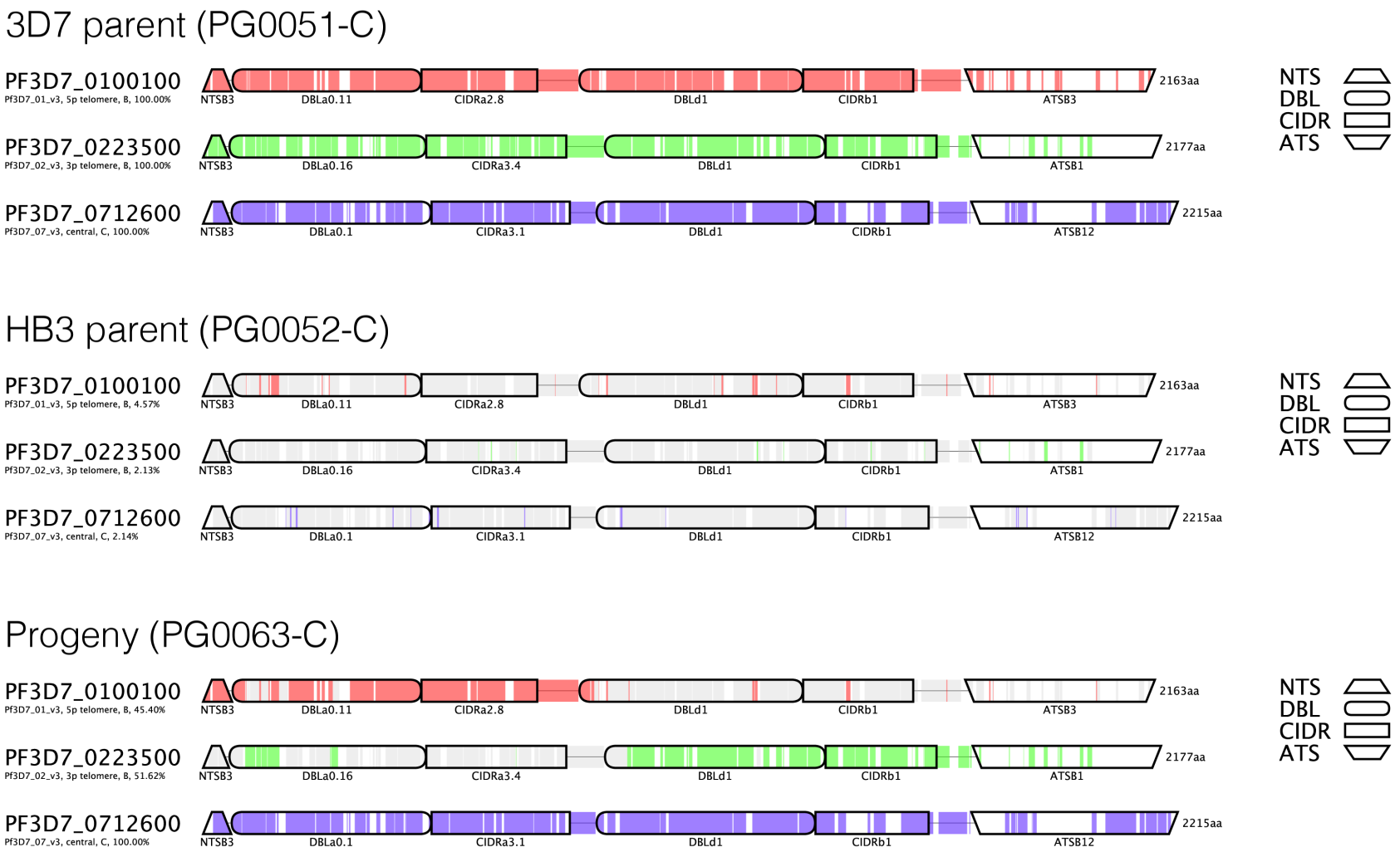

Figure 1.6: Presence and absence of unique kmers in three 3D7 *var* genes. Each vertical line represents a kmer. Colored kmers represent those unique 3D7 kmers that are recovered in the sample. Grey indicates no recovery. White indicates the kmer at that position was not unique in the 3D7 genome. Only the coding regions of the respective genes are shown, with domain annotations obtained from the VarDom server.[33]

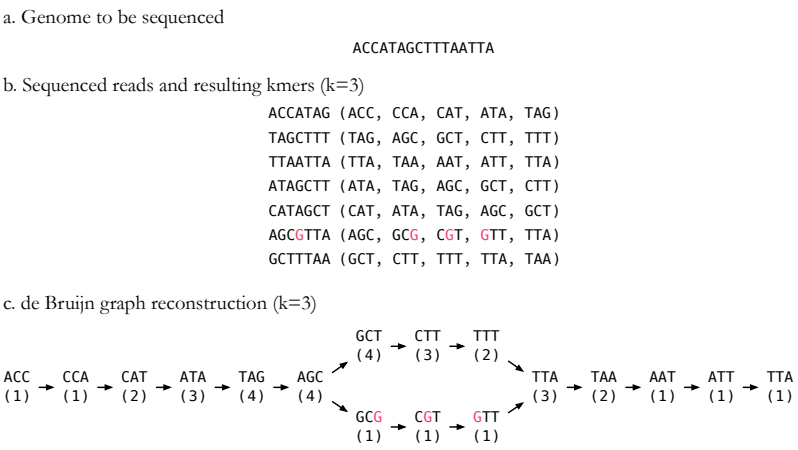

Figure 1.7: The process of generating a de Bruijn graph representation of sequence data. a. The underlying genome. b. Reads sequenced from the genome (including one read with a sequencing error). Reverse-complement reads are not shown for clarity. c. The $k = 3$ de Bruijn graph reconstruction, including kmer coverage annotations.

2 Background

2.1 How genome changes

2.1.1 Cross-over

2.1.2 Gene conversion

2.1.3 Point mutations

2.1.4 Structural variants

2.1.4.1 Small (indels)

2.1.4.2 Large (fusions, NAHR)

2.1.4.3 Chromosomal changes

2.2 Rates

2.3 Factors influencing

2.3.1 Replication time

2.3.2 Mat/pat age effects

2.3.3 Biases/locality

2.4 Known events in species

2.4.1 P.f.

2.4.2 Human

2.4.3 Chimp

2.4.4 Others

3 Simulation

De novo MUTATIONS WILL UNDOUBTEDLY TAKE MYRIAD FORMS (SNPs, insertions and deletions of varying length, expansions and contractions of short tandem repeats, tandem duplications, non-allelic homologous recombinations, and possibly even inversions). Detecting all types of variants is a considerable challenge, and the software to do so will be introduced in the next chapter. In order to measure that software's expected sensitivity and specificity to such variation, we require truth datasets to which we can compare our calls. A sufficiently small genome (on the order of tens of megabases), could be run on third-generation sequencers, the long reads used to assemble full-length genomes. Then, the variants called from short-read second-generation sequencing data could be compared to the "truth" dataset established by the newer platform. However, this is still very expensive (thousands of dollars for each sample), which limits the number of samples that could be feasibly obtained. Furthermore, if variants of the classes we are attempting to identify are absent in the handful of genomes we can afford to sequence, we would not be able to accurately ascertain our power.

We chose instead to pursue a simulation strategy in order to measure our DNM calling performance[1]. There are two components to these simulations: first we must generate the genomes of the parents and several children, including each type of DNM we hope to discover. From these genomes, we must then simulate reads that realistically model errors inherent in our data (matching read lengths, fragment size distributions, single base mismatch errors, indel errors, read pair chimeras, coverage profile, etc.). We discuss both of these components below.

3.1 Simulating genomes

Simulating a genome merely involves generating an artificial reference sequence in FASTA format. Our framework is a simple forward simulation of samples. We first generate the

[1]Several months after the simulation framework was completed, we obtained PacBio sequencing data on the parents of the 803xGB4 cross and three randomly selected progeny. These results will be discussed in a later chapter.

genomes of the parents. To generate a child's initial genome, we perform recombination *in silico*. We then add *de novo* mutations on this substrate, thus producing the child's final genome.

We make use of the Variant Call Format (VCF),[35] a text file that encodes one variant per line, specifying the genomic locus, reference and alternate alleles, and metadata for the variant, to describe differences between the two parents and the DNMs to incorporate into the child's genome. While the `FastaAlternateReferenceMaker` module in the GATK does purport to generate a new reference sequence based on variants in a VCF, we note that at the time of this writing, it silently fails to incorporate multinucleotide polymorphisms (MNPs) (simultaneous deletion and insertion). We generate many of these events to remove a reference allele and add an alternate allele in its place (e.g. inversions or gene repertoire replacements). To include this critical functionality, we developed our own tool to permute an existing reference sequence based on a single-sample VCF file.

Our algorithm, `IncorporateVariantsIntoGenome`, is described in Algorithm 2. Briefly, the sequence of each chromosome is loaded into an array, one nucleotide per array element. We then iterate over each record in the VCF file. For each SNP or insertion, we replace the reference nucleotide at that position with the entire alternate allele (for insertions, more than a single nucleotide). For deletions, we replace each corresponding array elements with empty strings. To generate the new genome, we iterate through each element of the array, emitting the string found in each position.

Note that we chose not to process each variant iteratively as insertions (deletions) would increase (decrease) the size of the array, altering the mapping between the VCF positions and the array positions. Keeping track of the mapping in spite of the changes is cumbersome. Instead, out scheme of placing all of the variants on the chromosome array first and then emitting the resulting sequence preserves the mapping. We will revisit this strategy later on in this chapter when we introduce an algorithm to lift data over from the reference genome coordinates to a simulated genome's coordinates.

Algorithm 2 could fail to produce a correct FASTA file in the pathological case that there are multiple overlapping variants called at a single locus. We are careful to avoid that scenario; we set our simulated variants to be placed no closer than 1000 bp from one another.

Many algorithms presented in this chapter rely on empirical distributions to model cross-over rates, read fragment size, indel lengths, and positional errors in reads. In all cases, we use the inverse transform sampling method for pseudo-random number generation from an arbitrary probability distribution given its cumulative distribution function

Algorithm 2 Generate an alternative reference sequence based on a VCF file.

```
1: function IncorporateVariantsIntoGenome(ref, vcf)
2:     for all chr in ref do
3:         vcs ← vcf.getVariants(chr)
4:         for all vc in vcs do
5:             if vc.getType() == DEL || vc.getType() == MNP then
6:                 for pos in vc.getPosition() : (vc.getPosition() + vc.getReferenceAllele().length()) do
7:                     chr[pos] = ""
8:             chr[vc.getPosition()] = vc.getAlternateAllele()
9:         write(chr)
```

Table 3.1: Assembly statistics on publicly available finished and draft *P. falciparum* references, ordered by scaffold N50 length. Parental samples are shown in boldface.

Isolate	Origin	Length (Mb)	Scaffolds	Scaffolds N50 (Kb)	%Q40
3D7	**Unknown**	**23.30**	**16**	**1,690.00**	**-**
HB3	**Honduras**	**24.26**	**1,189**	**96.47**	**93.17**
IGH-CR14	India	21.74	849	37.02	95.49
DD2	**Indochina/Laos**	**20.88**	**2,837**	**19.11**	**85.66**
RAJ116	India	14.11	1,199	13.00	89.68
VS/1	Vietnam	18.89	5,856	4.42	74.79
7G8	**Brazil**	**14.28**	**4,843**	**3.87**	**71.00**
Senegal_V34.04	Senegal	13.24	4,329	3.76	76.22
D10	PNG	13.38	4,471	3.71	71.80
RO-33	Ghana	13.71	4,991	3.47	69.91
K1	Thailand	13.29	4,772	3.42	73.30
FCC-2/Hainan	China	12.96	4,956	3.30	69.39
D6	Sierra Leone	13.22	5,011	3.23	71.62
SL	El Salvador	13.19	5,193	3.08	69.41
PFCLIN	Ghana	42.19	18,711	2.99	-

(CDF).[36] Simply put, we compute the CDF for an empirical probability distribution, generate a random uniform deviate between 0 and 1 for the x value, and interpolate the y value from the CDF.

3.1.1 Parents

We began by simulating the genomes of two parents using a workflow depicted in Figure 3.1. For convenience, we simulated samples from the 3D7xHB3 cross. Choosing the existing reference sequence for the 3D7 sample obviates the need to generate any data for the first parent. The second parent is tricker; while an existing draft reference sequences does exist for HB3, it is of low quality, assembled into thousands of pieces rather than

the simple 14 autosomes we expect (Table 3.1 shows metrics on every *P. falciparum* sample publicly available). Using the supercontigs from draft reference sequences is hugely cumbersome for simulating recombination as it is not straightforward to decide which chromosomes in the 3D7 genome and which supercontigs should be processed together.

Instead, we chose to produce a new HB3 reference genome sequence by taking the 3D7 reference and inserting the appropriate modifications using Algorithm 2. These modifications are comprised of two parts: introducing the appropriate variants, and replacing the *var* gene repertoire.

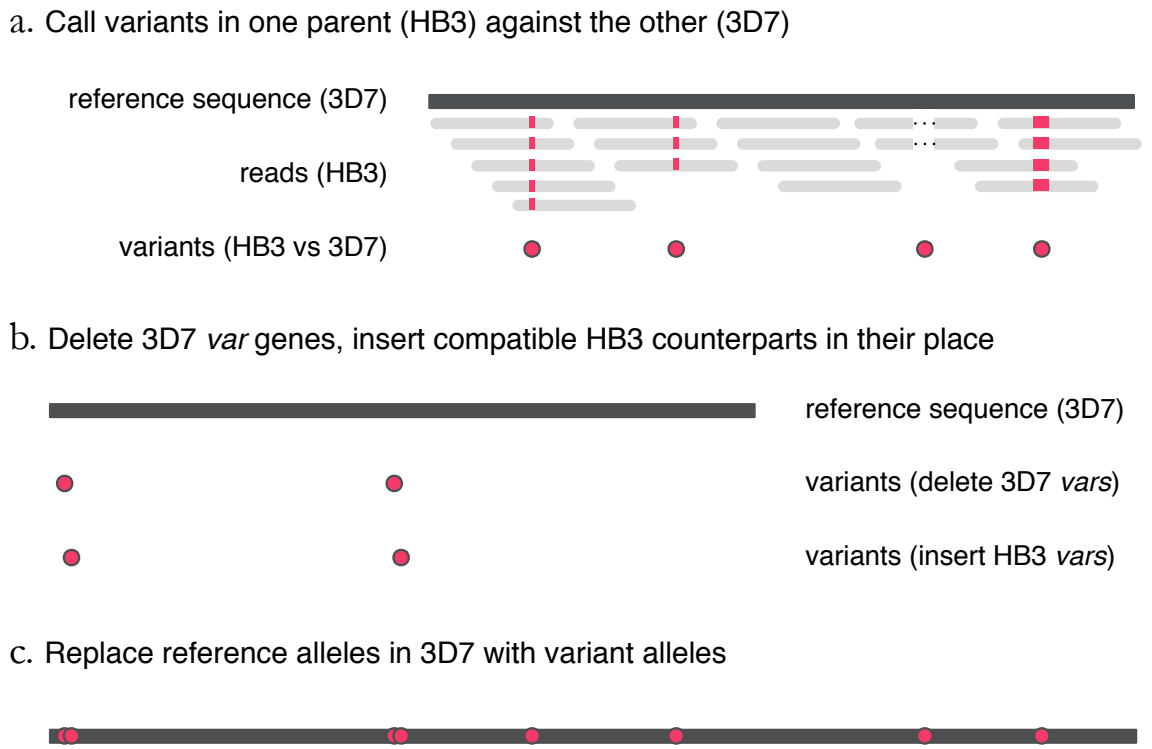

Figure 3.1: Workflow for generating the HB3 parental genome. a. Reads from HB3 sample, PG0052-C, are mapped to the 3D7 reference genome, and variants (SNPs and indels) are called and stored as a VCF file. b. We remove the 3D7 *var* gene repertoire, replacing each with a reasonable HB3 *var* counterpart, and encode the changes to the 3D7 reference genome as a VCF file. c. We alter the reference genome using Algorithm 2, thus producing the simulated HB3 genome.

We first obtained a VCF of variants found in the HB3 sample, PG0052-C, from the MalariaGen 3D7xHB3 cross dataset.[37] Variant counts are described in the Table 3.2, and include SNPs, insertions, deletions, and complex (simultaneous insertions and deletions) events. These calls were made by combining the results of the reference-based `UnifiedGenotyper` module in the GATK[24] and the reference-free bubble-calling algorithm in the Cortex[27] software. All calls were restricted to the core genome; subtelomeric regions

Table 3.2: Variants found the HB3 (PG0052-C) sample from the MalariaGen 3D7xHB3 dataset.

variants	SNPs	insertions	deletions	complex
42,054	15,376	11,807	14,643	228

were masked out due to poor mapping properties (owing to the tremendous diversity in these regions of other *P. falciparum* parasites with respect to the 3D7 reference).

Next, we produced a VCF describing *var* gene replacements. The sequences for HB3 *var* genes and upstream promoter metadata were obtained from the VarDom server.[38] No positional information from this data source is available, thus the exact placement of these *var* genes in a chromosomal context is unclear. However, previous work has established a strong association between conserved sequences of upstream promoters (phylogenetically grouped into five classes: A through E) and placement in the genome.[39] We therefore replaced 3D7 *var* genes with HB3 *var* gene counterparts, taking care to replace genes with similar UPS classes whenever possible, and grouping genes with suspiciously incomplete metadata otherwise. The replacements were described in the resulting VCF as simultaneous deletions of the 3D7 allele and insertions of the HB3 allele. No effort was made to match the orientation of the replacement *var* gene with the replaced *var* gene. The precise replacements are summarized in Table 3.3.

These two VCFs were combined to produce a complete set of changes required to transform the 3D7 genome into a pseudo HB3 genome. The transformation was applied using Algorithm 2.

3.2 *Children*

Generating the genomes of the children is slightly more involved, as there is much more biology to simulate, and many more considerations to be made when placing variants. We generated VCF descriptions of the children using a multi-stage workflow shown in Figure 3.2. In order, we simulate:

1. homologous recombination between 3D7 and HB3 genomes
2. gene conversion events
3. NAHR events between compatible *var* genes
4. *de novo* SNPs, insertions, deletions, and inversions

Table 3.3: *Var* gene replacements from 3D7 to HB3 repertoire.

3D7 gene	3D7 ups class	HB3 gene	HB3 ups class
PF3D7_0421100	UPSB5	PFHG_02500	UNKNOWN
PF3D7_0600200	UPSB2	PFHG_02495	UNKNOWN
PF3D7_0632500	UPSB5	PFHG_05132	UNKNOWN
PF3D7_0800300	UPSB2	PFHG_04012	ND
PF3D7_1200400	UPSB5	PFHG_05200	ND
PF3D7_1240900	U	PFHG_05483	ND
PF3D7_0400400	UPSA1	PFHG_03840	UPSA1
PF3D7_0425800	UPSA1	PFHG_03671	UPSA1
PF3D7_1100200	UPSA1	PFHG_04861	UPSA1
PF3D7_1150400	UPSA1	PFHG_05052	UPSA1
PF3D7_1300300	UPSA1	PFHG_03234	UPSA1
PF3D7_0533100	UPSA2	PFHG_03521	UPSA2*
PF3D7_0100300	UPSA3	PFHG_02274	UPSA3
PF3D7_0100100	UPSB1	PFHG_04081	UPSB1
PF3D7_0115700	UPSB1	PFHG_04749	UPSB1
PF3D7_0200100	UPSB1	PFHG_03516	UPSB1
PF3D7_0223500	UPSB1	PFHG_04277	UPSB1
PF3D7_0300100	UPSB1	PFHG_03717	UPSB1
PF3D7_0324900	UPSB1	PFHG_04035	UPSB1
PF3D7_0400100	UPSB1	PFHG_04491	UPSB1
PF3D7_0426000	UPSB1	PFHG_04620	UPSB1
PF3D7_0500100	UPSB1	PFHG_04593	UPSB1
PF3D7_0632800	UPSB1	PFHG_04770	UPSB1
PF3D7_0700100	UPSB1	PFHG_04057	UPSB1
PF3D7_0712300	UPSB1	PFHG_03232	UPSB1
PF3D7_0733000	UPSB1	PFHG_04928	UPSB1
PF3D7_0800100	UPSB1	PFHG_03416	UPSB1
PF3D7_0413100	UPSB3	PFHG_03476	UPSB3*
PF3D7_0712400	UPSB3	PFHG_02421	UPSB3
PF3D7_1240300	UPSB4	PFHG_02272	UPSB4
PF3D7_0809100	UPSB6	PFHG_02276	UPSB6
PF3D7_0712800	UPSB7	PFHG_04014	UPSB7
PF3D7_0808700	UPSB7	PFHG_02425	UPSB7
PF3D7_1240400	UPSB7	PFHG_04769	UPSB7
PF3D7_0412400	UPSC1	PFHG_03480	UPSC1
PF3D7_0412700	UPSC1	PFHG_03478	UPSC1
PF3D7_0412900	UPSC1	PFHG_00592	UPSC1
PF3D7_0420700	UPSC1	PFHG_02419	UPSC1
PF3D7_0420900	UPSC1	PFHG_02429	UPSC1
PF3D7_0421300	UPSC1	PFHG_02277	UPSC1
PF3D7_0617400	UPSC1	PFHG_02273	UPSC1
PF3D7_0712900	UPSC2	PFHG_04015	UPSC2
PF3D7_1200600	UPSE	PFHG_05046	UPSE

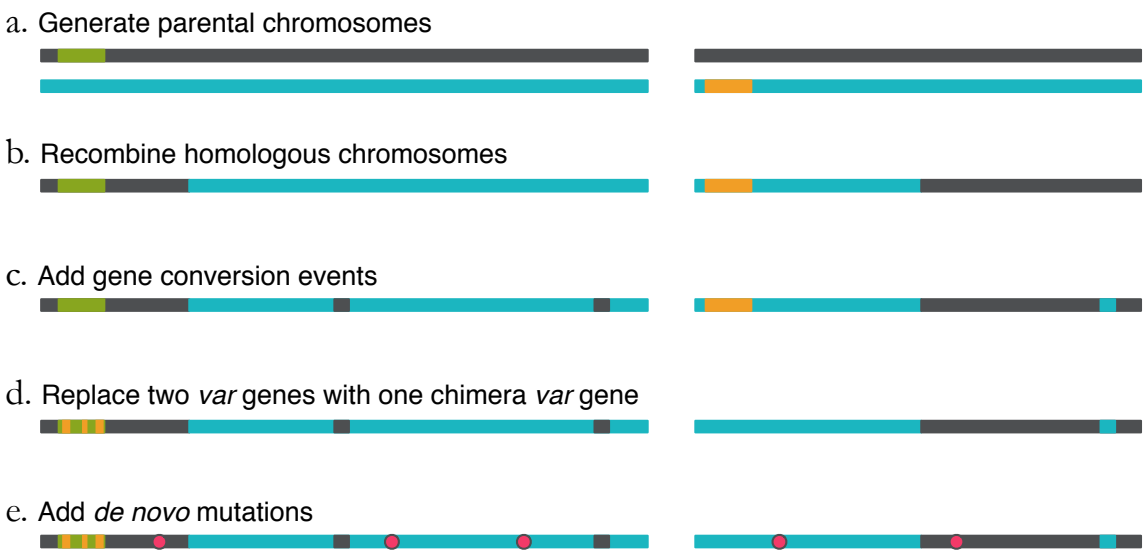

Figure 3.2: Workflow for generating children's genomes. a. Generate chromosomes from the parental genomes (compatible *var* genes shown in green and orange). b. Recombine homologous chromosomes. c. Add gene conversion events (by incorporating variants from the alternative haplotypic background over a limited genomic window). d. Replace one of the *var* genes with a chimera of compatible genes. e. Add *de novo* mutations.

3.2.1 Homologous recombination

3.2.1.1 Allelic homologous recombination

For each bivalent chromosome, the cross-over rate will be dependent on the length of the chromosome. The empirical distributions for bivalent formation and crossover were generated from the 75 samples in the MalariaGen crosses data. For each sample, only half of the chromosomes are expected to exhibit cross-over events. The cross-over rates are plotted in Figure 3.3. We simulated recombination in a sample by first drawing a binary number indicating whether a chromosome should be recombined, and if so, drawing the number of cross-over events per chromosome from these empirical distributions. The recombination sites themselves were chosen by drawing a uniform random variate between 1 and the length of the chromosome. Although there are certainly hotspots and coldspots of recombination in the genome, we have ignored this complication. An example haplotype mosaic of chromosome 12 for five samples is shown in Figure 3.4.

3.2.1.2 Gene conversion

To simulate gene conversion events, we first chose a handful of random sites known to be variant in HB3, and determined the size of the event (number of adjacent HB3 variants involved in the gene conversion) by choosing a random uniform variate between 1 and 3.

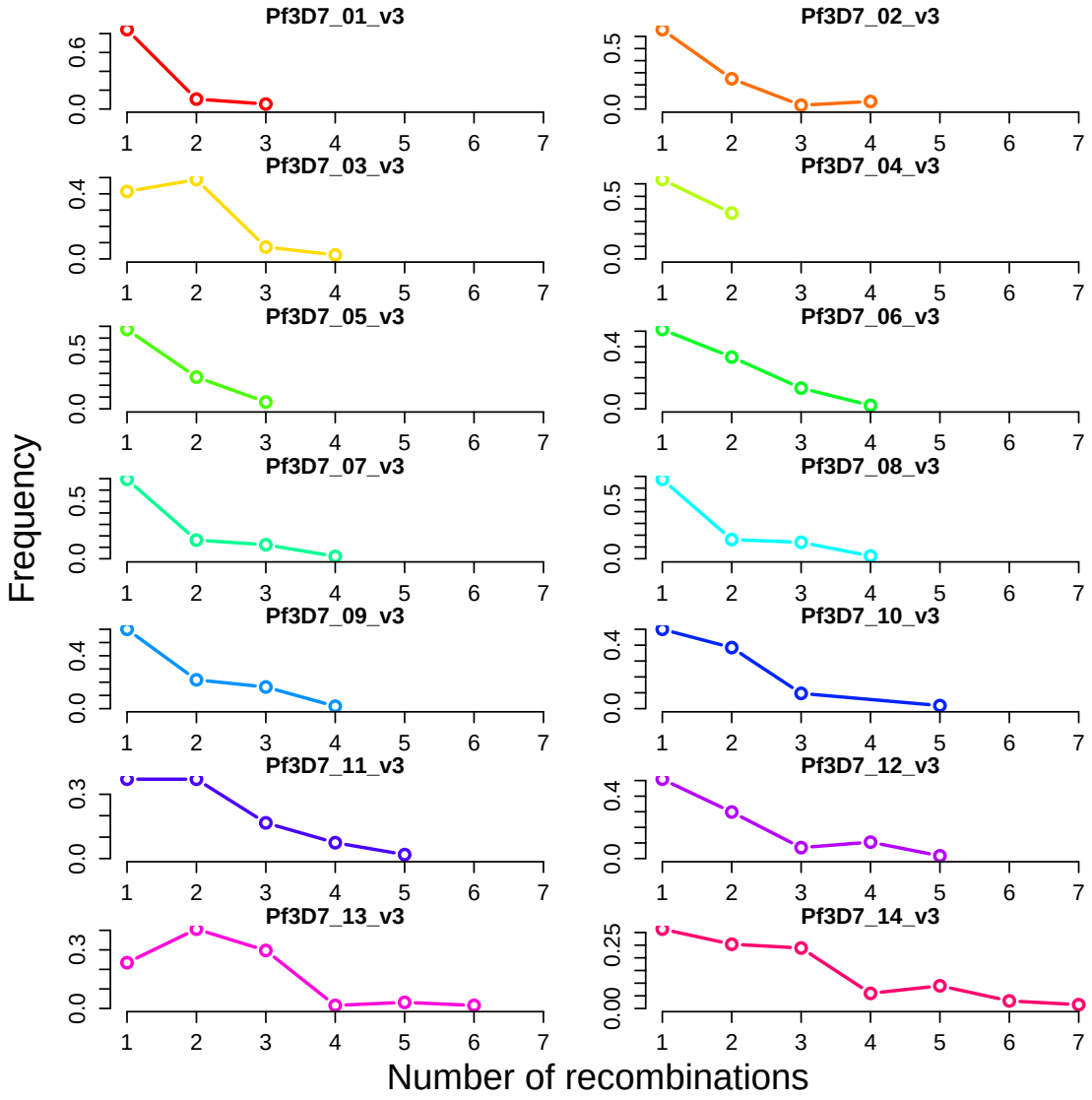

Figure 3.3: Empirical recombination frequencies per chromosome

If these sites were originally transmitted to the child, they were removed from the VCF. If they had not been transmitted, they were added. The homologous recombinations and gene conversion events are displayed below for each chromosome and sample.

3.2.1.3 Non-allelic homologous recombination

NAHR events were generated by first finding compatible recombination partners. This list was generated by determining which 3D7 *var* genes had been transmitted to the child, grouped by upstream promoter class and telomeric positioning (5′ or 3′). In each group, two random genes were chosen. If necessary, the gene sequences were reverse complemented to have matching orientation (note that the sequences may not have the same

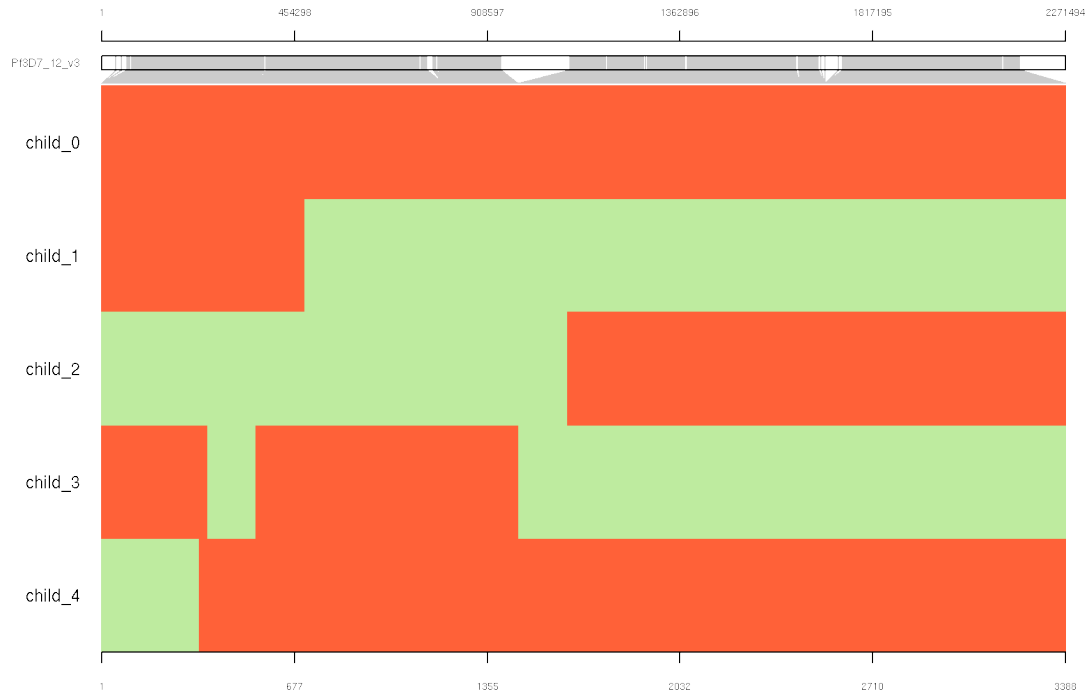

Figure 3.4: Simulated haplotype mosaics for chromosome 12. Genomic position is shown at the top of the figure, while variant number is shown at the bottom. Each variant is depicted as a vertical grey line attached to the mosaic plot at the appropriate location. In the mosaic, every variant is color-coded by parent of origin.

orientation in the simulated genomes themselves). As NAHR events between two *var* genes appear to occur in regions of homology, we identified shared 9-mers, positioned between 20 bp and 100 bp between the two genes, to act as possible recombination sites. We randomly selected between 2 and 5 of these positions to act as recombination breakpoints, switching between the sequences and copied sequence data accordingly. Keeping in mind that our previous work has shown that the recombined *var* genes are lost in order to produce the chimera, we added VCF records to delete the previous *var* alleles from the child's genome and replace one of them with the recombined sequence.

3.2.2 *SNPs, insertions, and deletions*

With the ground state genome now generated, we further generated simple events - SNPs, insertions, and deletions - on this foundation to complete the production of the child's genome. The precise number of events can be specified by the user at runtime, and for each simulated genome, different counts were specified.

To simulate *de novo* SNPs, we added sites with random (non-reference) alleles at random positions throughout the genome. We also simulated insertion, deletion, and inver-

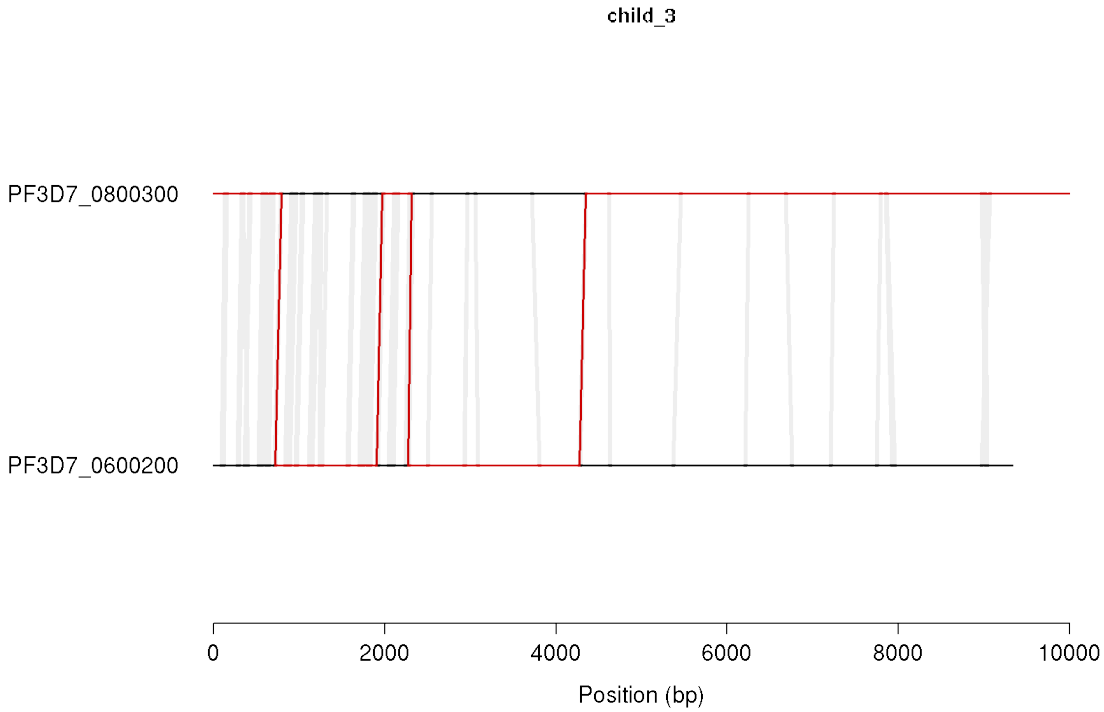

Figure 3.5: Non-allelic recombinations for two compatible *var* genes.

a. parental haplotype ATAAATATTACTCGTCGTCGTTGTGTATACTGCAGT

b. SNP ATAAATATTACTCGTC**A**TCGTTGTGTATACTGCAGT

c. insertion ATAAATATTACTCGTC**TC**ATCGTTGTGTATACTGCAGT

d. deletion ATAAATATTACTCGTCGTTGTGTATACTGCAGT

e. inversion ATAAATATTACTCGTC**CGAG**TTGTGTATACTGCAGT

f. STR expansion ATAAATATTACTCGTCGTCGT**CGT**TGTGTATACTGCAGT

g. STR contraction ATAAATATTACTCGTCGTTGTGTATACTGCAGT

h. tandem duplication ATAAATATTACTCGTCGTCGTTG**CGTCGTCGTTG**TGTATACTGCAGT

Figure 3.6: Simulated variant types. a. Original, parental haplotypic background upon which variants will be placed. b. A single nucleotide polymorphism. c. An insertion of two nucleotides. d. A deletion of three nucleotides. e. An inversion of four nucleotides. f. Expansion of a 3 bp short tandem repeat (STR) by one unit. g. A contraction of an STR by one unit. h. A tandem duplication of 11 nucleotides.

sion events at every length between 1 and 100 bp. For insertions, random alleles were generated and tested to ensure they did not match the allele already in the reference sequence. For deletions, we simply replaced the reference allele with a truncated allele of the prescribed length. For inversions, we replace the reference allele with its complement.

3.2.2.1 *Expansion and contraction of short tandem repeats (STRs)*

As a special case of indels, we sought specifically to simulate the expansion and contraction of short tandem repeats (STRs), depicted in Figure 3.6f-g. STRs are constrained to occur at loci where there are already existing repeats, and expansions (contractions) should manifest as the insertion (deletion) of whole units at a time. We first built a map of repeated 2-bp, 3-bp, 4-bp, and 5-bp sequences in the 3D7 genome. We filtered these lists, retaining only STRs where the repeated unit occurred at least three times. For each simulated event, we randomly chose a position from the appropriate list and select a number of units to add or remove. The number of units is constrained to be less than the length of the number of repeat units of the existing STR. With these considerations, we simulated expansions and contractions at the aforementioned repeat unit sizes.

3.2.2.2 *Tandem duplications*

For tandem duplications (as depicted in Figure 3.6h) of length l, we chose positions in the genome at random, copied the next l bases, and inserted an identical copy at the same locus. Events at each length between 10 bp and 50 bp were produced.

3.3 Simulating reads

We now turn our attention to simulating second-generation sequencing reads given an underlying genome. There are existing tools that will simulate perfect reads and uniform coverage, which will be important for initial tests of our variant identification software. However, the crucial simulation is of imperfect reads with non-uniform coverage. Without this, any estimate of our sensitivity and specificity is unlikely to be predictive of performance in real data.

There are many tools that can simulate imperfect reads from a given sequence. Almost every solution involves user-specified parameters controlling the properties of the sequencing data. For instance, a tool may model fragment size as a normal distribution, requiring the user to specify the requisite shape parameters. It may also permit the user to specify a desired mismatch rate to simulate the presence of sequencing error. Some tools have presets that automatically set parameters to those consistent with average behavior for various sequencing platforms.

The problem with all of these tools is an over-reliance on assumed parameters of real data. Should a fragment size distribution for real data deviate from the typical normal distribution, this will not be captured in the simulated dataset. Mismatch and indel errors do not happen at any position in the read with equal probability, but rather are biased

towards later cycles and certain sequence contexts. Read coverage is not simply Poisson-distributed, but varies across the length of the genome depending on GC bias, secondary structure, even the particular sequencing chemistry used. There are currently no tools that are capable of capturing such nuance.

Instead, we chose to learn empirical distributions of major sequencing properties using an exemplar dataset and sample from those distributions directly in order to generate reads. This frees us from having to make any assumptions about our dataset, easily generalizes to any dataset regardless of when, where, or how it was sequenced. It's also vastly more realistic than other approaches.

Our approach is detailed below. Briefly, it consists of three components:

1. A "coverage profile": a description of where every fragment and read in the genome should fall and which should contain errors.
2. A "read profile": a description of where to place errors within a read, including mismatches, insertions, and deletions.
3. The read simulator: samples from the profiles to generate reads in the new reference sequence.

3.3.1 *Constructing the coverage profile*

Construction of a coverage profile consists of two sub-problems: providing a complete description of where reads fall on the existing reference sequence, and transferring that information sensibly to the modified reference sequence. This is depicted in Figure 3.7. We address each of these needs with custom tools.

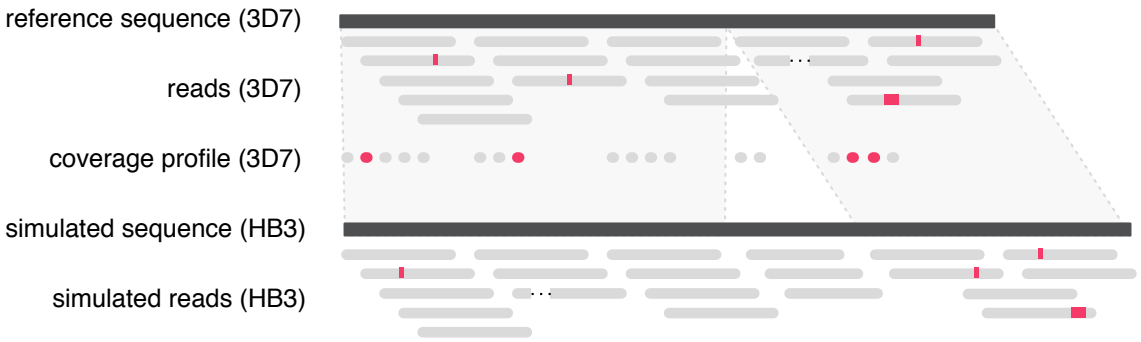

Figure 3.7: Construction of the coverage profile for the reference genome and liftover to the altered genome. Each read start (and fragment start, not shown) is stored along with a count of the number of reads at that location that contain errors. This information is then lifted over to the simulated sequence, and gaps in the table are filled in with neighboring values.

3.3.1.1 *Computing read and fragment starts, and error rates*

We developed a tool, `ComputeBaseAndFragmentErrorRates`, which provides a precise specification for the number of fragments and reads found starting at of every position in the canonical reference genome, as well as an accounting as to which reads and fragments contained any kind of error (mismatch or indels). Briefly, we iterate over every chromosome in the reference genome, advancing through every aligned read stored in an exemplar sample's coordinate-sorted BAM file. We instantiate a chromosome-length array indicating the number of reads that start at a given position and the number of reads that contain apparent errors (any discrepancy from the reference sequence).

We must also store information about read fragment starts and error rates, which requires us to keep track of read pairs as we traverse the BAM file. To do so, we hash the read name to the first instance of the read we see along the length of a chromosome. As paired-end reads have the same name, the second time we see the same read name, we will have found the second end of the pair. We then increment the count at the chromosome array position that corresponds to the 5′-most end of the pair, and increment the fragment errors array based on errors in either end of the pair.

This algorithm is described in Algorithm 3.

3.3.1.2 *Lifting read profile over from reference to simulated genome*

The genomic coordinates present in the table produced by Algorithm 3 must be transformed from the reference sequence to the simulated genome before it can be used. To do so, we developed a tool that could liftover the coordinates appropriately when given the table, reference sequence, and a VCF file describing the alterations made to the reference to transform it into the simulated genome. This is accomplished with an algorithm similar to Algorithm 2. We iterate through each chromosome as we did before, storing the entire sequence as an array of strings, placing alternate alleles in the place of reference alleles, or in the case of deletions, replacing reference alleles with blank strings. Once the array is populated, we advance through the coverage table one position at a time. At each position, we emit the contents of the previously constructed table with the number of reads, fragments, and errors for each. At some positions, insertions will have changed the length of the sequence in the bin, and the extra positions will not have explicit read and fragment information to emit. To account for this, we keep running statistics on previously seen read and fragment statistics from which we can compute running means and standard deviation. We generate new values for the number of reads, fragments, and error rates as necessary as the mean plus standard deviation of the relevant metric, ensuring the values are never less than 0, and that we round up or down to the nearest integer

Algorithm 3 Emit all fragment starts, read starts, and error rates per position.

```
1: function ComputeBaseAndFragmentErrorRates(BAM)
2:     for all chr in chrs do
3:         nReadsErrors ← []
4:         nReads ← []
5:         nFragmentsErrors ← []
6:         nFragments ← []
7:         seenReads ← []
8:         reads ← BAM.getAllReads(chr)
9:         for all read in reads do
10:            readErrorPositions ← getPositionsErrors(read)
11:            refErrorPositions ← convertReadPositionsToReferencePositions(readErrorPositions)
12:            for all refErrorPosition in refErrorPositions do
13:                nReadsErrors[refErrorPosition] + +
14:            for readPosition in 0 : read.length() do
15:                nReads[convertReadPositionsToReferencePositions(readPosition)] + +
16:            if !seenReads.contains(read.getName()) then
17:                seenReads ← read.getName()
18:            else
19:                mateErrorPositions ← getPositionsErrors(seenReads[read.getName()])
20:                if then readErrorPositions.size() + mateErrorPositions.size() ≥ 1
21:                    nFragmentsErrors[seenReads[read.getName()].getAlignmentStart() + +
22:                nFragments[seenReads[read.getName()] + +
23:        for pos in 0 : nReads.length() do
24:            print chr, pos, nReadsErrors[pos], nReads[pos], nFragmentsErrors[pos], nFragments[pos]
```

(error rates are rounded up and read/fragment counts are rounded down to increase our self-penalty).

This algorithm is described in 4.

Algorithm 4 Lift a table from reference to child coordinates.

```
1: function LiftoverFromRefToChild(ref, vcf, table)
2:     for all chr in ref do
3:         newchr = IncorporateVariantsIntoGenome(ref, vcf)
4:         for i in 0 : newchr.length() do
5:             emit(table[i])
6:             if newchr[i].length() > 1 then
7:                 for j in 1 : newchr[i].length() do
8:                     emit(extrapolate(table[i]))
```

3.3.2 *Constructing the read profile*

Next, we generate the read profile, describing the various properties of fragments and read. As in previous examples, we iterate over each read in the exemplar sample's BAM file, storing relevant information in tabular form.

3.3.2.1 *Scalar properties*

We first store the following scalar information (as the data we are modelling is assumed to be Illumina data generated from a single library, some properties which could otherwise be stored as distributions are instead treated as a single number that will be simple constants in our simulation):

1. read length
2. number of reads
3. number of reads with errors
4. number of read pairs
5. number of chimeric pairs (each end aligned to different chromosomes)
6. number of mismatches
7. number of insertions
8. number of deletions

Table 3.4: Example read and fragment scalar properties for sample PG0063-C.

	PG0051-C
readLength	76
numReads	38,846,418
numReadsWithErrors	3,696,708
numPairs	19,473,634
numChimericPairs	348,294
numMismatches	6,525,504
numInsertions	139,941
numDeletions	317,076

Example values for each of these metrics can be found in Table 3.4. Note that some of the mismatches, insertions, and deletions may represent true variation between the sample and the reference sequence. We do not mask these sites out. While this increases the apparent error rate, the variant rates are typically low compared to the number of bases in the reference sequence itself, making the difference negligible. Furthermore, we will choose the reference sample as the exemplar dataset for the read simulations. Since this sample should theoretically be identical to the reference sequence, this choice obviates the need for any masking of variants in the reference sample against the reference sequence.

3.3.2.2 Empirical distributions

Other properties take on a range of values with some probability. Rather than trying to fit the underlying distributions explicitly (which can often fail as datasets contain more nuance than what sequencing platforms should theoretically produce), we instead store empirical distributions and generate random values from them accordingly. We store the following empirical distributions:

1. number of errors (of any type - mismatch, insertion, or deletion) in a read
2. fragment size
3. insertion size
4. deletion size

Note that these distributions are not conditioned on position in the read. Example distributions derived from an exemplar sample are shown in Figure 3.8.

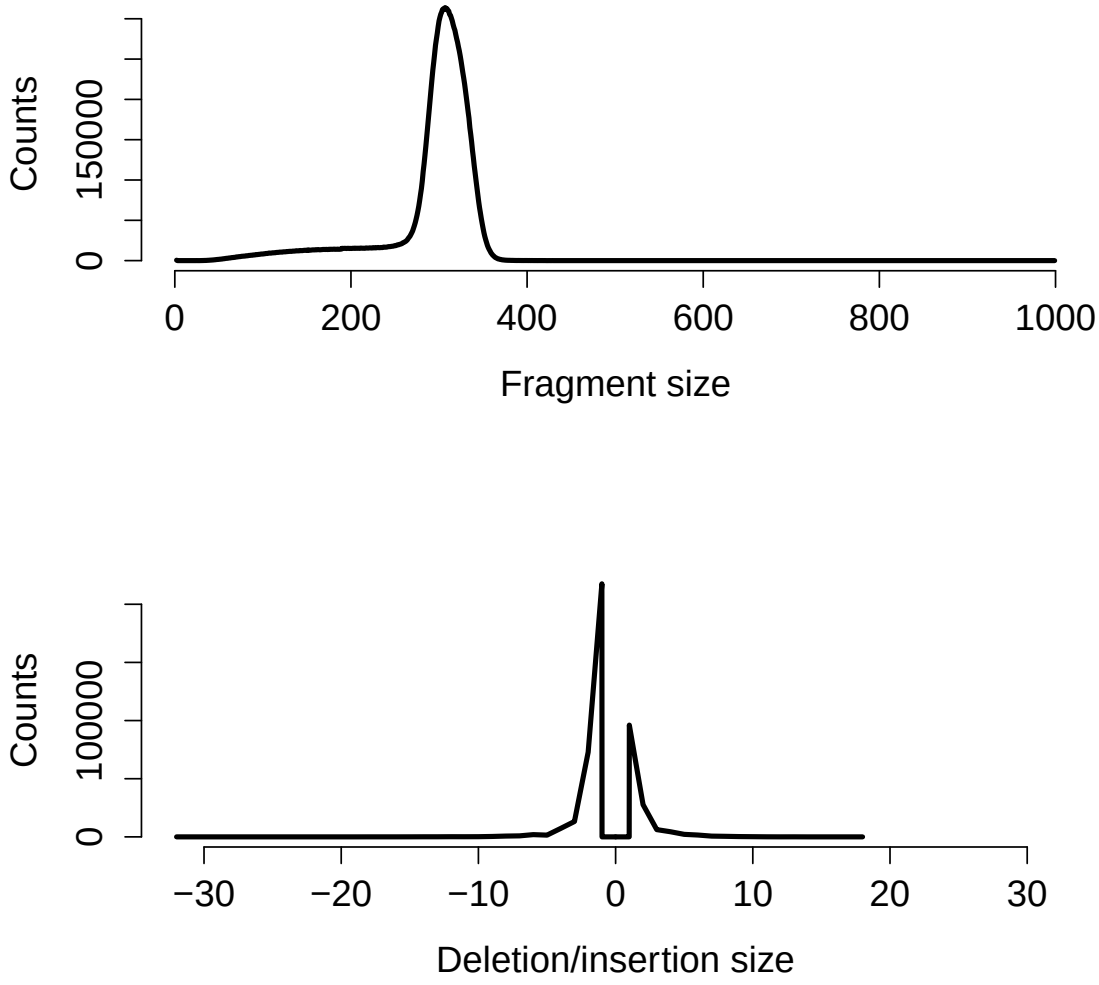

Figure 3.8: Top: empirical fragment size distribution for PG0051-C. Bottom: empirical deletion (negative values) and insertion (positive values) length distribution for the same sample.

3.3.2.3 Covariate table

Finally, we construct the covariate table: a set of empirical distributions for various error events conditioned on the following:

1. type (SNP, insertion, deletion)
2. end of pair (first end or second end)
3. strand (positive or negative)

4. 5′ dinucleotide context

5. position in read

6. first base of error sequence (empty for deletions)

For each read, we increment an element in a table that corresponds to these six covariates. The code to do so is contained in our `GenerateReadSimProfile` module.

3.3.3 *The read simulator*

With the coverage and read profiles in hand, we are finally ready to simulate reads. We advance through each base of the simulated genome, reading the coverage profile as we traverse. At each site, we use the coverage profile to dictate the number of fragments that must be generated and how many of those fragments should contain errors, thus modelling regions of the genome with higher or lower error rates. We then generate fragments, sampling fragment lengths from the empirical fragment length distribution. If a read is to contain an error, as specified by the coverage profile, we construct a read-specific error profile for mismatches, insertions, and deletions. These profiles take into account the preceeding dinucleotide context for each position in the read[2], the end of the pair being simulated, whether the fragment came from the positive or negative strand, and the first nucleotide of the error to be incorporated (not applicable for deletions).

3.4 *The simulated dataset*

With our genome and read simulation framework now complete, we simulated the genomes of 20 progeny from a pseudo 3D7xHB3 cross. The precise counts of variant types per sample are shown in Table 3.5. For each sample, we generated two datasets: a so-called "perfect" dataset (uniform coverage, perfect reads), and a so-called "realistic" dataset (non-uniform coverage, imperfect reads). Both datasets contain approximately $150x$ coverage.

[2]To handle the first and second positions in the read, which do not have a dinucleotide context, we simply extract a read by starting two nucleotides into the simulated fragment.

Table 3.5: *De novo* variant counts for each of the 20 simulated children.

	DEL	GC	INS	INV	NAHR	RECOMB	SNP	STR_CON	STR_EXP	TD
0	22	25	22	22	2	10	5	3	3	26
1	21	21	21	21	2	10	23	11	11	26
2	11	22	11	11	2	8	13	22	22	8
3	25	17	25	25	2	32	23	17	17	21
4	4	23	4	4	2	8	14	16	16	12
5	26	23	26	26	2	37	28	5	5	8
6	13	17	13	13	2	15	27	23	23	4
7	1	22	1	1	2	30	28	5	5	12
8	26	16	26	26	2	16	16	13	13	8
9	4	23	4	4	2	25	23	23	23	21
10	12	20	12	12	2	16	23	19	19	27
11	13	19	13	13	2	7	20	18	18	17
12	19	20	19	19	2	8	14	5	5	28
13	10	20	10	10	2	25	13	28	28	11
14	28	18	28	28	2	8	3	29	29	17
15	27	22	27	27	2	30	5	19	19	2
16	23	22	23	23	2	12	29	24	24	17
17	17	22	17	17	1	10	28	13	13	11
18	23	18	23	23	2	8	1	21	21	18
19	22	22	22	22	2	17	19	3	3	2

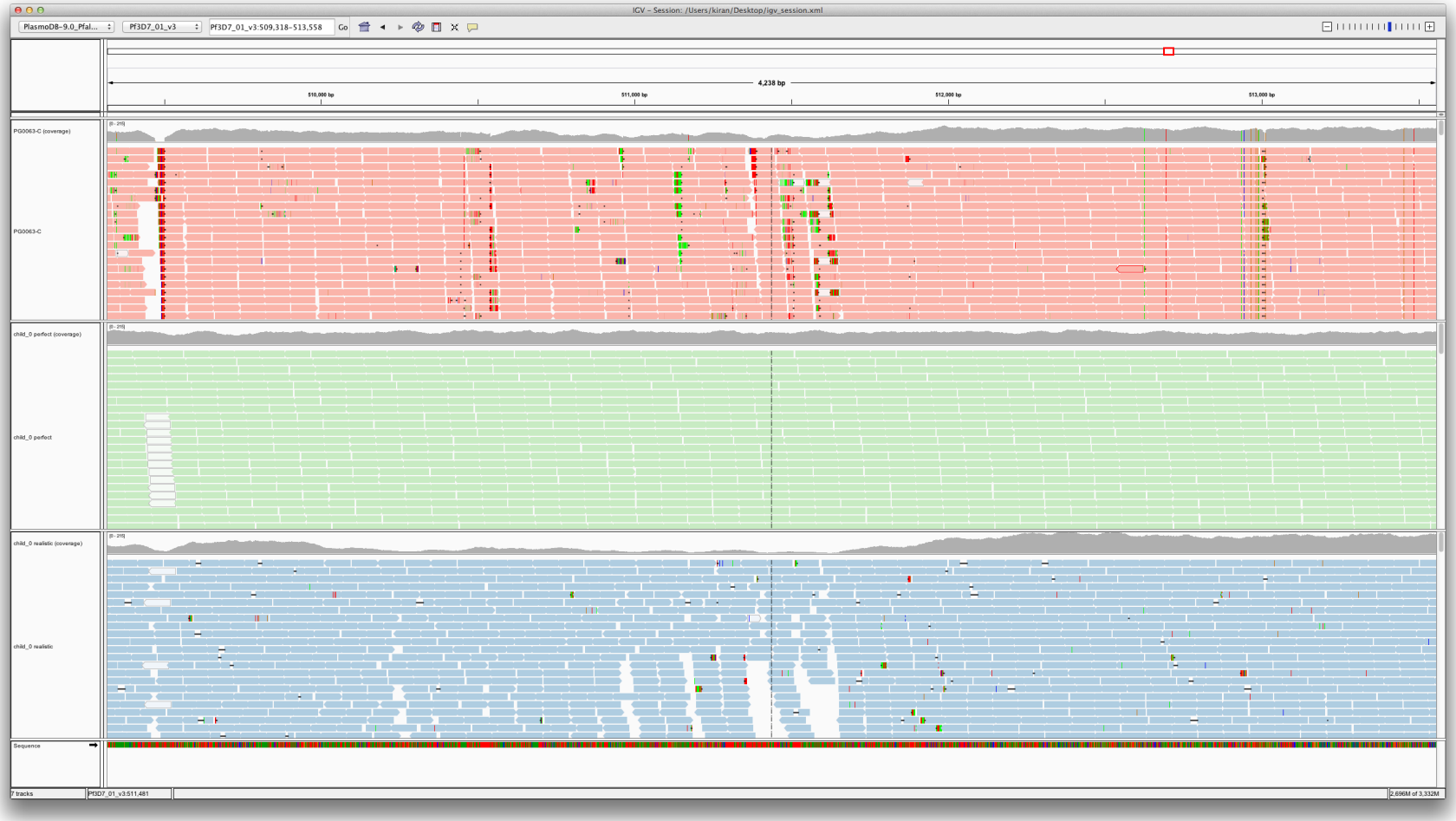

Figure 3.9: Read datasets for real (top panel), simulated perfect (middle panel), and simulated realistic (bottom panel) data.

4 *Detection and classification*

We now present a novel graphical method for detecting and classifiying *de novo* variants. We shall present some brief foundational background on *de novo* assembly, upon which the variant caller is built. The simulation framework and dataset we described in Chapter 3 will be used to establish the method's accuracy.

Reference-based analyses benefit from being reasonably intuitive, as the underlying genome is linear and there are many visualization tools that can facilitate the user's understanding of the underlying data.[40–44] In contrast, graph data structures are less intuitive and lack dedicated tools for visualization. In this chapter, we will also present images from our purpose-built trio graph visualization software for the purposes of guiding the reader's intuition regarding graphical variant motifs and the operation of the calling algorithms.

4.1 *De novo assembly*

De novo assembly refers to the process wherein a sampled genome is reconstructed from sequencing data without guidance from an existing genome. Sequenced deeply enough, a set of reads from a single sample will contain overlaps that can be used to infer the sequence of contiguous segments of the genome into so-called **contigs**. If the reads are long enough to span repetitive regions in the genome, these contigs could be as long as the chromosome itself. Otherwise, separate contigs can be joined together into **scaffolds** (contigs plus gaps) using paired-end reads, information from linkage analysis, HAPPY mapping, and other methods.

The quality of the reconstruction can vary considerably depending on how the assembly is performed. Typically, constructing a complete and high-quality reference sequence (one with few errors and few gaps in the linear sequence of each assembled chromosome) is a big first step to studying the genome of an organism, done at great expense and labor over a period of several years. In 2002, after several years of work, Gardner *et al.* published the sequence of the 3D7 *P. falciparum* parasite clone. By using a whole chromosome

Table 4.1: Comparison of assembly statistics of the finished 3D7 reference genome and a reconstruction of the same sample from 76-bp Illumina data.

	contigs	min length	max length	mean length	N50	total sequence
3D7	16	5967	3291936	1458302	1687656	23332831
PG0051-C	51425	47	27520	478	1280	24602599

shotgun strategy with accurate and long (several hundred bp) first-generation sequencing reads (Sanger), each chromosome was fully resolved with very few gaps in the sequence and no unplaced contigs.[28]

Today, the same sample can be assembled in a matter of days rather than years using high-throughput second-generation sequencing. Short reads ($76 - 100$ bp) from second-generation sequencers (Illumina) can be produced cheaply and in abundant quantities, and similar read overlap considerations can be used to generate assemblies. However, these reads tend to be much more error prone, and the shorter read length fails to span many repetitive regions of the genome. The result is a much cheaper, but far more fragmented assembly than the reference assembly. Table 4.1 compares the assembly statistics of the reference genome versus a reconstruction of the same sample from Illumina data taken from our cross dataset (PG0051-C) using the McCortex assembly software.[45] While the parasite genome is known to have 16 chromosomes (which the reference recapitulates), the Illumina assembly broken into over $50,000$ pieces with an N50[1] of a mere $1,280$ bp.

It is perhaps surprising then to discover the central argument of this dissertation is on the value of *de novo* assembly of short reads for *de novo* mutation discovery. After all, a poor-quality Illumina assembly - as evidenced by the numerous short contigs - would seem to be very limiting, even if it could theoretically reconstruct pieces of the genome that cannot be recovered from a reference-based analysis. However, for the work that we describe in this chapter, the value is not in the contig reconstructions, but in the underlying data structure from which the contigs are produced: the "de Bruijn graph".

The de Bruijn graph is a data structure that encodes read overlaps such that a walk through the vertices with unambiguous connections yields contiguous sequence in the genome. In real data, those walks may end prematurely due to errors or homology, yielding junctions that cannot be confidently navigated. Typically, assembly algorithms will be conservative in the contigs they emit from this data, choosing to terminate the walk at the junction rather than risk going forward and emitting sequence that does not actually

[1] **N50**: the length for which the set of all contigs that length or greater represents half the total lengths of all contigs.

appear in the genome. However, with an additional set of metadata and a reasonable assumption, we can traverse the barrier. In trio data, it is easy to detect a so-called novel kmer: a kmer occuring in the child but absent in the parents. By annotating the graph with this information, we can see stretches of novel kmers. Figure 4.1 shows a portion of such an annotated graph. Ignoring the annotations, a traversal that starts at vertex D would yield a short contig: $C \rightarrow D \rightarrow E$. However, if we assume the novel kmers link together, we can extend our traversal to yield $C \rightarrow D \rightarrow E \rightarrow F \rightarrow G \rightarrow H$. These novel kmers are the hallmark of *de novo* variation, and by utilizing these annotations, we can navigate parts of the graph that are otherwise unnavigable, surpassing what conservative contigs can give us and providing tremendous sensitivity and specificity to DNMs.

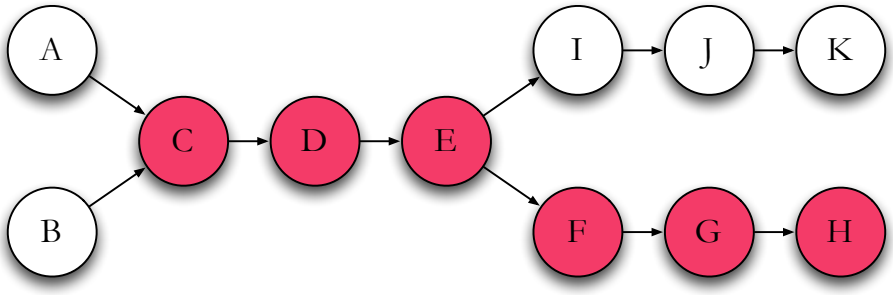

Figure 4.1: Graph with novel kmer annotations in red.

4.1.1 Definitions

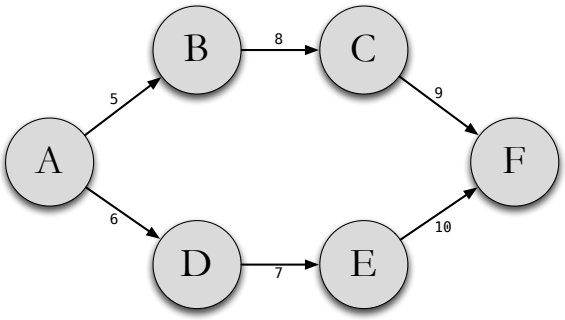

Figure 4.2: An example directed graph with six vertices.

First, we provide some definitions. We denote a **graph** as $G = \{\mathcal{V}, \mathcal{E}\}$ where $\mathcal{V}$ represents a unique set of **vertices**, and $\mathcal{E}$ a set of **edges**.[46] We shall assume the set of vertices $\mathcal{V} = V_1, V_2, ..., V_n$. A pair of vertices may be connected by an edge. For the purposes of this dissertation, we shall require that all edges are **directed** (though for some applications outside this work, it is also possible for edges to be **undirected**). Written as $V_i \rightarrow V_j$

(or equivalently $V_i \leftarrow V_j$ and $V_j \rightarrow V_i$), directed edges restrict graph traversal in one direction (thus enforcing a traversal order when reconstructing a region of the genome). A vertex may have a number of incoming (outgoing) edges, the precise count being referred to as a vertex's **in- (out-) degree**. We shall also refer to any vertex with an in-degree or out-degree greater than 1 as a **junction**.

A **path** is a sequence of adjacent vertices that respects these edge relationships, i.e. $V_i, ..., V_k$ such that for every $j = i, ..., k$, we have $V_j \rightarrow V_{j+1}$. In Figure 4.2, the vertex sequence A, B, C, F forms a path. Similarly, a **trail** denotes a sequence of adjacent vertices, but does not respect the directionality of the edges. In Figure 4.2, the sequence F, E, D, A forms a trail. Edges can optionally carry **weight**, indicating an arbitrary cost for traversing from one vertex to another via particular edges. Unless otherwise specified, we shall assume the edge weight is always 1.

A **multi-color graph** is a useful extension for multi-sample scenarios. Each edge carries additional metadata used to denote sample identity (e.g. each sample is assigned a unique "color"). All kmers in all samples are added to the graph, and following the edges with the same color yields the genome of that sample. Many kmers will not be accessible when traversing paths or trails in one color versus another. These motifs are the hallmark of most variation in a graphical setting.

Often in this dissertation, we will perform operations on a limited graph region wherein we process only vertices of interest and all edges present between them in the original graph. This is referred to as an **induced subgraph** (which is *not* technically synonymous with a subgraph, but for simplicity in this work, we will often drop the "induced" qualifier). Let $\mathbf{V} \subset \mathcal{V}$. The **subgraph** $G[\mathbf{V}] = \{\mathbf{V}, \mathcal{E}'\}$ where $\mathcal{E}'$ are all the edges $V_i \rightleftharpoons V_j \in \mathcal{E}$ such that $V_i, V_j \in \mathbf{V}$.

A **de Bruijn** graph represents fixed length symbols (vertices) and their overlaps (edges), with the added restriction that each symbol may only appear once in the graph.[47] Applied to assembly, each symbol is taken to be a genomic sequence of length k (or **kmer**), with edges connecting vertices overlapping by $k - 1$ bases[2].

To construct the initial graph, each sequenced read is broken up into $l - k + 1$ kmers (where l is the read length) and added to the graph as vertices, with edges being placed between adjacent kmers. Overlapping reads should share kmers, and the adjacency information stored in the graph can be updated accordingly. Thus processing one read at a time in this manner will yield a graph of overlaps for the entire dataset.

[2]According to the original mathematical definition, a de Bruijn graph should represent *every* possible symbol of length k, which makes the assembly formulation a subgraph rather than a graph. However, none of the relevant literature refers to assembly graphs in this manner, so we shall carry on abusing the term.

We rely on the Cortex assembly software for construction of the graph. Cortex represents the graph on disk as fixed-width records (herein referred to as **CortexRecords**) consisting of a **CortexKmer** (defined as a odd-length kmer or its reverse complement, whichever is alphanumerically lower), coverage in each color, and a list of incoming and outgoing edges. The edge lists utilize a minimalist description. For incoming edges, only the first base of the preceeding kmer is stored; the rest of the kmer is assumed to be the 0 to $k-1$ substring of the current kmer. Likewise, for outgoing edges, the subsequent kmer is assumed to be the 1 to k substring of the current kmer plus the last base of the next kmer. Figure 4.3 lists three example records. In the first record, the specified kmer has coverage 9 in color 0 (for our purposes, the child), 8 in color 1 (mother), and 5 in color 2 (father). The trailing three columns encode edge information per color. The first four characters of each column denote incoming edges to kmers with A, C, G, or T prefixes (or "." for no edge to that prefix). The last four characters of each column denote outing edges to kmers with A, C, G, or T suffixes (or "." for no edge to that suffix).

```
AAAAAAAAAAAAAAAAAAAAAAAAAAAAAAATATATGTATATATATA 9 8 5 a......T a......T a......T
AAAAAAAAAAAAAAAAAAAAAAAAAAAAAAATATATGTATATTAACT 7 6 3 a...A... a...A... a....C..
AAAAAAAAAAAAAAAAAAAAAAAAAAAAAAATATATGTATGTATATA 4 9 0 a......T a......T ........
```

Figure 4.3: Example CortexRecord entries.

The Cortex de Bruijn graph can be easily represented as a hash table where each key is a CortexKmer and the associated value a list of incoming and outgoing edges. This enables lookups to be performed in $\mathcal{O}(1)$ time, but requires the entire graph be loaded into memory. While this makes sense from the perspective of a software developer writing assembly software (where one would assume that every kmer will be processed during the lifetime of the program's execution), it is cumbersome for our purposes. DNMs are anticipated to be scant, which implies that the number of kmers that need to be examined is modest. Furthermore, should we wish to scale to larger genomes in the future (e.g. the 3 gigabase chimpanzee genome), we must be aware of the much greater difficulty in loading such a graph entirely into memory (unless one happens to be operating on a computer with several hundred gigabytes of available RAM). Instead, we sort the Cortex graphs and perform a binary search whenever we need to load the CortexRecord associated with a particular CortexKmer. This increases the time complexity for kmer lookups to $\mathcal{O}(\log n)$, but eliminates the need to load the entire graph to memory.

We define a series of utility functions that aid graph traversal. The **`findRecord`** method retrieves the CortexRecord indexed by a kmer via a binary search over the sorted disk-based graph, or throws an error if the graph is not sorted. The CortexKmer within the

CortexRecord, in addition to carrying the text of the kmer, also stores a bit that indicates whether the stored orientation matches the requested orientation, which is useful for navigation. The methods **`getPrevKmers`** and **`getNextKmers`** retrieve lists of kmers connected to incoming and outgoing edges of the specified kmer, orientation-matched to the kmer `sk`.

Many methods will accept two graphs rather than just one: a **clean** graph and a **dirty** graph. The clean graph represents data where errors have been removed by the assembly software's automatic filtering process (coverage and contig length considerations). The dirty graph represents data prior to this cleaning step. When a kmer is absent from the clean graph or lacks incoming/outgoing edges, traversal can still continue if the dirty graph contains the requested kmer and edge information. This overcomes an issue wherein *overcleaned* data (data filtered with too stringent a threshold) causes erroneous gaps in the graph. If carefully used, the dirty graph can be used to patch these holes without causing significant errors in the traversal. Almost all methods with this double graph signature have a form that look like Algorithm 5, wherein a single graph version of the same method is called, only to be called again if the operation on the clean graph was unsuccessful.

Algorithm 5 Get next kmers from the clean graph, failing back to the dirty graph

```
1: function getNextKmers(clean, dirty, kmer, color)
2:     nextKmers = getNextKmers(clean, kmer, color)
3:     if (dirty != null && nextKmers.isEmpty()) then
4:         nextKmers = getNextKmers(dirty, kmer, color)
5:     return nextKmers
```

Finally, we present in Figure 4.4 the UML diagram of the relevant parts of codebase encapsulating the relationships between `CortexGraph` (manager of access to underlying disk representation of the multi-color de Bruijn graph); `CortexRecord` (decodes graph records into kmer, coverage, and incoming/outgoing edges); `CortexKmer` (the kmer itself, along with orientation information); the utility method object `CortexUtils` (a collection of miscellaneous methods written to facilitate graph navigation); and the `AnnotatedVertex` and `AnnotatedEdge` objects (used to store subgraphs and metadata).

For clarity of the pseudocode presented below, we will refrain from referring to the object to which a method is bound. For example, rather than specifying `CortexUtils.getNextKmer(...)` in an algorithm, we shall simply write `getNextKmer(...)`. We *will* refer to the parent object if doing so implies different data being accessed. For example, `clean.findRecord(...)` and `dirty.findRecord(...)` refer to different data sources, the former being the error-cleaned data, the latter data that has not be processed in this manner.

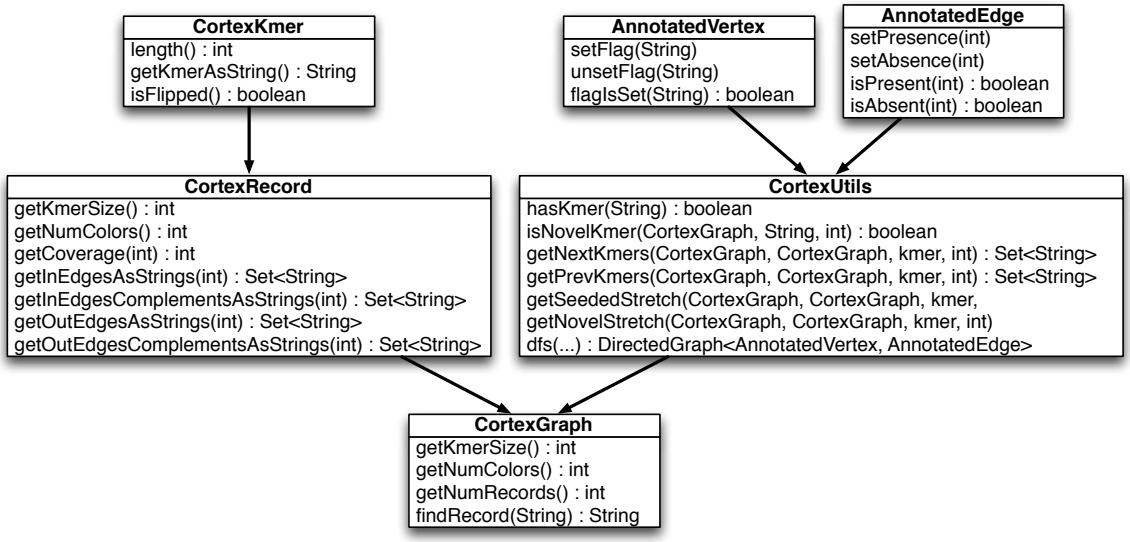

Figure 4.4: Relationships between the `CortexGraph`, `CortexRecord`, `CortexKmer`, `CortexUtils`, `AnnotatedVertex`, and `AnnotatedEdge` objects.

4.2 Variant motifs

Just as reference-based methods search for motifs in the data representing variants (e.g. recurrent mismatches, gaps, or unusual truncations in the read alignments; read pairs aligning much further apart than expected; chimeras or inter-chromosomal alignments; etc.), so must we scan for indicative motifs in the assembly graph. Before we discuss the precise nature of these motifs, it is useful to draw a distinction between "simple" and "complex" variants. A "simple" variant is a SNP, insertion, or deletion that occurs within a single chromosome. A "complex" variant could be a homologous or non-homologous recombination, translocation, or other interchromosomal exchange - something that does not fit within the confines of the straightforward SNP or indel classification. The patterns inherent to these two categories of variants are very different.

4.2.1 Simple variant motifs

Simple variants in *de novo* assembly data typically manifest as "bubbles" in the de Bruijn graph: regions where a variant has broken the homology between sequences, resulting in flanking kmers that are shared between the samples and spanning kmers that differ through the variant itself. In a single diploid sample, this could be a heterozygous SNP or indel between two homologous chromosomes. In a collection of haploid samples, one or more samples may differ from the others, resulting in the bubble.

As an illustration, consider three sequences from a mother-father-child pedigree, shown

in Figure 4.5a. While the maternal and paternal haplotypes (green and blue, respectively) are identical, the child's haplotype (red) differs by a single C to G SNP. Figure 4.5b shows the resulting multi-color de Bruijn $k = 3$ graph built from this data. The mutation has given rise to the canonical bubble motif in the graph. Three novel kmers (kmers present in the child and absent in the parents) spanning the variant allele are present. Figure 4.6 is an equivalent graph for another simulated SNP, shown with more context and constructed with a much larger value of k appropriate for 76 - 100 bp read lengths, typical of second-generation sequencing datasets (in this case, $k = 47$).

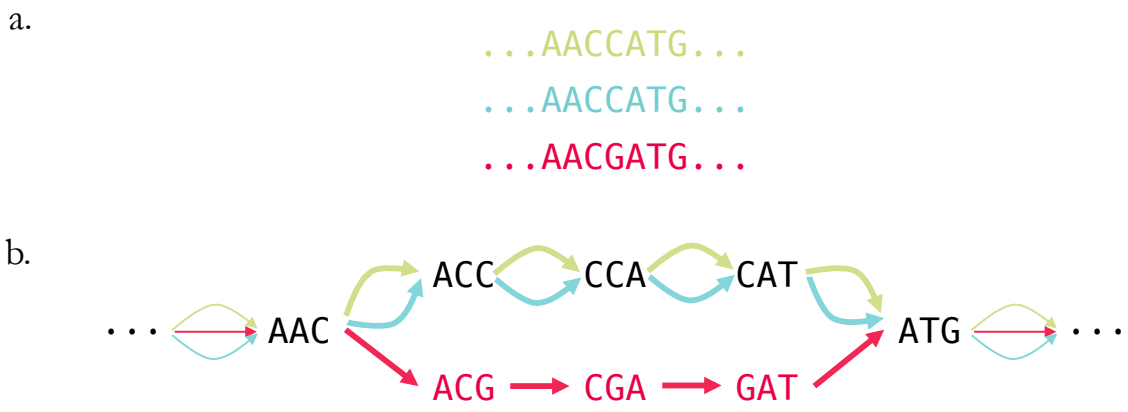

Figure 4.5: A simple variant motif for a C to G SNP. a. Haploid sequences from a mother (green), father (blue), and child (red), the last differing from the first two by a single base substitution. b. The resulting multi-color de Bruijn graph for $k = 3$. Red vertices denote kmers that are deemed "novel", i.e. present in the child and absent in the parents. Edge colors reflect the samples in which the connected pairs of kmers are found. Edges that are part of the bubble (variant call) are displayed with thicker lines.

All simple variants will have this basic structure: a bubble in the graph that separates the variant samples from the non-variant samples. The only major difference is the length of each branch: longer for an insertion in the child, shorter for a deletion (note that for short events, this is generally not apparent from the display, as evidenced by Figures 4.7 and 4.8).

Many variants may occur on the haplotypic background of one parent and not the other. This is common in regions of the genome that are divergent between the two parents. Figure 4.9 depicts one such simulated event. A 41-bp tandem duplication has occurred on the background of the mother (evidenced by the presence of green edges), but not the father (thus the absence of blue edges). In the flanking tails, edges shared between all three samples are present until a blue edge separates from the graph and connects to different vertices. While not shown, these branches continue along the genome of the

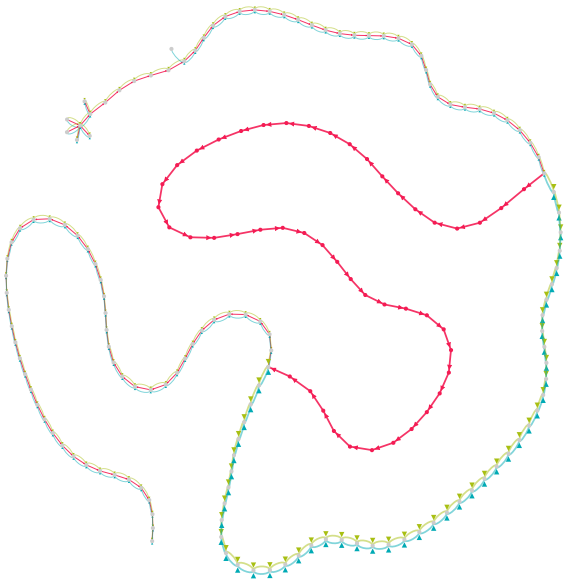

Figure 4.6: A multi-color de Bruijn graph at $k = 47$ for a haploid pedigree spanning a simulated *de novo* SNP, produced by our VisualCortex software. Vertex labels have been supressed for clarity. Spatial layout is arbitrary and for display purposes only.

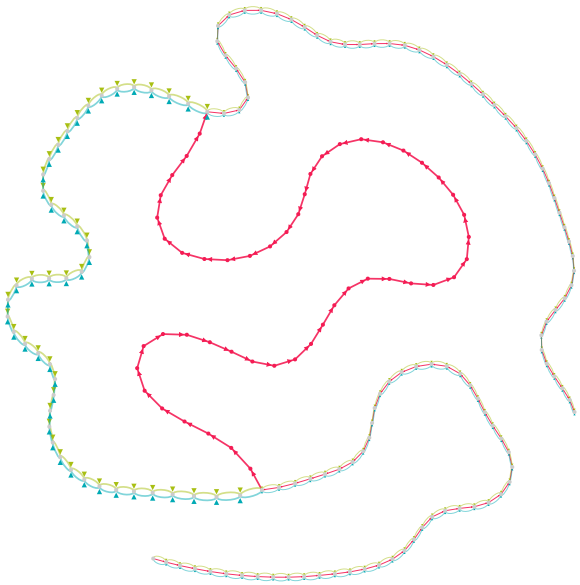

Figure 4.7: A 5 bp insertion in the child

father.

Finally, it is possible to encounter variants where the path through the graph taken by

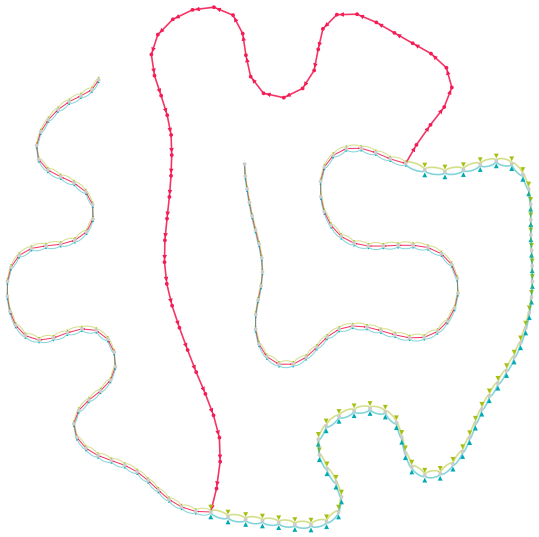

Figure 4.8: A 5 bp deletion in the child

the child can appear to follow both the variant and non-variant paths, as demonstrated by Figure 4.10. Such a scenario may arise by a mutation on a sequence with copy number greater than 1: both the unaltered and altered sequences would then exist simultaneously in the child's genome.

4.2.2 *Complex variant motifs*

Recombination events (allelic crossovers or gene conversion events; NAHR events) will not necessarily appear as bubbles. Bubbles form in the graph when parental and progeny haplotypes diverge (at the site of a variant) and reconnect (at the flanking homologous regions). In a recombination event, the haplotypes do not necessarily reconnect. In a crossover or gene conversion event, as in Figure 4.11, the progeny's graph should follow one parent or the other, switching at the crossover site. Gene conversions and other multiple crossovers may switch back and forth several times. These events can be detected simply by keeping track of which parent's graph is apparently being followed. However, we caution the reader that it's quite likely that many events of this nature will likely go uncalled or improperly called. For such recombination events to be detected, a kmer spanning two proximal variants must be present. This is unlikely to occur for simple crossovers, particularly in genomes of reasonably low heterozygosity, as neighboring

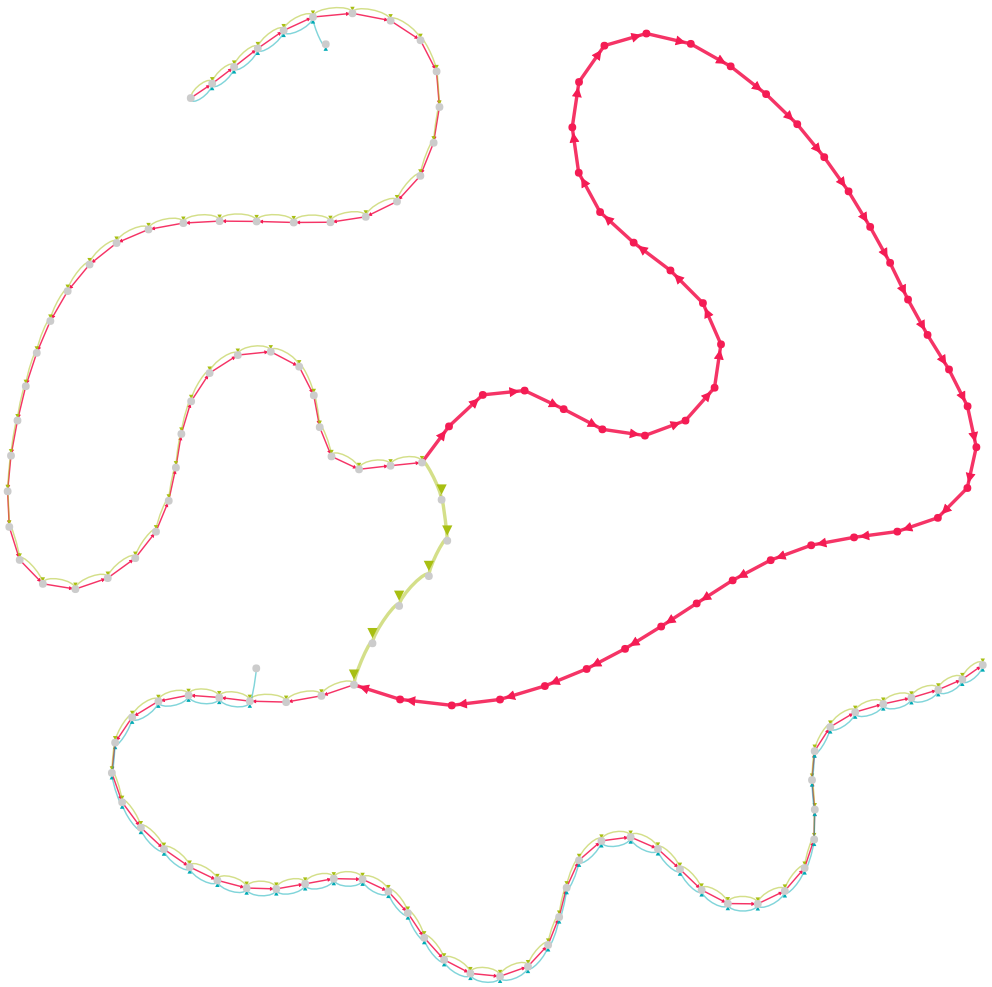

Figure 4.9: A tandem duplication on the haplotypic background of the mother.

variants beyond a kmer's length away will not give rise to novel kmers necessary for the event's detection. It is perhaps slightly more likely for gene conversion events, where the multiple crossovers proximal to a variant exclusive to one of the parents will generate the sought-after novel kmer signal.

NAHR events are trickier; as these events are generally mitotic rather than meiotic events, the expected motif is that a child's graph should follow the same parent, but connect disjoint components of the graph (e.g. telomeres of different chromosomes) through novel kmers. In principle, one should be able to detect such an event by testing whether removing the child's contribution to the pedigree subgraph results in disrupting the otherwise connected components.[48] In practice, however, NAHR events are mediated by homology between low-complexity regions of the subtelomeric genomic regions. The homology will result in confounding connections between disparate regions of the graph.

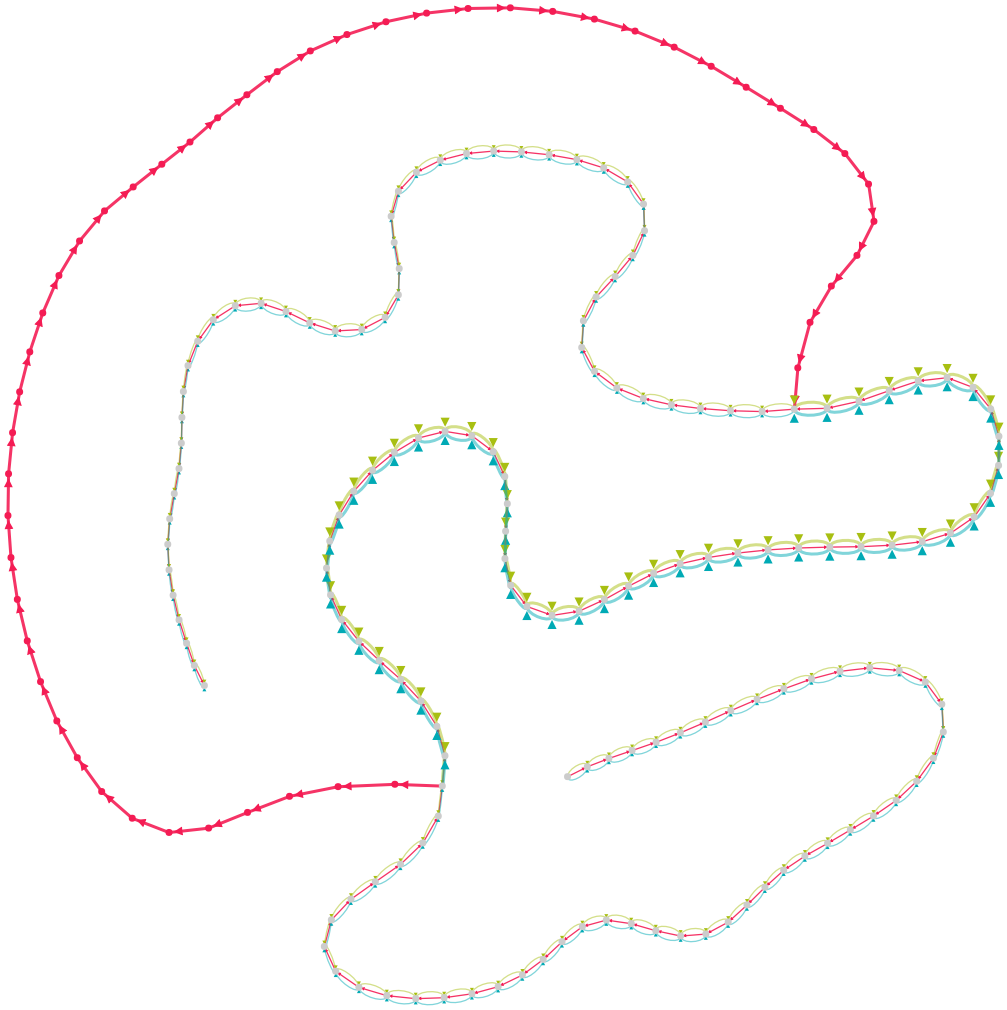

Figure 4.10: A variant wherein the child's path does not simply diverge from that of the parents, but rather navigates both.

An easier solution is to track the parent apparently being copied from and determine the chromosome of origin for each kmer present in the flanking regions of the novel kmers. This is only feasible if one happens to have draft reference genomes for which a kmer's chromosome of origin can be approximately determined.

4.2.3 Handling errors in sequencing

Bubble and non-bubble motifs are trivial to find and navigate if there are no errors in the sequence data, but this situation rarely arises in real data. Real data is subject to sequencing errors, making graph traversal much more difficult. Errors manifest as extraneous branches in the graph, adding ambiguity to traversals. Without a guide as to which branch to explore at a junction, we are either forced to abandon the traversal, make

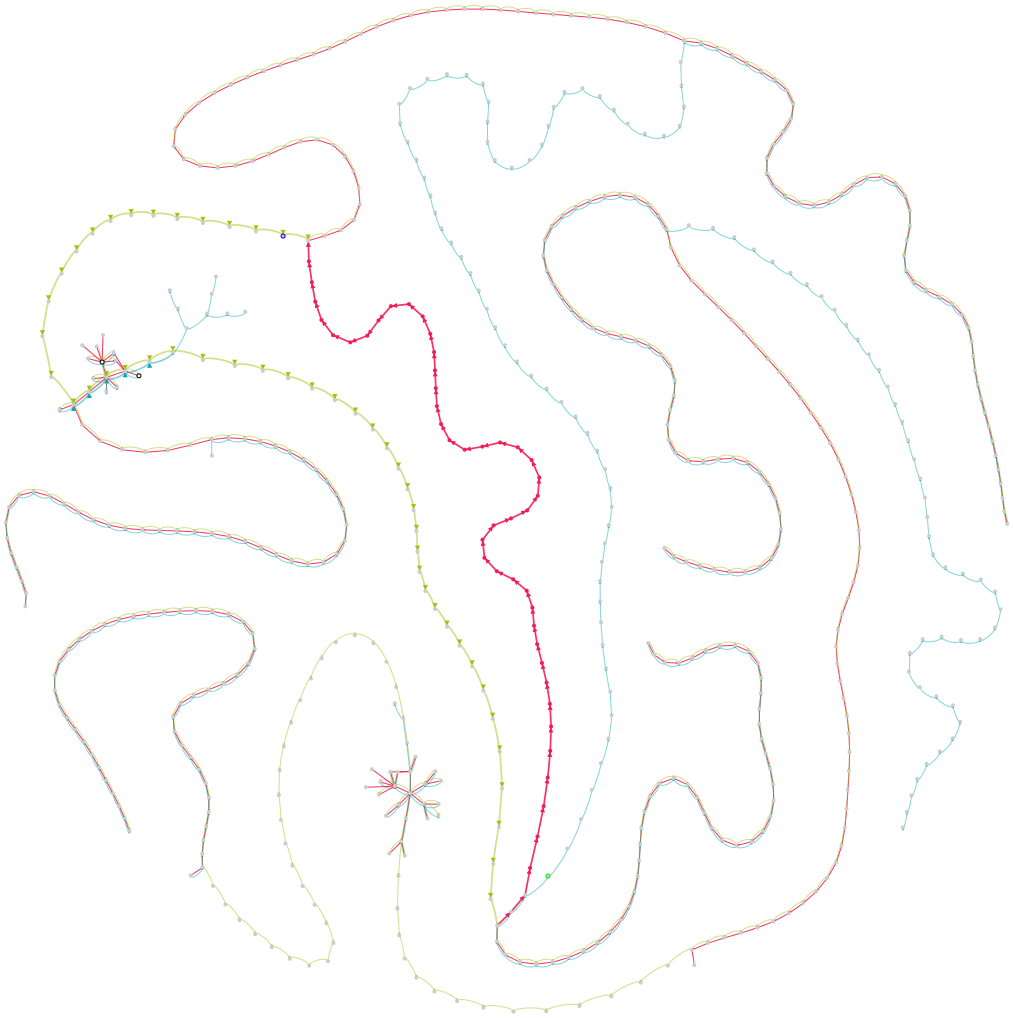

Figure 4.11: A gene conversion event

a guess, or explore all possible branches. The first option is overly conservative; many variants will go untyped. The second is hazardous; there is the very real potential for choosing erroneously and typing the variant incorrectly. The last is computationally expensive; errors explode the complexity of the graph, making it prohibitively costly to find the correct path through the graph.

To solve this, recall that DNMs do more than open up a bubble motif in the graph. Ideally, each kmer along the variant path is novel. If we assume that branches following the novel branch at junctions are correct and linked with the current variant being explored, we can use these novel kmers as "sign posts" to mark successful traversals. Navigating a branch and not seeing a sign post gives us adequate cause to abandon a branch in favor of another.

Figure 4.12a-b depict a simulated indel in imperfect data, the former with some of

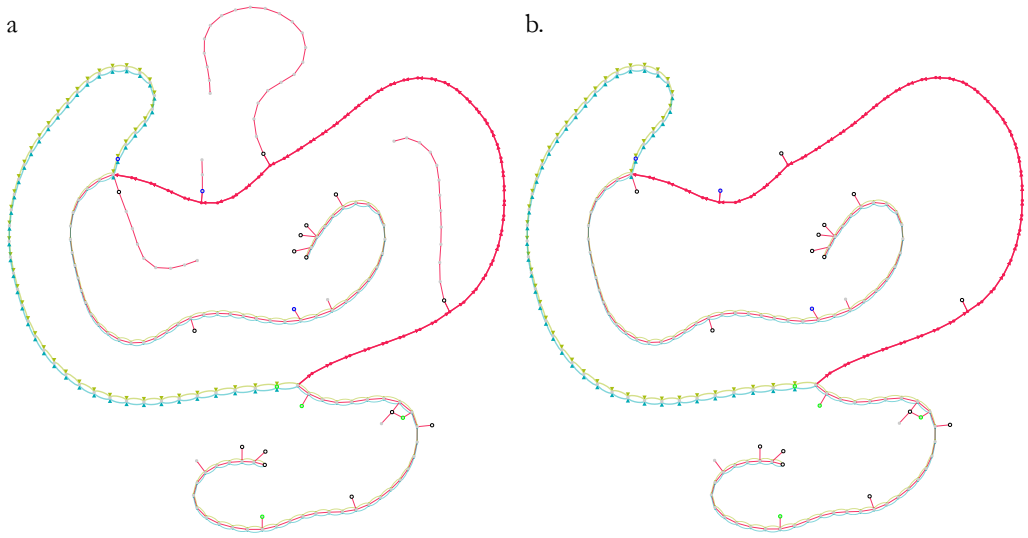

Figure 4.12: Indel with sequencing errors in graph. a. Selected extraneous branches expanded for illustrative purposes b. All extraneous branches collapsed.

these extraneous branches displayed, the latter with them suppressed. Branches with novel kmers (the red vertices) clearly complete the variant, while branches lacking these novel kmers are superfluous to the traversal and can be discarded without loss. This limits the amount of unnecessary traversal in the graph, making it easier to find paths through the parental and child colors to form the variant.

4.3 *Calling and classifing de novo variants*

Armed with an intuition as to how graphs behave in regions of *de novo* variation, we can now describe the procedure for identifying and classifying a variant. The overview involves five big steps (and associated substeps):

1. Identify confident and trusted novel kmers
2. Construct multi-color de Bruijn "trio" graphs (child, mother, father)
3. Load subgraph local to a novel kmer
4. Identify and classify variants in the subgraph
5. Evaluate performance

We discuss these in details in the sections below.

4.3.1 *Identify confident and trusted novel kmers*

We first seek to build a list of novel kmers that are both *confident* (i.e. unlikely to be sequencing errors) and *trusted* (i.e. are unlikely to be the result of contamination). Identification of the novel kmers themselves is trivial; we simply build a list of kmers that appear in the child but are completely absent in the parents. The subsequent filtering steps are described below.

4.3.1.1 *Remove low coverage kmers*

For a deeply sequenced sample, we expect all kmers in the genome to be of similarly high coverage. While there will inevitably be regions of the genome where coverage is poor owing to failure to amplify regions with high GC content, the Lander-Waterman statistics in Chapter 1 suggest we should easily see many copies of the entire *P. falciparum* genome at a coverage of $100x$. We can therefore assume that failure to reach a certain coverage threshold is indicative of sequencing error, and such kmers can be removed as candidates from the novel kmer list.

The problem remains as to where the threshold should be set. For each sample, we plotted the histogram of kmer coverage, shown in Figure 4.13, smoothing the resulting distribution with a non-parametric LOESS fit. The smoothed histogram makes it easier to find the first local minimum using Algorithm 6.

Algorithm 6 Compute the local minimum of a kmer coverage distribution

```
1: function firstLocalMinimum(coverageHist)
2:     y = laggedDifferences(c(INT_MAX, x)) > 0L
3:     y = cumSum(equalRunLengths(y).lengths)
4:     y = y[seq(2L, length(y), 2L)]
5:     return(y[2])
```

4.3.1.2 *Remove possible contaminants*

Contamination can occur during sequencing library preparation due to handling from human operators (transferring either bacterial or human genetic material to the library) or from other samples (often from different species) being processed in the same laboratory. Contamination would result in kmers that appear novel - owing to their absense in the parents - but are irrelevant for our study. It is perhaps not a paramount concern when processing *P. falciparum* data, as the genome is very different than any other sample likely to be a contaminant. However, it may contribute false-positives that we can easily mitigate.

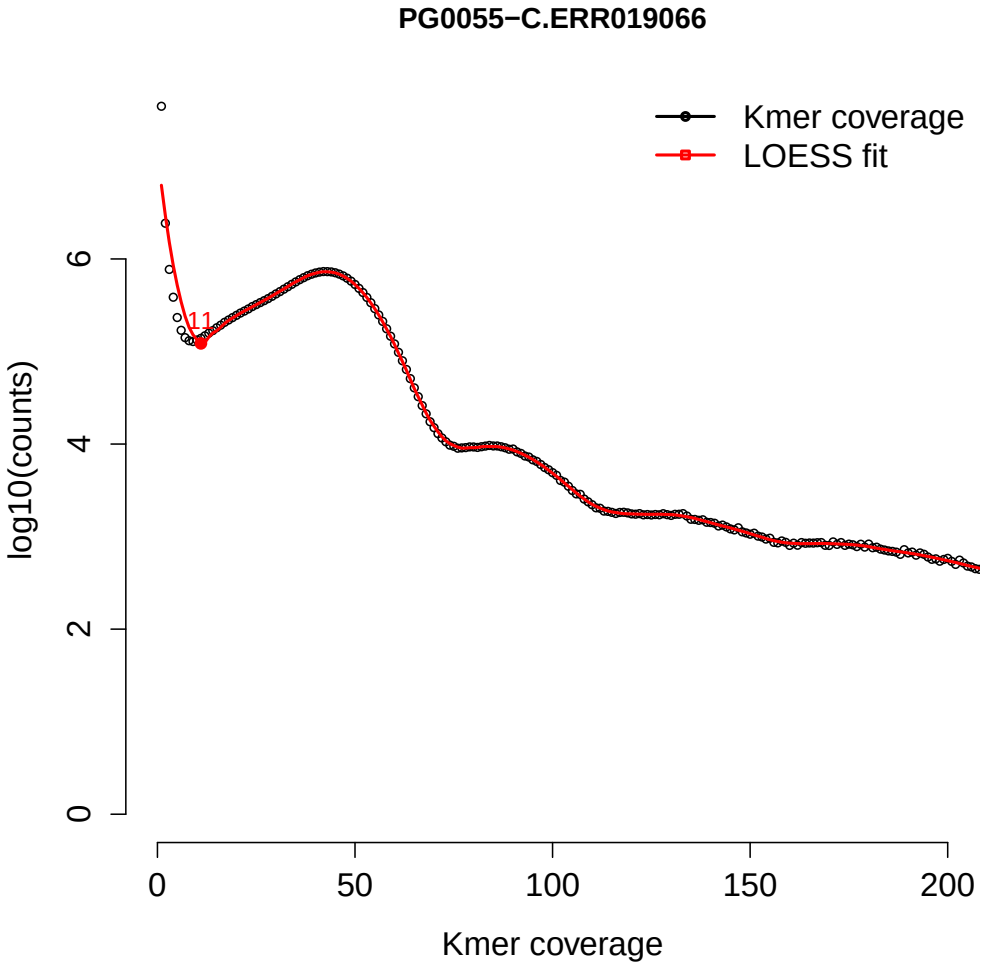

Figure 4.13: Kmer coverage histogram for a real sample, with LOESS fit

To remove the effects of contamination, we run every confident novel kmer through BLAST.[49] Specifically, we used the `blastn` package and all available BLAST nucleotide databases to identify the likely species of every confident novel 47-mer in each sample. Any unidentified kmer or apparently *P. falciparum* kmer was retained; all others were removed. In practice, this removes anywhere from dozens to thousands of kmers from needing to be considered; as evidenced by Figure 4.14, the exact number varies as each sample is prepared independently, at different times and by different personnel.

4.3.2 Construct multi-color de Bruijn "trio" graphs

To construct the "trio" graphs, we perform assembly on each sample with the *Cortex de novo* assembly software[27] following the recommended workflow.[45] Briefly, each sample is

assembled using the `build` command at a kmer size of 47 bp[3] and ignoring nucleotides with an Illumina quality score less than 5. Each sample was then cleaned of likely sequencing errors with the `clean` command using automatically calculated coverage and supernode (unambiguous runs of kmers with in/out degree of 1) length thresholds. Finally, the graph for the child was merged into a *clean* trio graph, and separately, a *dirty* trio graph (one using the uncleaned graph data) using the `join` command. This multi-color graph consists of child, mother, and father. For our purposes with *P. falciparum*, "child" is assigned color 0, "mother" (the first parent of the cross) to color 1, and "father" to color 2. Read threading was *not* applied, as in our analyses, there is no need for contigs, just the graph data structure.

4.3.3 Load subgraph local to a novel kmer

To facilitate variant calling, we must process regions of the graph likely to harbor DNMs. While it is technically possible to load a *P. falciparum* graph into RAM (owing to its small 23 megabase genome), it is unlikely such a solution would scale to larger genomes. It is also cumbersome to do so when there are only on the order of dozens, perhaps hundreds, of variants to be discovered per genome. Therefore, we adopted a solution of fetching only relevant parts of the genome as necessary, operating on the local subgraph surrounding the putative variant, rather than on the entire graph at once.

4.3.3.1 Depth-first search

Graph exploration is an *online* problem, meaning the structure of the graph cannot be known until it is explored. As a non-linear data structure, it is not trivial to determine where to start and stop exploring a graph. During traversal, one may encounter junctions (due to errors or homology) without any additional information as to which branch to choose. Graphs sometimes loop back onto themselves, necessitating that we keep track of our walk so that we do not end up traversing endlessly in circles. Incorrect decisions in the traversal cannot always be detected, requiring appropriate stopping conditions to abort a traversal if no fruitful data is discovered.

Typically, graph exploration can be accomplished with a so-called *depth-first search*, or DFS. The basic premise of a DFS is summarized in Algorithm 7: start at a vertex, walk in a chosen direction until a junction is encountered, choose one branch and repeat the DFS from that point until it is deemed appropriate to stop, then jump back to the junction to choose the next branch, and repeat until completion. In practice, this approach has some

[3]This setting results from evaluations on optimal kmer size for maximizing contig length, despite not needing to produce contigs for our analyses

drawbacks that manifest quickly in real data. First, the basic DFS algorithm terminates only when there are no more vertices left to traverse, which is overkill for our purposes. Second, all branches are treated equally. For our purposes, branches containing errors are not important and should be discarded lest they confuse later algorithms trying to find paths through bubbles in order to type variants. Third, this requires us to explore three graphs separately, which is inefficient.

Algorithm 7 A basic, iterative depth-first search

```
1:  function IDFS(graph, vertex)
2:      s = new Stack()
3:      visited = {}
4:      s.push(vertex)
5:      while !s.isEmpty() do
6:          current = s.pop()
7:          if (visited.contains(current)) then
8:              next
9:          visited.add(current)
10:         for v in graph.nextVertices(vertex) do
11:             s.push(v)
```

The solution is to instead conduct a DFS with stopping conditions and recursively. Stopping conditions, specifying the conditions upon which a traversal is deemed "successful" or "failed" allow us to decide certain branches in the subgraph are unfruitful for analysis. The recursive traversal allows us to act on the result of the stopping condition, adding it to the subgraph if successful, discarding it if not. This is described in Algorithm 8.

Stopping conditions are implemented as a callback object, permitting programmer-specified limits for different situations. To type DNMs, we begin traversal at a novel kmer, walking forward and backward in the graph until the stopping conditions are met. We then explore the parental graphs based on the subgraph we loaded for the child. As the parental traversals have some additional information (namely, the presence of the child's subgraph allows us to check if a parental traversal has diverged and rejoined from the graph), the stopping conditions are different.

The stopping condition callback object implements two boolean methods: `hasTraversalSucceeded` and `hasTraversalFailed`. Both of them may return `false`, in which case the traversal continues. If either returns `true`, traversal is halted and the branch is evaluated for retention or rejection.

Algorithm 8 The recursive depth-first search with arbitrary stopping conditions

```
1: function RDFS(clean, dirty, kmer, color, g, stopper, depth, goForward, history)
2:     firstKmer = kmer
3:     sourceKmersAllColors = goForward ? getPrevKmers(clean, dirty, kmer) : getNextKmers(clean, dirty, kmer)
4:     sourceKmers = sourceKmersAllColors.get(color)
5:     dfs = new AnnotatedGraph()
6:     repeat
7:         cv = kmer
8:         cr = clean.findRecord(cv)
9:         if (cr == null && dirty != null) then
10:            cr = dirty.findRecord(cv)
11:        prevKmers = getPrevKmers(clean, dirty, cv)
12:        nextKmers = getNextKmers(clean, dirty, cv)
13:        adjKmers = goForward ? nextKmers : prevKmers
14:        addVertexAndConnect(dfs, cv, prevKmers, nextKmers)
15:        if (stopper.keepGoing(cr, g, depth, dfs.vertexSet().size(), adjKmers.get(color).size()) && !history.contains(kmer)) then
16:            history.add(kmer)
17:            if (adjKmers.get(color).size() == 1) then
18:                kmer = next(adjKmers.get(color))
19:            else if (adjKmers.get(color).size() != 1) then
20:                childrenWereSuccessful = false
21:                for (ak in adjKmers.get(color)) do
22:                    branch = dfs(clean, dirty, ak, color, g, stopperClass, depth + isNovelKmer(cr) ? 0 : 1, goForward, history)
23:                    if (branch != null) then
24:                        addGraph(dfs, branch)
25:                        childrenWereSuccessful = true
26:                if (childrenWereSuccessful || stopper.hasTraversalSucceeded(cr, g, depth, dfs.vertexSet().size(), 0)) then
27:                    return dfs
28:        else if (stopper.traversalSucceeded()) then
29:            return dfs
30:        else
31:            return null
32:    until (adjKmers.get(color).size() == 1)
33:    return null
```

4.3.3.2 *Stopping conditions for child*

The child's stopping conditions on traversal success or failure are provided in Algorithm 9 and 10, respectively. For the child, success is approximately determined by having explored a novel kmer stretch in the graph to the point that it has rejoined the parental graphs. However, we purposefully continue reading another 50 kmers before returning success. If more novel kmers are recovered in that span, we reset our counters and continue walking. This facilitates two things: the absence of novel kmers due to sequencing errors or overthresholding, and typing complex variants that may have short stretches of non-novel kmers. Failure is determined by a number of criteria, including the absence of novel kmers, low complexity regions, having no more branches to explore, having reached a maximum graph depth, or having reached a maximum graph size.

Algorithm 9 Child's traversal success determination method

```
1: function hasTraversalSucceeded(cr, g, depth, size, edges)
2:     if (goalSize == 0 && (cr.getCoverage(1) > 0 || cr.getCoverage(2) > 0)) then
3:         goalSize = size
4:         goalDepth = depth
5:     if (goalSize > 0 && isNovel(cr)) then
6:         goalSize = size
7:         goalDepth = depth
8:     return (goalSize > 0 && (size >= goalSize + 50 || isLowComplexity(cr) || edges
   == 0))
```

Algorithm 10 Child's traversal failure determination method

```
1: function hasTraversalFailed(cr, g, depth, size, edges)
2:     return !isNovel(cr) && (isLowComplexity(cr) || edges == 0 || depth >= 5 || size
   > 5000)
```

4.3.3.3 *Stopping conditions for parents*

The parents' stopping conditions on traversal success or failure are provided in Algorithm 11 and 12, respectively. Success is determined by having diverged from the child's graph and rejoined it. Care is taken to ensure that we have rejoined the graph at a boundary of the novel kmer stretch, rather than some ther part of the graph obtained when trying to read some extra flanking data in Algorithm 9. Failure is determined by a number of criteria, including having reached a maximum graph size, having reached a maximum graph depth, or low complexity regions.

Algorithm 11 Parents' traversal success determination method

```
1: function hasTraversalSucceeded(cr, g, depth, size, edges)
2:     fw = cr.getKmerAsString()
3:     rc = reverseComplement(fw)
4:     v = null
5:     rejoinedGraph = false
6:     if (g.containsVertex(fw) || g.containsVertex(rc)) then
7:         rejoinedGraph = true
8:         for av in g.vertexSet() do
9:             if (av.getKmer().equals(fw) || av.getKmer().equals(rc)) then
10:                if (!sawPredecessorFirst && !sawSuccessorFirst) then
11:                    if (av.flagIsSet("predecessor")) then sawPredecessorFirst = true
12:                    else if (av.flagIsSet("successor")) then sawSuccessorFirst = true
13:                if ((sawPredecessorFirst && av.flagIsSet("predecessor")) || (sawSuccessorFirst && av.flagIsSet("successor"))) then
14:                    rejoinedGraph = false
15:                    break
16:    return size > 1 && rejoinedGraph
```

Algorithm 12 Parents' traversal failure determination method

```
1: function hasTraversalFailed(cr, g, depth, size, edges)
2:     return size > 1000 || junctions >= 5 || isLowComplexity(cr)
```

4.3.4 Identify and classify variants in the subgraph

With the relevant subgraph now loaded, we can now attempt to type variants. Typing involves three steps:

1. Annotate vertices in the graph that can be possible start and end points of the variant bubble
2. Find the shortest path from start to end that satisfies some conditions
3. From the haplotypes, remove the flanking homologous sequence to reveal the variant alleles

Let us first detail how we annotate the viable starts and ends of the variant, which simply amounts to iterating through each vertex in the subgraph and checking that it means various conditions. A variant start (end) vertex should have out degree (in degree) greater than 1. The branches should be color-specific to reflect the opening of a bubble between the different samples in the graph. This is detailed in Algorithm 13.

Algorithm 13 Annotating possible variant starts and ends of the subgraph

```
function annotateStartsAndEnds(b)
    for av in b.vertexSet() do
        if (b.outDegreeOf(av) > 1) then
            aes = b.outgoingEdgesOf(av)
            childEdges = {}
            parentEdges = {}
            for (AnnotatedEdge ae in aes) do
                if (ae.isPresent(0) && ae.isAbsent(1) && ae.isAbsent(2)) then
                    childEdges.add(ae)
                if (ae.isPresent(color)) then
                    parentEdges.add(ae)
            if (childEdges.size() > 0 && parentEdges.size() > 0) then
                av.setFlag("start")
                candidateStarts.add(av)
        if (b.inDegreeOf(av) > 1) then
            aes = b.incomingEdgesOf(av)
            childEdges = {}
            parentEdges = {}
            for AnnotatedEdge ae in aes do
                if ae.isPresent(0) && ae.isAbsent(1) && ae.isAbsent(2) then
                    childEdges.add(ae)
                if ae.isPresent(color) then
                    parentEdges.add(ae)
            if (childEdges.size() > 0 && parentEdges.size() > 0) || beAggressive then
                av.setFlag("end")
                candidateEnds.add(av)
```

4.3.4.1 *Dijkstra's shortest path algorithm*

With all of the start and end points now annotated, we now need to find a path from one end of the putative variant to the other. The number of possible paths could be very large. We shall make the assumption that the correct path is the shortest path. While this will often be the case, we note that the shortest path is not necessarily the biological path. This could be the case in highly repetitive regions longer than a kmer length. Since de Bruijn graphs tend to collapse long repeats, we may miss some events.

E. W. Dijkstra described his shortest path algorithm in 1959.[50] We describe it below in Algorithm 14. Briefly, we keep track of all vertices' distance from the source vertex, setting the source's distance to itself to 0 and all others to infinity (to denote as-of-yet unvisited vertices). We then select the vertex with the minimum distance to the source (in the first iteration, the source itself) and compute a new distance to all immediately adjacent vertices. This new distance is a sum of the distance traversed so far from the source to one of these vertices. For our purposes, we shall assume the distance between two adjacent vertices is always 1. If the distance computed is less than the distance recorded, we replace the old value with the new. We remove this vertex from the processing queue and proceed to the next vertex with the lowest distance from the source.

To use this algorithm for allele identification, we iterate through all possible combinations of start and stop vertices, obtained as described in the previous section. We then iterate through the three graph colors (representing the child, mother, and father). For each color, we apply Algorithm 14. For the child, we place the additional constraint that the path accepted must contain at least one novel kmer.

This algorithm will return the child and parental haplotypes. To identify the precise alleles of the event, we simply trim back the homologous regions of the haplotypes with Algorithm 15.

4.3.4.2 *Classify event*

For simple variants (those that conform to the bubble motif), event classification is reasonably straightforward. We simply inspect the recovered alleles and evaluate them against simple rules. For example, a SNP should be a single nucleotide in length. An insertion should have a parental allele length of 1 and a child allele length > 1.

To classify complex variants, we rely on other heuristics. GC events are classified by keeping track of which parent the child's genome appears to be exclusively copying from (simply by measuring when kmer coverage has dropped from one parent and returned in the other), detailed in Algorithm 16. NAHR events, involving recombinations between

Algorithm 14 Finding the shortest path in a graph

```
function DSPA(graph, source, destination, color)
    dist = {}
    prev = {}
    q = []
    for all v in g.vertexSet() do
        dist[v] = infinity
        prev[v] = null
        push(q, v)
    dist[source] = 1
    while !q.isEmpty() do
        u = vertexWithMinDistance(q, dist)
        if u == destination then
            break
        q.remove(u);
        if u != -1 then
            for all e in g.outgoingEdgesOf(u, color) do
                v = g.getEdgeTarget(e, color)
                alt = dist[u] + 1
                if alt < dist[v] then
                    dist[v] = alt
                    prev[v] = u
    s = []
    Integer u = destination
    while u != null && prev.containsKey(u) do
        push(s, u)
        u = prev[u]
    return s
```

Algorithm 15 Trim back haplotypes to reveal alleles

```
function TRIMHAPLOTYPES(child, parent)
    eo = child.length() - 1
    e1 = parent.length() - 1
    s = 0
    length = (child.length() < parent.length() ? child.length() : parent.length())
    for (s = 0; s < length && child[s] == parent[s]; s++) do
        (do nothing)
    while (eo > s && e1 > s && child[eo] == parent[e1]) do
        eo–
        e1–
```

different chromosomes, are detected by examining if any kmers are uniquely found on different chromosomes, detailed in Algorithm 17.

The classification algorithm can be described by the decision tree in Figure 4.15.

4.3.4.3 *Choosing haplotypic background*

When calling variants, we do not know the haplotypic background upon which a variant has occured. We must compare the child's graph to the mother's and then to the father's, making separate calls. This results in two variant calls for the same event. A single event must be chosen. In cases where the child and parental alleles are identical, this is trivial. Additionally, variants where the event can be identified against one parent but not the other are straightforward. The problematic events are those that have conflicting descriptions between parents. In this situation, we heuristically assign a score for various properties of the variant, choosing the representation with the highest score. This has the effect of preferring simpler descriptions (e.g. "SNP") to more complex ones (e.g. "GC").

4.3.4.4 *Mark traversed novel kmers as used*

We then mark all the novel kmers we saw used in the stretch as used so we do not process them again. This allows us to keep track of our progress, only acting on kmers that have not been associated to any variant yet.

4.3.5 *Evaluate performance*

We evaluated the performance of our graphical DNM caller by running the thing on some simulated data. Note that the way a variant is simulated and the way a variant is called are not necessarily identical. In particular, indels are tricky because there is not a standard representation in graphs. Usually, when indels are called in reference-based methods, the reference is taken to be the forward strand and indels are left-shifted as far as possible. In graphs, there is no information available for determining orientation. When they were simulated, we knew what the forward strand was, but we do not know that in the graph. Thus, when we go to check on the presence of a variant, we must check it in both orientations, and accounting for multiple representations.

4.3.5.1 *Pre-compute novel kmer to variant map*

We iterated through all variants, extracting sequence from the simulated child's reference genome between start $-(2k-1)$ and stop $+(2k-1)$ bp. We then extracted each kmer from this sequence and, if the kmer is novel, emitting a table row mapping the novel kmer to variant ID, variant type, and position in the child's reference genome. Note that

Algorithm 16 Stretch has switches

```
function hasSwitches(graph, stretch)
    inherit = []
    for all 47-bp kmers k in stretch do
        cov0 = graph.getCoverage(k, 0)                    ▷ child
        cov1 = graph.getCoverage(k, 1)                    ▷ mother
        cov2 = graph.getCoverage(k, 2)                    ▷ father
        if (cov0 > 0 && cov1 == 0 && cov2 == 0) then
            append(inherit, "C")
        else if (cov0 > 0 && cov1 > 0 && cov2 == 0) then
            append(inherit, "M")
        else if (cov0 > 0 && cov1 == 0 && cov2 > 0) then
            append(inherit, "D")
        else if (cov0 > 0 && cov1 > 0 && cov2 > 0) then
            append(inherit, "B")
    for i in inherit.length() do
        for inherit[i] == 'B' do
            prevContext = '?'
            nextContext = '?'
            for (j = i - 1; j >= 0; j–) do
                if (inherit[j] == 'M' || inherit[j] == 'D') then
                    prevContext = inherit[j]
                    break
            for (j = i + 1; j < inherit.length(); j++) do
                if (inherit[j] == 'M' || inherit[j] == 'D') then
                    nextContext = inherit[j];
                    break;
            context = '?';
            if (prevContext == nextContext && prevContext != '?') then
                context = prevContext
            else if (prevContext != nextContext) then
                if (prevContext != '?') then
                    context = prevContext
                else
                    context = nextContext
            inherit[i] = context
    return inheritStr.matches(".*D+.C+.M+.*") || inheritStr.matches(".*M+.C+.D+.*")
```

Algorithm 17 Stretch has chimeras

```
function hasChimeras(stretch, lookup)
    chrCount = {}
    for all kmers k in stretch do
        if lookup.numAlignments(k) == 1 then
            chrCount[lookup.getFirstAlignment(k).getChr()]++
    return chrCount.size() > 1
```

Algorithm 18 Score variant

```
function chooseVariant(gvc)
    scores = []
    for all colors c do
        if (gvc.traversalIsComplete(c)) then
            scores[c]++
        if (gvc.variantType(c) != "unknown" then
            scores[c]++
        if (gvc.variantType(c) not in ("GC", "NAHR")) then
            scores[c]++
    bestColor = whichMax(scores)
    return (scores[0] == scores[1] ? 0 : bestColor)
```

because we chose to space our variants out over considerable distance, it is generally not possible for a kmer to map to multiple variants. However, as we have placed very few constraints on variant positioning otherwise, it is possible a simulated variant has landed in a low-complexity region that occurs multiple times throughout the genome, and that multiple variants thus share novel kmers. In that instance, the first variant we see during processing is assigned the novel kmer.

4.3.5.2 Load variant containing a novel kmer and comparing

If we are in evaluation mode (that is, if we've a novel kmer to variant map along with a dataset), then after each variant we call, we check if any of the kmers involved in the variant call are in the map, and load the relevant variant information. We then evaluate our call using Algorithm 19.

4.4 Results on simulated data

We ran our algorithm on the perfect and realistic simulated datasets presented in Chapter 3. Looking first at purely event recovery without classification (i.e. did we find *de novo* variants, irrespective of whether we classified them correctly), we summarize our stats in Tables 4.2 and 4.3. In both cases, our sensitivity and specificity to DNMs is very high - greater than 98% in nearly all cases. Note that the true negatives (tn) are effectively every kmer that we did *not* call in our dataset, which effecitvely makes our specificity nearly perfect, as the use of the novel kmers prevents us from making calls in the vast majority of the graph.

Additionally in these tables, we also computed the "redundant call", or "rc" metric. The rc metric reveals an important caveat regarding graph calls: should the traversals fail and the alleles of the variant not ascertained, the novel kmers involved in the variant will

Algorithm 19 Evaluate variant

```
function evalVariant(call, truth, stretch)
    relevantVariants = []
    for all kmers in stretch do
        if (truth.contains(kmer)) then
            push(relevantVariants, truth.get(kmer))
    bestVariant = null;
    for all vi in relevantVariants do
        ref = call.getParentalAllele()
        alt = call.getChildAllele()
        refStretch = call.getParentalStretch()
        altStretch = call.getChildStretch()
        found = false;
        if (!found) then                                   ▷ left-shift variants and check
            pos = call.getStart()
            while (pos >= 0 && pos + ref.length() < refStretch.length() && pos +
alt.length() < altStretch.length()) do
                refFw = refStretch.substring(pos, pos + ref.length())
                altFw = altStretch.substring(pos, pos + altLength)
                refRc = reverseComplement(refFw);
                altRc = reverseComplement(altFw)
                if (known ref and alt alleles match called fw or rc alleles) then
                    ref = (refFw or refRc)
                    alt = (altFw or altRc)
                    found = true;
                    break;
                pos−
        if (!found) then                                   ▷ right-shift variants and check
            pos = call.getStart()
            while (pos >= 0 && pos + ref.length() < refStretch.length() && pos +
alt.length() < altStretch.length()) do
                refFw = refStretch.substring(pos, pos + refLength)
                refRc = reverseComplement(refFw)
                altFw = altStretch.substring(pos, pos + altLength)
                altRc = reverseComplement(altFw)
                if (known ref and alt alleles match called fw or rc alleles) then
                    ref = (refFw or refRc)
                    alt = (altFw or altRc)
                    found = true;
                    break;
                pos++
            ▷ Maybe what we've found is a truncated version of what we were expecting
        knownRef = vi.ref
        knownAlt = vi.alt == null ? "" : vi.alt
        if (!found && knownRef.length() > ref.length() && knownAlt.length() >
alt.length() && knownRef.length() == knownAlt.length()) then
            refFw = ref;
            altFw = alt;
            refRc = reverseComplement(refFw);
            altRc = reverseComplement(altFw);
            refFinal = null, altFinal = null;
            if (knownRef contains refFw or refRc and knownAlt contains altFw or altRc)
then
```

not be marked as used. However, we still emit a variant "event", despite our inability to classify it. In the subsequent iteration of the algorithm, the remaining novel kmers will be picked up for calling again, leading to the same variant being emitted multiple times. Thus, we must exercise caution with untyped variants: the rate at which they appear in our callset may be slightly higher (up to 10%) than the rate at which they truly exist in the genome.

Results on event classification are shown as heatmaps in Figures 4.16 and 4.17, with observed events on the bottom and expected events on the side. On the observed axis, an "unknown" event denotes a variant that could not be typed. On the expected axis, an "unknown" event is one that does not appear in the simulation list (i.e. a false positive). The total number of events simulated that could possibly be recovered via novel kmers is the sum of each row (except for the "unknown" row, which instead enumerates the false positives and the types they've been assigned). For the most part, variants appear on the diagonal, indicating proper classification. Performance degrades when we move into the non-bubble motif variants (i.e. GC and NAHR) events.

Gene conversion events are quite often erroneously described as SNPs. This is likely due to the fact that the classification algorithm is looking for clear switches of parental copying in the child (copying from mother, then father, then mother again, or vice versa). However, if variants that appear on different haplotypic backgrounds are too close to one another, 47-bp kmers might span both, and the recombination motif that we seek may be obscured and cause the algorithm to call a SNP instead.

Many NAHR events are classified as "unknown". This is perhaps not unreasonable. Our classification algorithm for NAHR events (Algorithm 17) requires that the stretch have kmers from different chromosomes. However, if the stretch truncates early due to errors or homology, there may be insufficient genomic context in order to determine the chromosomes of origin, leaving us unable to classify the variant accordingly.

Table 4.2: ROC metrics on simulated perfect data

sn	sim	fp	fn	tp	tn	rc	sens	spec	prec	npv	fpr	fnr	fdr	acc
5	perfect	1	5	126	22240910	9	0.9618	1	0.9921	1	0	0.0382	0.0079	1
3	perfect	2	3	154	22200660	4	0.9809	1	0.9872	1	0	0.0191	0.0128	1
0	perfect	0	2	106	22241343	7	0.9815	1	1.0000	1	0	0.0185	0.0000	1
12	perfect	0	2	113	22233659	3	0.9826	1	1.0000	1	0	0.0174	0.0000	1
13	perfect	0	2	114	22217297	5	0.9828	1	1.0000	1	0	0.0172	0.0000	1
17	perfect	0	2	117	22242890	6	0.9832	1	1.0000	1	0	0.0168	0.0000	1
1	perfect	1	2	137	22249556	8	0.9856	1	0.9928	1	0	0.0144	0.0072	1
14	perfect	2	2	162	22196410	7	0.9878	1	0.9878	1	0	0.0122	0.0122	1
11	perfect	1	1	114	22207761	2	0.9913	1	0.9913	1	0	0.0087	0.0087	1
6	perfect	1	1	118	22203683	2	0.9916	1	0.9916	1	0	0.0084	0.0084	1
8	perfect	1	1	129	22229379	5	0.9923	1	0.9923	1	0	0.0077	0.0077	1
10	perfect	0	1	130	22238480	2	0.9924	1	1.0000	1	0	0.0076	0.0000	1
15	perfect	1	1	131	22208991	10	0.9924	1	0.9924	1	0	0.0076	0.0076	1
16	perfect	1	1	166	22213928	4	0.9940	1	0.9940	1	0	0.0060	0.0060	1
2	perfect	1	0	105	22225262	3	1.0000	1	0.9906	1	0	0.0000	0.0094	1
4	perfect	2	0	72	22210167	2	1.0000	1	0.9730	1	0	0.0000	0.0270	1
7	perfect	1	0	57	22225612	1	1.0000	1	0.9828	1	0	0.0000	0.0172	1
9	perfect	0	0	107	22255460	2	1.0000	1	1.0000	1	0	0.0000	0.0000	1
18	perfect	2	0	133	22242522	0	1.0000	1	0.9852	1	0	0.0000	0.0148	1
19	perfect	1	0	98	22236313	6	1.0000	1	0.9899	1	0	0.0000	0.0101	1

Table 4.3: ROC metrics on simulated realistic data

sn	sim	fp	fn	tp	tn	rc	sens	spec	prec	npv	fpr	fnr	fdr	acc
5	realistic	4	2	123	77566161	7	0.9840	1	0.9685	1	0	0.0160	0.0315	1
0	realistic	1	1	101	77516712	7	0.9902	1	0.9902	1	0	0.0098	0.0098	1
6	realistic	2	1	107	77289511	2	0.9907	1	0.9817	1	0	0.0093	0.0183	1
13	realistic	0	1	107	77362132	3	0.9907	1	1.0000	1	0	0.0093	0.0000	1
17	realistic	3	1	109	77390562	5	0.9909	1	0.9732	1	0	0.0091	0.0268	1
12	realistic	2	1	111	77440516	3	0.9911	1	0.9823	1	0	0.0089	0.0177	1
16	realistic	1	1	155	77369055	5	0.9936	1	0.9936	1	0	0.0064	0.0064	1
2	realistic	4	0	93	77425427	1	1.0000	1	0.9588	1	0	0.0000	0.0412	1
4	realistic	3	0	65	77312705	2	1.0000	1	0.9559	1	0	0.0000	0.0441	1
3	realistic	6	0	150	77296380	1	1.0000	1	0.9615	1	0	0.0000	0.0385	1
1	realistic	1	0	133	77509177	5	1.0000	1	0.9925	1	0	0.0000	0.0075	1
7	realistic	4	0	56	77445270	1	1.0000	1	0.9333	1	0	0.0000	0.0667	1
8	realistic	6	0	126	77469034	3	1.0000	1	0.9545	1	0	0.0000	0.0455	1
9	realistic	2	0	95	77503142	2	1.0000	1	0.9794	1	0	0.0000	0.0206	1
10	realistic	1	0	124	77398963	2	1.0000	1	0.9920	1	0	0.0000	0.0080	1
11	realistic	2	0	108	77422535	2	1.0000	1	0.9818	1	0	0.0000	0.0182	1
14	realistic	6	0	150	77355056	7	1.0000	1	0.9615	1	0	0.0000	0.0385	1
15	realistic	1	0	125	77435743	9	1.0000	1	0.9921	1	0	0.0000	0.0079	1
18	realistic	4	0	123	77355144	3	1.0000	1	0.9685	1	0	0.0000	0.0315	1
19	realistic	2	0	95	77480228	6	1.0000	1	0.9794	1	0	0.0000	0.0206	1

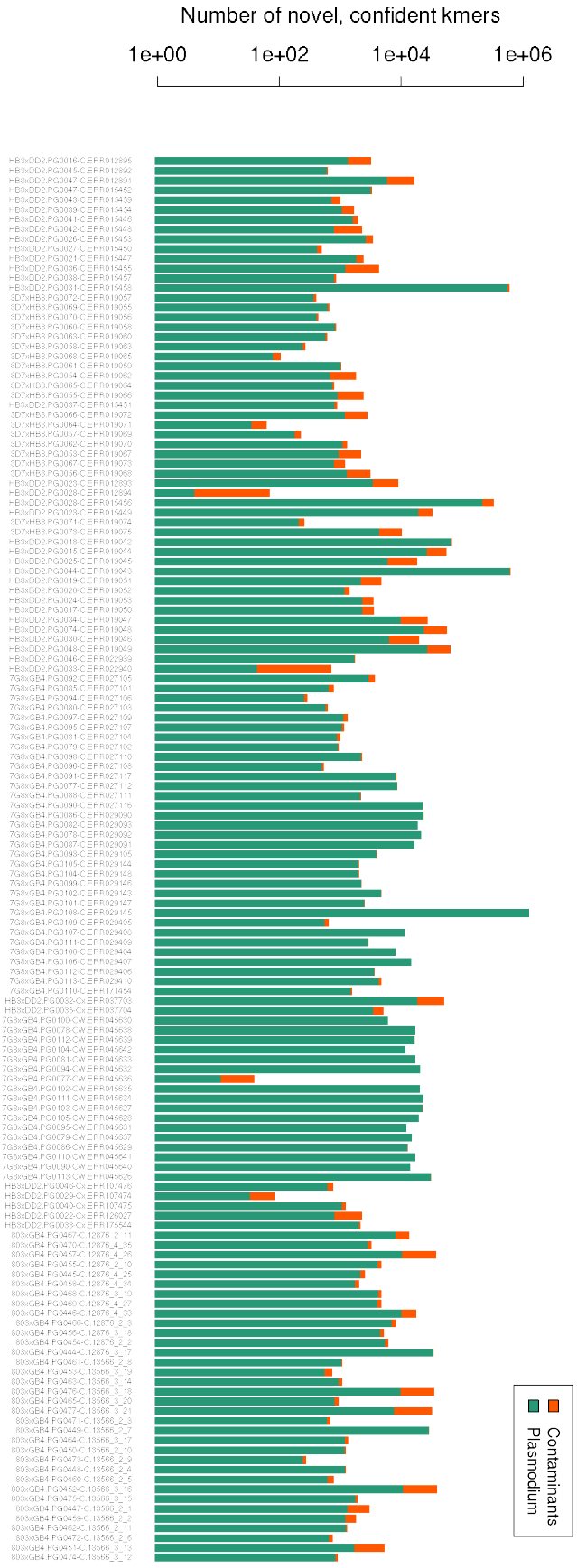

Figure 4.14: Removal of contaminating kmers; *P. falciparum* kmers are shown in green; the putative contaminants are shown in orange.

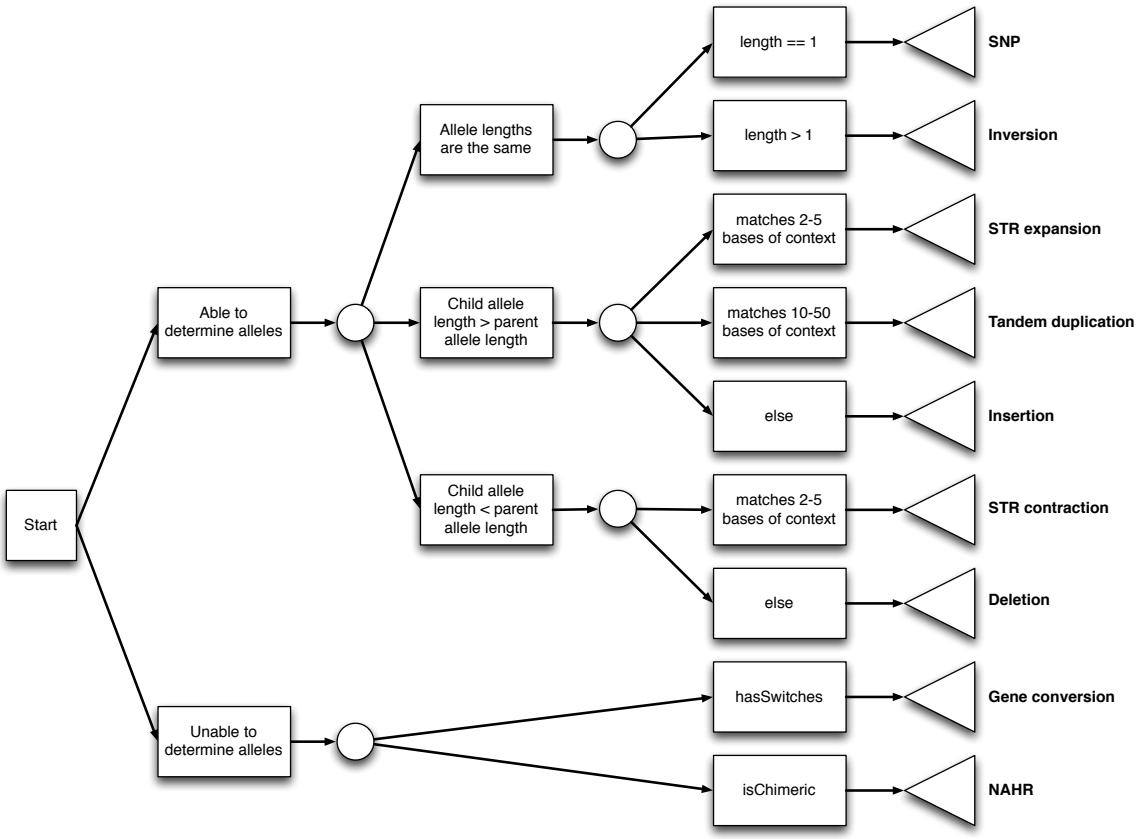
Start
Able to determine alleles
Unable to determine alleles
Allele lengths are the same
Child allele length > parent allele length
Child allele length < parent allele length
length == 1
length > 1
matches 2-5 bases of context
matches 10-50 bases of context
else
matches 2-5 bases of context
else
hasSwitches
isChimeric
SNP
Inversion
STR expansion
Tandem duplication
Insertion
STR contraction
Deletion
Gene conversion
NAHR

Figure 4.15

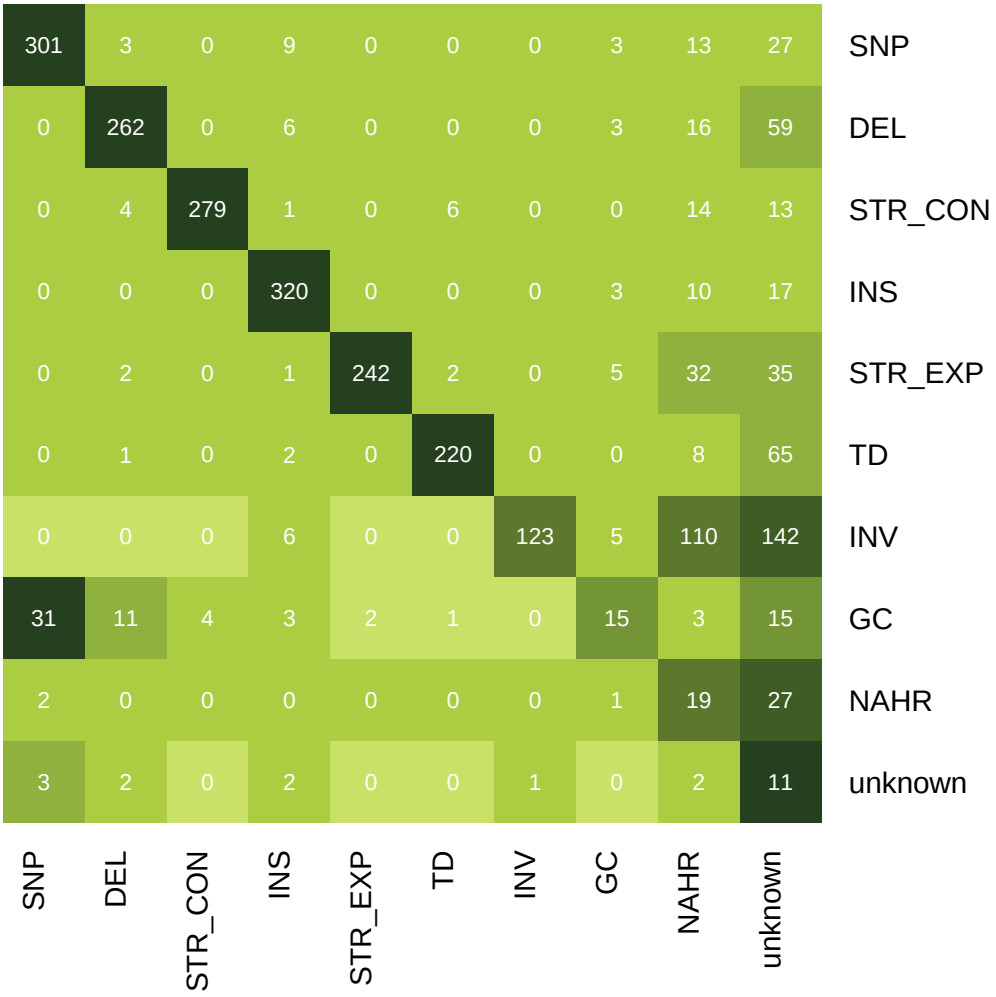

Figure 4.16: Confusion matrix for observed events (below) versus expected events (right), in simulated perfect data.

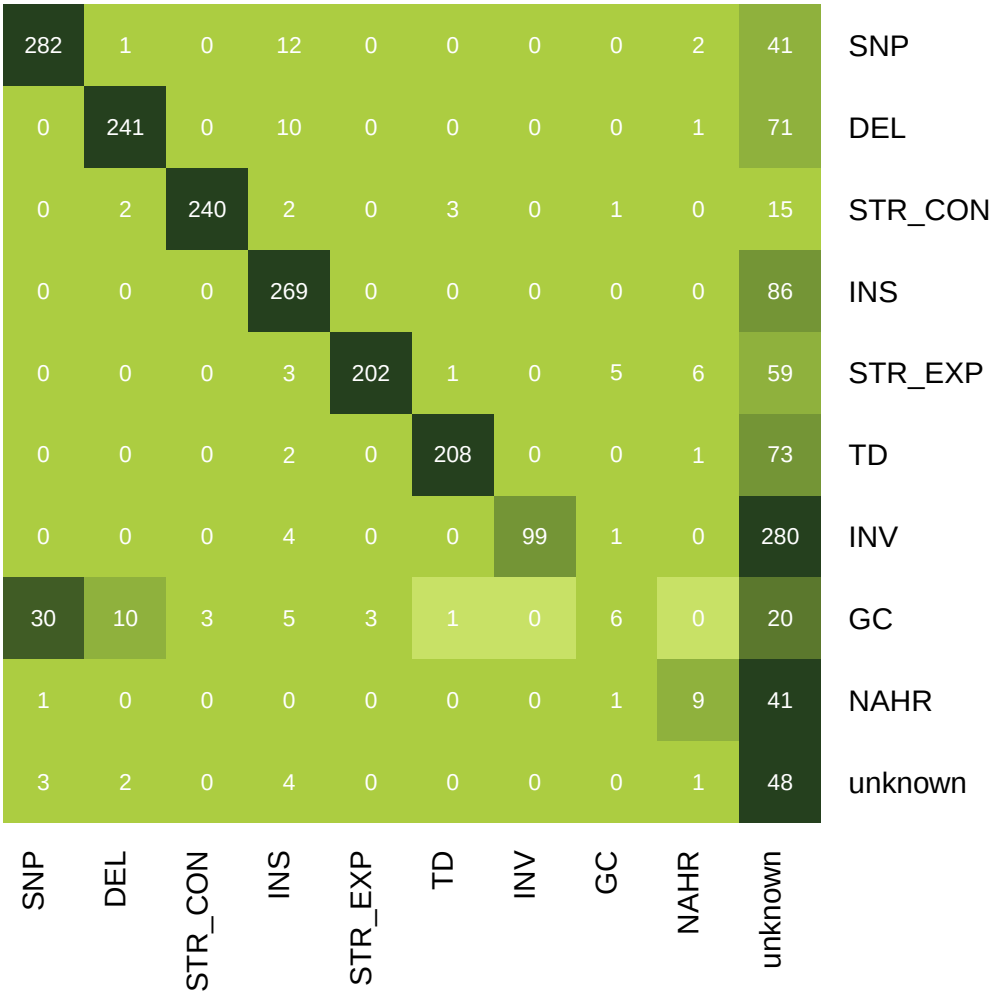

Figure 4.17: Confusion matrix for observed events (below) versus expected events (right), in simulated realistic data.

5 *Plasmodium falciparum*

In the previous chapter, we demonstrated our *de novo* mutation detection software on simulated crossings of the *falciparum* malaria parasites. We now apply our work to real data: over 100 samples taken from four separate crossings of six parasites.

No comprehensive catalog of *de novo* variation in these crosses currently exists. To date, the focus on the $3D7xHB3$, $HB3xDD2$, $7G8xGB4$ and $803xGB4$ datasets has largely been on discovering the genomic basis for phenotypic differences between the parents, and on characterizing novel antigenic forms in the children. However, the previous phenotypic studies have verified the presence of some large structural *de novo* variants - namely a handful of NAHR events involving antigenic genes. These known events serve as useful validation data for the most difficult form of variation for our software to detect. Furthermore, these previously observed events have occurred in low-complexity regions. Such regions may confound DNA repair machinery and provide a substrate for the generation of *de novo* variation. These regions are outside the reach of reference-based analyses, but may be accessible with our graph-based approach. Finally, the *P. falciparum* genome is small enough to be sequenced inexpensively on current third generation sequencing platforms, enabling high-quality reconstructions of the parental genomes, and in turn, facilitating DNM discovery. These factors make the *P. falciparum* datasets a compelling study target.

5.1 Data processing

5.1.1 Initial data

We obtained whole genome sequence data for parent and progeny clones of the $3D7xHB3$,[6] $HB3xDD2$,[8] $7G8xGB4$,[51] and $803xGB4$[1] crosses. All were sequenced on Illumina platforms over the past five years using a PCR-free library preparation protocol known to reduce coverage biases associated with AT-rich templates. Across all four crosses, we obtained 152 samples prior to any quality control checks.

[1] Rick Fairhurst and Michael Krause, personal communication

Table 5.1: Additional data availability for all *P. falciparum* cross parents

	3D7	HB3	DD2	7G8	GB4	803
Finished reference	x					
PacBio assembly	x	x	x	x	x	
Draft assembly		x	x	x		
Illumina data	x	x	x	x	x	x

5.1.2 Sample processing

5.1.2.1 Children

We used the available Illumina data to construct the de Bruijn graph structures for each child with McCortex, using a kmer size of 47 bp and discarding bases with a quality score less than Q5. The "dirty" graph (raw graph structure before any pruning is applied) was cleaned using McCortex's automatically chosen thresholds (falling back to trimming contiguous regions of the graph with coverage less than 2 in the event that automatic thresholds could not be calculated). As contigs were not required for our analyses, we opted to forego the paired-end read threading and contig emission steps.

5.1.2.2 Parents

In addition to the Illumina data for the parents, we often benefitted from the availability of supplementary draft assembly data from the Pf3k project. These draft assemblies were constructed using the HGAP 2.0 pipeline,[52] an assembler that follows the overlap-layout-consensus paradigm using exccedingly long reads from from PacBio RSII instruments (on average 10,000 kb in length, sometimes as long as 50,000 kb, two orders of magnitude longer than the reads used to assemble the finished 3D7 reference). This data helps in determining parental paths in the graph near variants without ambiguity. Table 5.1 shows all additional data used in constructing parental assemblies.

Parental graph construction was performed on each parental data source separately following the same workflow used for the children's graphs. The separate graphs were then combined into a single graph using McCortex's `join` command.

For most samples, the finished or draft PacBio assemblies vastly outperform any assembly that could be produced with the Illumina data, and are an excellent basis for localizing events and determining their proximity to genes. However, as there is no high-quality sequence of the 803 genome, we were forced to construct one ourselves using the available Illumina data. After producing the cleaned graph with the McCortex workflow, we applied the software's paired-end read threading and contig emission steps. The assembly statistics for all six genomes are presented in Table 5.2. The assembly for 803

Table 5.2: Statistics on all parental assemblies

	contigs	min length	max length	N50	total sequence	genes
3D7	16	5,967	3,291,936	1,687,656	23,332,831	5,777
DD2	16	6,094	3,257,617	1,661,885	22,682,339	8,284 (3D7, DD2)
7G8	17	6,094	3,311,228	1,560,458	22,832,195	5,530 (3D7)
GB4	26	7,376	3,360,747	1,565,171	23,525,386	5,576 (3D7)
HB3	28	6,094	3,378,065	1,593,993	22,812,563	7,467 (3D7, HB3)
803	148,826	47	17,610	1,042	59,118,463	4,663 (3D7)

is exceedingly poor compared to the other assemblies, as expected from short Illumina reads. That the total sequence length is more than 2.5 times larger than a typical *falciparum* parasite is almost certainly artifactual and will be discussed further below.

We transferred gene models onto the new genomes by examining existing finished and draft reference genomes and their annotation sets, selecting each annotated exon sequnce from its corresponding FASTA sequence file, and aligning it to the new genome using BWA. For 7G8, GB4, and 803, we transferred only the 3D7 annotations obtained from PlasmoDB release 26.[29] For DD2 and HB3, additional separate annotations exist from the Broad Institute. These undoubtedly contain better representations of genes divergent from their 3D7 counterparts (particularly antigens). However, owing to the poor DD2 and HB3 assemblies to which they are associated, the annotations are likely to be incomplete. We therefore chose to transfer both the 3D7 and DD2 (HB3) annotations onto the new DD2 (HB3) assemblies. This has resulted in a slight over-annotation of genes in these two genomes, as shown in Table 5.2. This happens when the gene models slightly differ between 3D7 and the target (e.g. exon end definitions differ by as much as a single nucleotide), but refer to the same gene. Rather than simply choosing one definition, we permit both to remain as the PlasmoDB annotations are continuously maintained and improved, while the Broad's annotations have not been updated since April 2014.

When producing visualizations with the Circos[53] genomic comparison tool, we require alignments between the contigs of a parental genome and the chromosomes of the reference. For 3D7, DD2, 7G8, GB4, and HB3, this is trivial as nearly the entirety of each chromosome has been successfully reconstructed. For those genomes, we simply lined each assembled contig with its 3D7 counterpart. In the case of 803, we aligned each contig to the 3D7 genome using BWA to derive the mapping.

Finally, we computed a number of sequence composition and complexity metrics in tiled 2,500 bp windows using the SeqComplex tool[2]. The full list of metrics computed is as follows:

[2]https://github.com/caballero/SeqComplex

1. gc: GC content
2. gcs: GC skew (defined as $(G - C)/(G + C)$)
3. at: AT content
4. ats: AT skew (defined as $(A - T)/(A + T)$)
5. cpg: CpG content
6. ce: Complexity by Shannon entropy[54]
7. cl: Complexity by linguistic values[55]
8. cwf: Complexity by Wootton and Federhen[56]
9. cz: Compression factor (the ratio of uncompressed to compressed sequence file size, using the `gzip` compression utility)

These metrics were computed for each parental genome except 803, whose contig lengths were too variable to consistently satisfy the 2,500 bp window requirement, making comparison with GB4 cumbersome.

5.1.3 Quality control

We examined assembly metrics on all of our samples in order to flag samples for downstream analysis rejection. We examined each sample for outlier behavior per cross in the following metrics:

1. number of unique kmers: the total number of unique kmers in the graph after the automatic cleaning step
2. contig N50: the weighted median length of the contigs (very short contigs may indicate high sequencing error rate)
3. total assembly length: the sum of all contigs produced (this should be reasonably close to the expected genome size)

The distributions for each of these metrics are shown in Figure 5.1. We rejected samples that were outliers in at least two metrics (shown in red).

One assumes that a newly assembled *falciparum* parasite should have a similar assembly length to the $3D7$ reference sequence, or at least the other assembled parasites in this dataset. Many of the $803xGB4$ samples appear to defy this expectation (including the 803

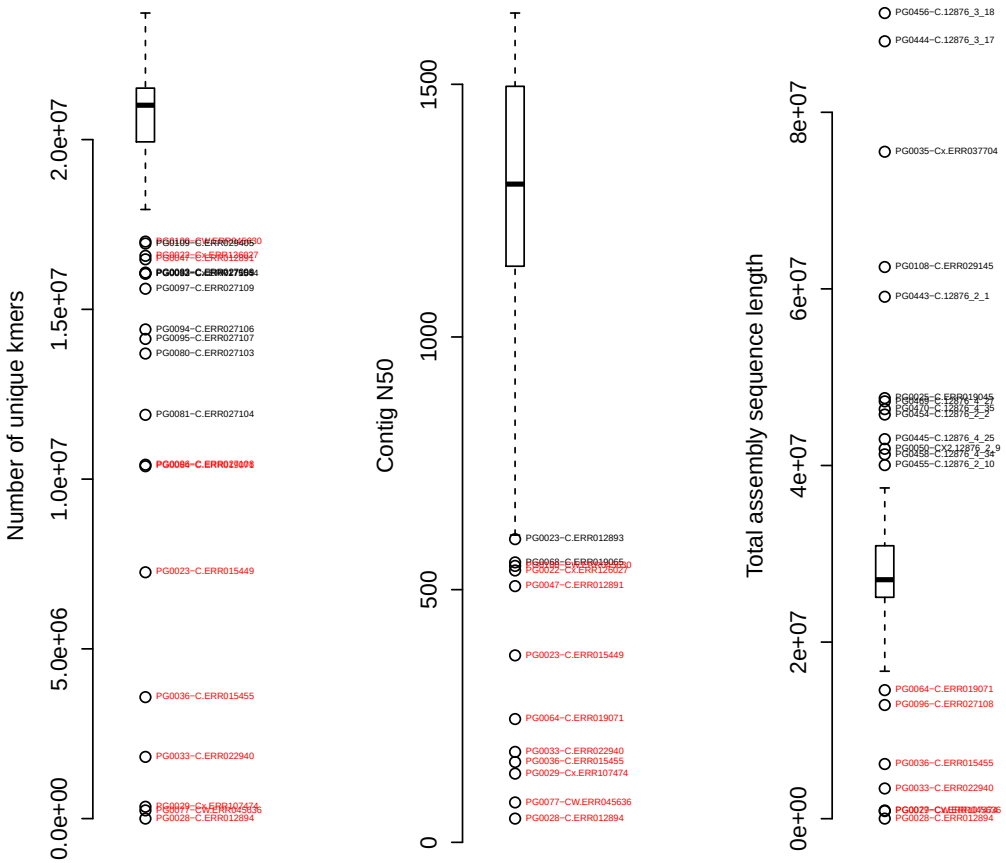

Figure 5.1: Boxplots of QC metrics

parental sample), exhibiting assembly lengths well above the 23 megabases we expected. Several samples have much longer assemblies: 40 megabases or more. This outcome is unchanged even when other assembly software (e.g. SGA) is applied. The source of this excess sequence is unclear. It is possibly due to intraspecies sample contamination. This would not be filtered out by our contamination checks, as those checks serve only to eliminate non-*falciparum* kmers that might masquerade as novel kmers. Despite this worry, we chose specifically not to exclude these samples from our analysis for two reasons: first, the issue affects a preponderance of 803xGB4 samples, including the parents; and second, our graph-based variant caller should hopefully be able to compensate for the issue.

Table 5.3: Summary of *P. falciparum* cross data

	3D7xHB3	HB3xDD2	7G8xGB4	803xGB4
Samples	22	42	52	36
Samples QC+	21	35	49	36
Read length	76	76	76	100
Fragment size	300 ± 29	253 ± 48	293 ± 21	222 ± 10
Coverage	99 ± 38	121 ± 91	110 ± 40	205 ± 106
Platform	Illumina GAII	Illumina GAII	Illumina GAII	Illumina HiSeq 2000
Sequencing Date	2010	2009-2012	2010-2011	2014

The final dataset after QC is shown in Table 5.3. Sequencing date and QC status are shown in Figure 5.2.

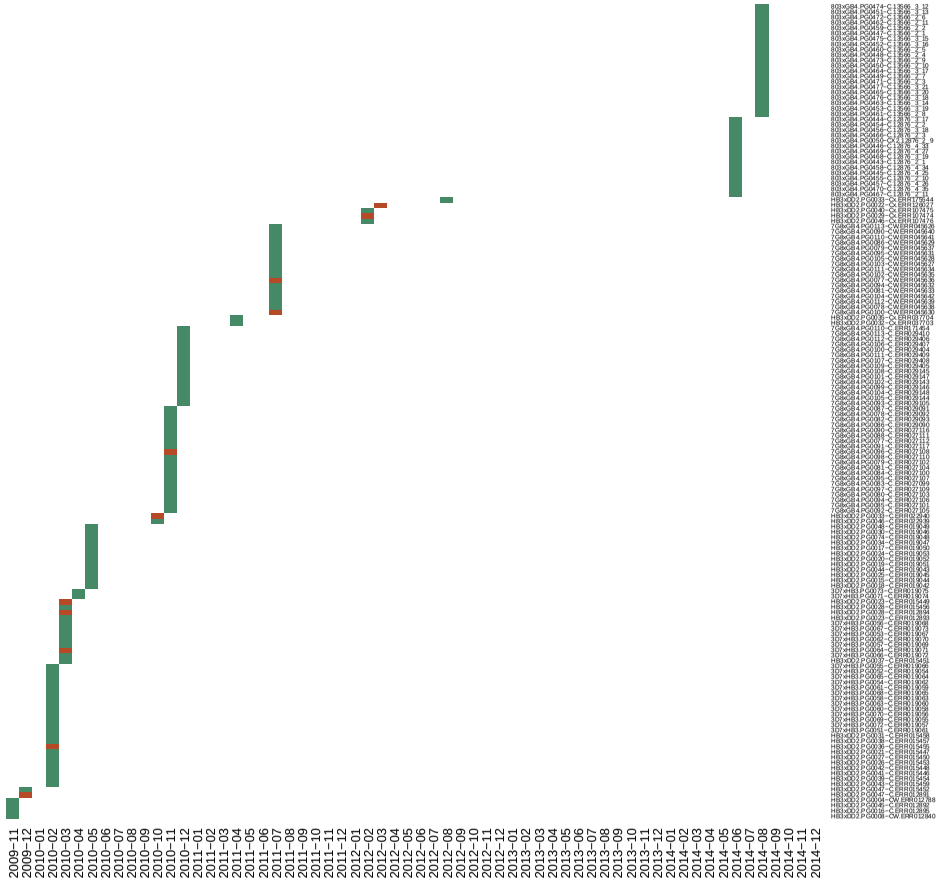

Figure 5.2: Samples and their sequencing date. QC failures are shown in red.

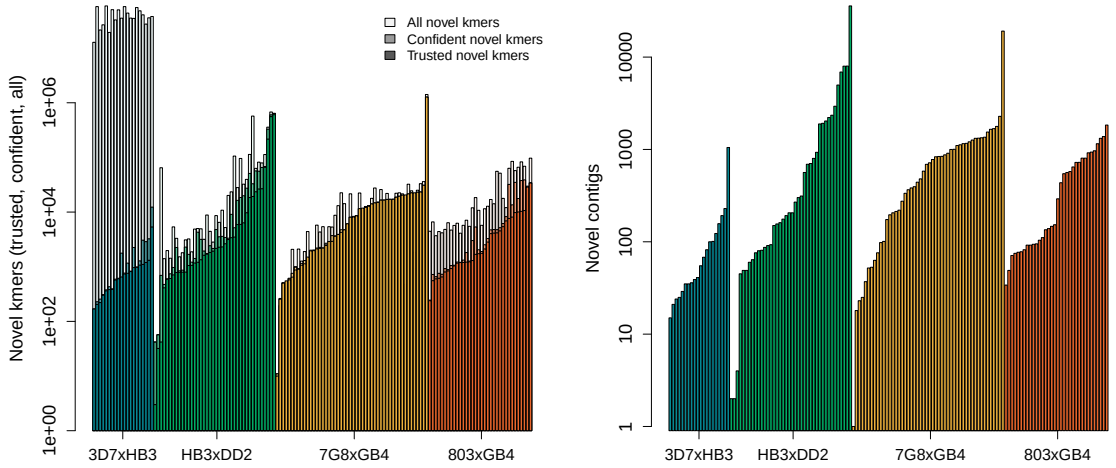

Figure 5.3: a. Number of novel kmers found in each sample, broken down into "trusted", "confident", and "all" categories. b. Number of novel contigs (contigs containing at least one trusted novel kmer) per sample.

5.1.4 Novel kmers

We identified novel kmers using the software we presented in Chapter 4, dividing the set into three subsets: "all" (no filtering applied), "confident" (kmer coverage thresholds automatically detected and applied), and "trusted" (potential contaminants removed). The total number of such kmers is shown in Figure 5.3a.

The 3D7xHB3 cross has far more novel kmers than the other samples before any coverage and contamination filters are applied. This may simply reflect the fact that the 3D7xHB3 samples were sequenced on early Illumina GAII sequencers and chemistry. With the exception of a handful of HB3xDD2 samples, they are the oldest samples in the dataset, and perhaps have a much higher error rate to show for it.

Furthermore, the 803xGB4 samples have consistent novel kmer behavior with the samples from other crosses, despite the assembly lengths being substantially longer than expectation.

After all filters are applied, the number of novel kmers per sample appears to have tremendous variance, typically between 100 and 1,000.

Novel contigs (contigs containing trusted novel kmers) can be used as a proxy for *de novo* mutations in the genome, as each contiguous stretch of novel kmers ideally represents the child's branch of a variant bubble. In practice, the proxy is imperfect as many contigs will be prematurely truncated due to absent coverage, repetitive regions, or se-

quencing error. Nevertheless, it is still a useful upper bound on the amount of variation we might expect to see in each parasite. Figure 5.3b shows the number of such novel contigs in each sample. The median number of novel contigs per sample is 224, far fewer in the 3D7xHB3 cross (48). The overall contig count distributions are quite consistent between crosses.

5.2 *De novo mutations in the P. falciparum crosses*

5.2.1 *De novo mutations in a single sample*

We first examined DNM calls in a single sample from the $3D7xHB3$ cross: PG0063-C. This sample is known to harbor an NAHR event between two *var* genes: *PF3D7_0100100* (situated in the 5′ telomere of chromosome 1), and *PF3D7_0223500* (the 3′ telomere of chromosome 2), which makes it a useful test sample for initial examination. All 27 called mutations are described in Table 5.4, additionally annotated with the locus, the haplotypic background of the variant, variant type, closest gene (and the associated product), and whether the variant falls within the MalariaGen variant calling exclusion mask. The variants can be seen in their genomic context in Figure 5.4.

Table 5.4: *De novo* variants in 3D7xHB3 progeny, PG0063-C

	locus	background	event	closest gene	product	within mask
1	1:27733	3D7	unknown	PF3D7_0100100	PfEMP1 (var)	yes
2	1:29780	3D7	MNP	PF3D7_0100100	PfEMP1 (var)	yes
3	1:30339;2:922666	3D7	NAHR	PF3D7_0100100;PF3D7_0223500*	PfEMP1 (var)	yes
4	1:31825;2:920323	3D7	unknown	PF3D7_0100100;PF3D7_0223500*	PfEMP1 (var)	yes
5	1:30503;1:613915	3D7	NAHR	PF3D7_0115700	PfEMP1 (var)	yes
6	2:227	3D7	NAHR	PF3D7_0200100	PfEMP1 (var)	yes
7	2:394194	3D7	unknown	PF3D7_0209600*	transporter	no
8	2:919803	3D7	SNP	PF3D7_0223500*	PfEMP1 (var)	yes
9	3:471	HB3	unknown	PF3D7_0300100	PfEMP1 (var)	yes
10	3:1064983	3D7	unknown	PF3D7_0324900	PfEMP1 (var)	yes
11	6:1338957	HB3	GC	PF3D7_0632100*	RIF	yes
12	6:1338975	HB3	unknown	PF3D7_0632100*	RIF	yes
13	7:658	HB3	MNP	PF3D7_0700100	PfEMP1 (var)	yes
14	7:1428132	3D7	INS	PF3D7_0733000	PfEMP1 (var)	yes
15	10:1663367	3D7	MNP	PF3D7_1041300	PfEMP1 (var)	yes
16	12:532	3D7	unknown	PF3D7_1200100	PfEMP1 (var)	yes
17	12:603510;12:603561	3D7	unknown	PF3D7_1214100*	PIGO	no
18	13:953155	HB3	unknown	PF3D7_1322500*	DHHC5	no
19	13:15776184	HB3	unknown	PF3D7_1339200	tRNA proline	no
20	13:2871396	3D7	STR_EXP	PF3D7_1373100*	RIF	yes
21	14:1040207	3D7	unknown	PF3D7_1426700	PEPC	no
22	14:3016814	3D7	SNP	PF3D7_1474000*	probable protein	no
23	14:3065820	3D7	unknown	PF3D7_1474700*	protein kinase	no
24 (a)	1:27241;14:23321	3D7;HB3	NAHR	PF3D7_0100100;PF3D7_1400700	Stevor;PfEMP1 (var)	yes
24 (b)	14:23321;1:617342	HB3;3D7	NAHR	PF3D7_1400700;PF3D7_0115700	PfEMP1 (var)	yes
24 (c)	1:617342;13:2894565	3D7	NAHR	PF3D7_0115700;PF3D7_1373500	PfEMP1 (var)	yes
25	NA	3D7	unknown	unknown	unknown	NA
26	NA	3D7	unknown	unknown	unknown	NA
27	NA	3D7	unknown	unknown	unknown	NA

There are several noteworthy features of Table 5.4 and Figure 5.4. First, the call rate is reasonably low; less than 30 events in this sample, consistent with the expectation that *de novo* mutations should be rare. We discover a variety of event types, including SNPs (depicted in the plot with large circles), indels (triangles), multi-nucleotide polymorphisms (squares), and NAHR events (diamonds). Many events could not be typed (small circles).

Second, nearly all of the events can be localized within the parental genomes, even if the precise event type could not always be determined. Here, we benefit from aligning sequences that flank the region of novelty, rather than aligning 76 bp reads. The flanking sequences can often be longer than a read length, which provides the alignment software more context with which to determine an appropriate home for the variant. Further to this point, nearly all of the variants appear on a haplotypic background consistent with the haplotype assignments from the reference-based analysis (shown in the outer ideogram). This is of course expected, as when the graph traversal lacks sufficent context to determine the parentage of a stretch of sequence, we simply determine the appropriate parent using the flank alignments and the reference-based parentage determinations. There are occasional violations of the expected parentage, which may indicate a missed recombination event (perhaps a gene conversion in the case of the untyped variant at the 3′ end of chromosome 3).

Third, we are able to identify interchromosomal exchanges, including the known NAHR event between PF3D7_0100100 on the 5′ end of chromosome 1 and PF3D7_0223500 on the 3′ end of chromosome 2.[57] Curiously, there is another apparent interchromosomal exchange involving antigenic genes on chromosomes 1, 13, and 14. While Sander *et al.* did describe another NAHR event involving PF3D7_0115700 and PF3D7_0200100, that event was verified to have occurred in PG0062-C, not PG0063-C. Both PF3D7_0115700 and PF3D7_0200100 do seem to have incurred DNMs. However, our calls suggest an exchange between PF3D7_0115700, PF3D7_1373500 (both *var* genes), and perhaps even PF3D7_1400700 (a member of the *stevor* antigenic gene family). Such a complex recombination seems implausible, and is perhaps artifactual. This unexpected behavior might be due to intraspecies contamination during library preparation of the sequenced samples. However, if significant sample mixing had occurred, we would expect to see unusual allele balances at variant sites in the reference-based analysis (since in a pure sample, the allele balance should ideally be 100% alternate allele, 0% reference allele). Visual inspection of a number of variant sites in IGV does not reveal unusual allele balances. We note that the alignment of this variant's flanking sequence to chromosomes 13 and 14 are only supported by 2 to 4 kmers (48 to 50 bp, respectively). It is possible that a repetitive region present on all three chromosomes happens to be collapsed on chromosome 1, but

represented more completely on chromosomes 13 and 14. Kmers that appear unique to those chromosomes might actually be present in chromosome 1, but are not present in the finished sequence by chance.

Fourth, we are able to detect some intrachromosomal events. Chromosome 6 appears to contain a single gene conversion event within the PF3D7_0632100 gene, a member of the large *rifin* antigenic gene family. Interestingly, chromosome 2 is home to a variant whose type was unable to be determined. However, it is apparently on the 3D7 haplotypic background, despite surrounding variants suggesting that it should be on the HB3 background. This could be another gene conversion event that was incompletely assembled.

Fifth, we are able to detect many mutations that occur in masked regions of the reference genome. MalariaGen delibrately excluded a number of regions from processing. This included repetitive regions (often telomeric, centromeric, or pericentromeric regions) as short reads could often not be aligned in long repetitive regions with confidence. It also included hypervariable regions (typically subtelomeric) as population diversity was too great to yield confident results in the reference-based analysis. As we are comparing each sample to a parental graph rather than a reference sequence that is an undetermined number of generations removed, our graphical approach can reconstruct and localize these events. For example, the MNP on the 3' end of chromosome 10 falls within a subtelomeric repetitive region.

Sixth, our calls in this sample appear overwhelmingly concentrated in or near antigenic genes (19/27), most often *var* genes. This is likely somewhat over-counted owing to incomplete reconstructions of the same variant appearing multiple times. Yet, a more pessimistic accounting wherein we only count each affected locus once still suggests that 14/23 events are in or near antigenic genes. Such a skew is unusual, especially given the fact that our algorithm is hypothesis-free and is not biased towards processing any particular region of the genome.

Subtelomeric regions (and the antigenic genes contained within) are known to be high in repetitive sequence. To visualize the potential relationship between sequence content and variant location, we examined a number of different sequence properties. Shown in Figure 5.4 above each parental assembly track is one of these metrics: the sequence compression ratio. Data compression algorithms look for a smaller representation of a given string of data. For example, a simple run-length encoding (wherein we count the number of identical and adjacent characters) of the sequence `AAAAGAGACCCC` might yield

the encoding,

$$rle(AAAAGAGACCCC) = A(4)G(1)A(1)G(1)A(1)C(4), \tag{5.1}$$

where the number indicates the the preceeding character should be repeated in order to reconstruct the original sequence. In contrast, the sequence `AGTCGTTCATGT` would yield,

$$rle(AGTCGTTCATGT) = A(1)G(1)T(1)C(1)G(1)T(2)C(1)A(1)T(1)G(1)T(1). \tag{5.2}$$

Clearly the first sequence compresses to something much smaller than the second owing to the repetitiveness of the sequence. Such compression or entropy measures on sequence provide an excellent metric for sequence complexity. Many of our DNM calls appear to follow closely with spikes in the local sequence compressibility measure. Quite often these spikes correspond with being in a masked repetitive region, but there are notable additions. For example, two SNPs on chromosome 14, occuring in PF3D7_1474000 (unknown function) and PF3D7_1474700 (a protein kinase, thought to be a viable drug target[58]) appear near such a local increase in sequence compressibility. We shall examine this point in greater detail when we discuss the calls across the whole dataset.

5.2.2 *De novo mutations in all 3D7xHB3 progeny*

5.2.2.1 *Allelic events*

Counts per sample are shown in Figure **??**, stratified by type (left) and subtype (right). Across the entire 20-sample 3D7xHB3 dataset, allelic variant counts per sample are modest - around two SNPs and one to two insertions, deletions, and MNPs per sample. Many of these events are still found in subtelomeric low complexity regions, as evidenced by the sample mosaic in Figure 5.6.

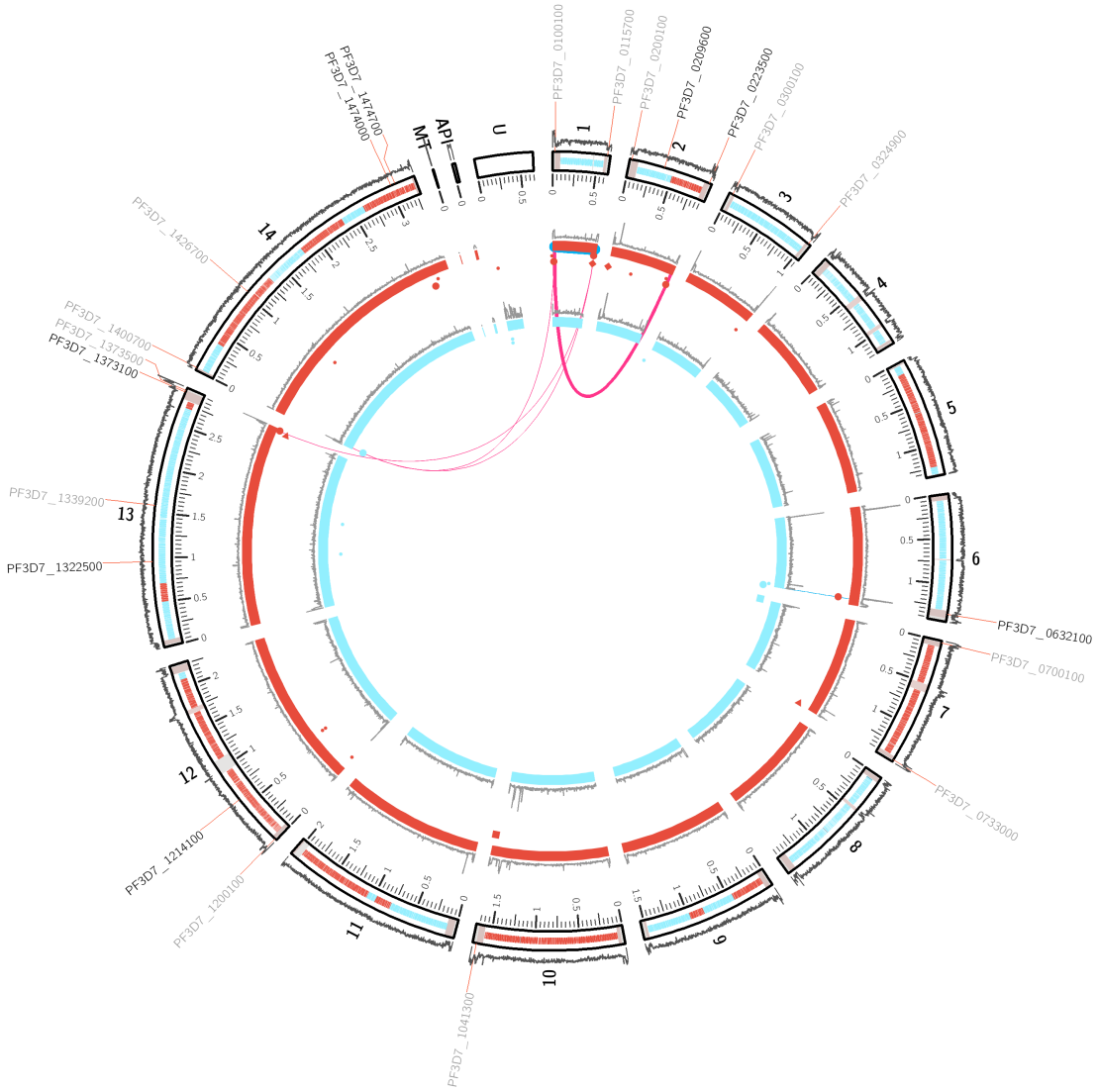

Figure 5.4: Circos visualization of all *de novo* mutations in PG0063-C, positioned on the reference sequence (outer ring), aligned maternal assembly (middle), and aligned paternal assembly (inner). Unplaced parental contigs are concatenated and placed in the "U" pseudochromosome. Each parental ring is annotated with a sequence compressibility score for every 2,500 bp shown above their ideograms, while the reference ring is annotated with mean read coverage per 2,500 bp. Within the reference ideogram, all reference-based variant calls made in this sample from the MalariaGen project are shown, color-coded to reflect their parentage. Regions that were masked out of MalariaGen's variant calling process are shown as grey bars. Variants are shown as glyphs below the parental ideograms, shape-coded for type (small circle: unknown, large circle: SNP, triangle: indel, square: MNP, diamond: NAHR event). The color and positioning of the glyph reflects the haplotypic background upon which the event occurred. Interchromosomal structural variation and gene-conversion events are additionally denoted as arcs linking the relevant parts of the genome. The closest gene to the event is reported in black if the mutation falls within the gene and as grey if it falls outside the gene.

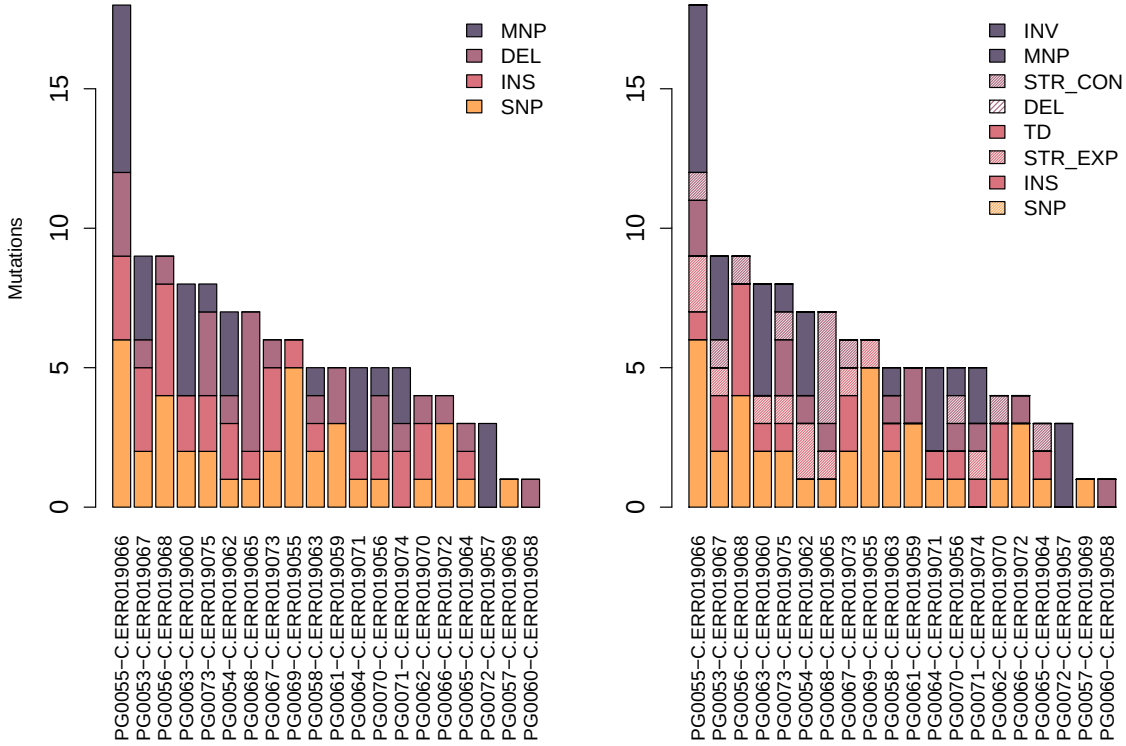

Figure 5.5: *De novo* mutations in each of the 20 progeny from the 3D7xHB3 cross.

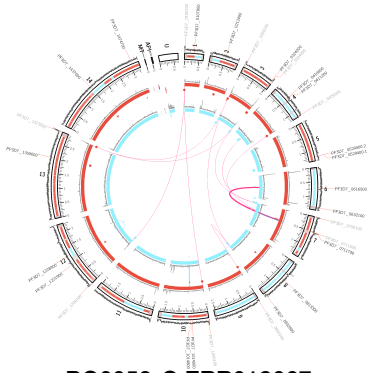

PG0053-C.ERR019067

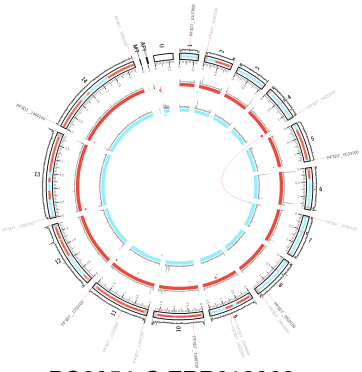

PG0054-C.ERR019062

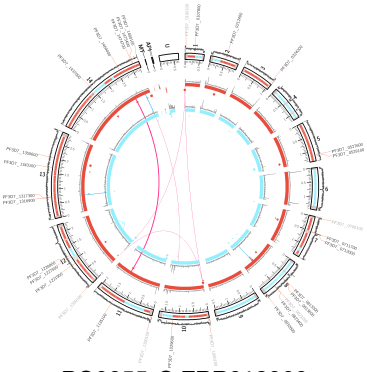

PG0055-C.ERR019066

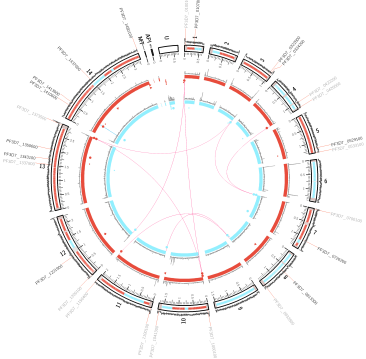

PG0056-C.ERR019068

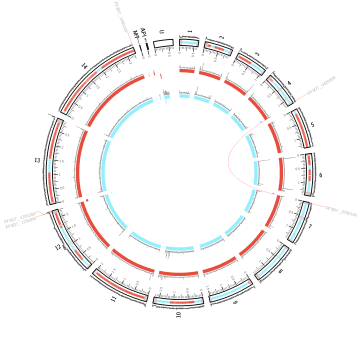

PG0057-C.ERR019069

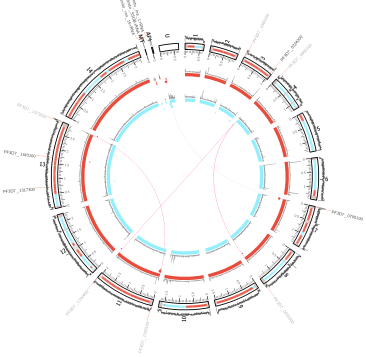

PG0058-C.ERR019063

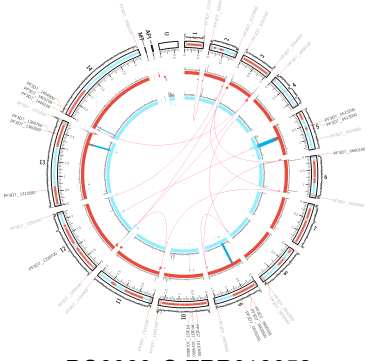

PG0060-C.ERR019058

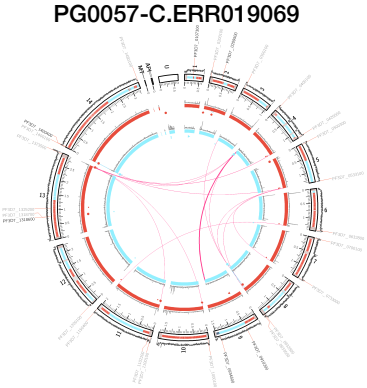

PG0061-C.ERR019059

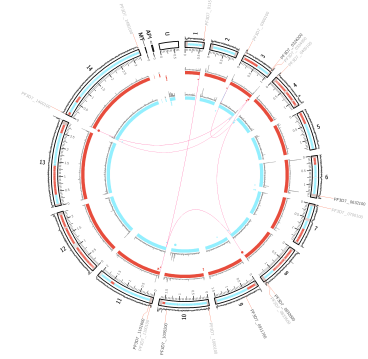

PG0062-C.ERR019070

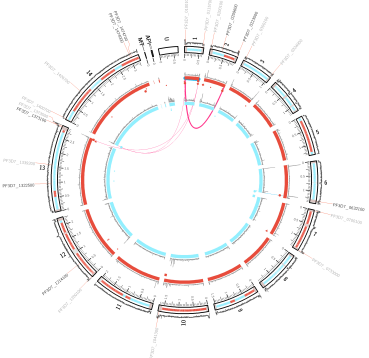

PG0063-C.ERR019060

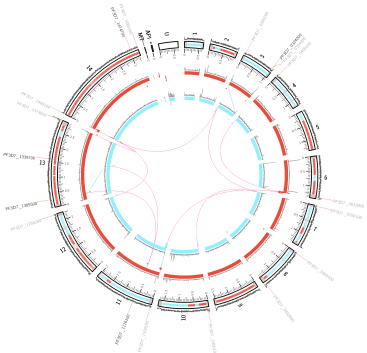

PG0064-C.ERR019071

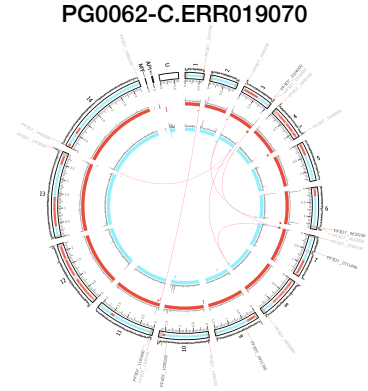

PG0065-C.ERR019064

Figure 5.6: *De novo* mutations in each of the 20 progeny from the 3D7xHB3 cross. Left: mutations stratified by type. Right: mutations stratified by subtype.

sample	type	length	locus	gene	description
PG0063-C.ERR019060	MNP	0	Pf3D7_01_v3:27733-27902	PF3D7_0100100	PfEMP1 (VAR)
PG0063-C.ERR019060	MNP	9	Pf3D7_01_v3:29780-30133	PF3D7_0100100*	PfEMP1 (VAR)
PG0061-C.ERR019059	DEL	30	PfHB3_01:299430-299547	PF3D7_0108700*	secreted ookinete protein, putative (PSOP24)
PG0055-C.ERR019066	SNP	0	Pf3D7_02_v3:495067-495161	PF3D7_0212400	conserved membrane protein, unknown function
PG0053-C.ERR019067	SNP	0	Pf3D7_02_v3:495067-495161	PF3D7_0212400	conserved membrane protein, unknown function
PG0070-C.ERR019056	SNP	0	PfHB3_02:698465-698559	PF3D7_0217500*	calcium-dependent protein kinase 1 (CDPK1)
PG0063-C.ERR019060	SNP	0	Pf3D7_02_v3:919803-920297	PF3D7_0223500*	PfEMP1 (VAR)
PG0062-C.ERR019070	INS	100	PfHB3_04:1-48	PF3D7_0300600	exported protein, unknown function, fragment
PG0062-C.ERR019070	INS	100	Pf3D7_03_v3:1063591-1063645	PF3D7_0324900	PfEMP1 (VAR)
PG0053-C.ERR019067	MNP	2	Pf3D7_03_v3:1066484-1066640	PF3D7_0324900	PfEMP1 (VAR)
PG0061-C.ERR019059	SNP	0	Pf3D7_05_v3:31612-31706	PF3D7_0500400	rifin (RIF)
PG0066-C.ERR019072	DEL	32	Pf3D7_05_v3:208520-208614	PF3D7_0505000	conserved membrane protein, unknown function
PG0055-C.ERR019066	SNP	0	PfHB3_05:1147154-1147246	PF3D7_0527300	methionine aminopeptidase 1a, putative (METAP1a)
PG0053-C.ERR019067	MNP	10	PfHB3_05:1203344-1203449	PF3D7_0529100	conserved protein, unknown function
PG0071-C.ERR019074	DEL	102	Pf3D7_06_v3:57319-57486	PF3D7_0601400	PfEMP1 (VAR) pseudogene
PG0070-C.ERR019056	STR_CON	4	Pf3D7_06_v3:253909-253981	PF3D7_0606000	conserved protein, unknown function
PG0064-C.ERR019071	MNP	54	Pf3D7_06_v3:1416554-1416719	PF3D7_0632800	PfEMP1 (VAR)
PG0071-C.ERR019074	STR_EXP	2	Pf3D7_06_v3:1377300-1377366	PF3D7_0632800*	PfEMP1 (VAR)
PG0056-C.ERR019068	SNP	0	PfHB3_07:1102288-1102382	PF3D7_0727700*	conserved protein, unknown function
PG0072-C.ERR019057	MNP	26	Pf3D7_07_v3:1428612-1428810	PF3D7_0733000	PfEMP1 (VAR)
PG0063-C.ERR019060	INS	1	Pf3D7_07_v3:1428132-1428267	PF3D7_0733000	PfEMP1 (VAR)
PG0068-C.ERR019065	STR_CON	8	PfHB3_08:79631-79699	PF3D7_0801500	nucleolar protein 10, putative (NOL10)
PG0053-C.ERR019067	MNP	34	PfHB3_04:478252-478977	PF3D7_0809000	RNA of unknown function RUF6-10
PG0067-C.ERR019073	STR_CON	8	Pf3D7_08_v3:656614-656684	PF3D7_0813300	conserved protein, unknown function
PG0055-C.ERR019066	STR_CON	8	Pf3D7_08_v3:656614-656684	PF3D7_0813300	conserved protein, unknown function
PG0053-C.ERR019067	STR_CON	8	Pf3D7_08_v3:656614-656684	PF3D7_0813300	conserved protein, unknown function
PG0056-C.ERR019068	STR_CON	8	Pf3D7_08_v3:656614-656684	PF3D7_0813300	conserved protein, unknown function
PG0055-C.ERR019066	DEL	947	Pf3D7_08_v3:1024822-1025845	PF3D7_0823200	RNA binding protein, putative
PG0068-C.ERR019065	STR_EXP	5	PfHB3_09:217009-217114	PF3D7_0905100	nucleoporin NUP100/NSP100, putative (NUP100)
PG0061-C.ERR019059	DEL	15	Pf3D7_09_v3:472149-472252	PF3D7_0910300	conserved protein, unknown function
PG0073-C.ERR019075	STR_CON	8	Pf3D7_09_v3:1223097-1223182	PF3D7_0930700*	conserved protein, unknown function

PG0073-C.ERR019075	MNP	110	Pf3D7_10_v3:145-377	PF3D7_1000100	PfEMP1 (VAR)
PG0069-C.ERR019055	STR_EXP	2	PfHB3_10:581292-581364	PF3D7_1015700.1	tubulin binding cofactor c, putative
PG0066-C.ERR019072	SNP	0	Pf3D7_10_v3:1286013-1286107	PF3D7_1031900*	conserved protein, unknown function
PG0068-C.ERR019065	SNP	0	PfHB3_10:1263212-1263306	PF3D7_1032700	conserved protein, unknown function
PG0062-C.ERR019070	SNP	0	PfHB3_10:1396068-1396162	PF3D7_1036500	probable protein, unknown function
PG0065-C.ERR019064	SNP	0	PfHB3_10:1396068-1396162	PF3D7_1036500	probable protein, unknown function
PG0063-C.ERR019060	MNP	147	Pf3D7_10_v3:1663367-1663662	PF3D7_1041300	PfEMP1 (VAR)
PG0056-C.ERR019068	INS	89	Pf3D7_10_v3:1687367-1687443	PF3D7_1041300	PfEMP1 (VAR)
PG0070-C.ERR019056	MNP	6	Pf3D7_11_v3:448-545	PF3D7_1100100	PfEMP1 (VAR)
PG0058-C.ERR019063	MNP	87	Pf3D7_11_v3:26051-26674	PF3D7_1100100*	PfEMP1 (VAR)
PG0071-C.ERR019074	INS	1	Pf3D7_11_v3:66678-66762	PF3D7_1101100*	rifin (RIF)
PG0062-C.ERR019070	STR_CON	4	Pf3D7_11_v3:82697-82754	PF3D7_1101600*	exported protein (hyp4), unknown function
PG0065-C.ERR019064	STR_CON	4	Pf3D7_11_v3:82697-82754	PF3D7_1101600*	exported protein (hyp4), unknown function
PG0073-C.ERR019075	SNP	0	Pf3D7_11_v3:1019513-1019607	PF3D7_1126100*	ThiF family protein, putative
PG0069-C.ERR019055	SNP	0	Pf3D7_11_v3:1019513-1019607	PF3D7_1126100*	ThiF family protein, putative
PG0073-C.ERR019075	STR_EXP	5	PfHB3_11:1662431-1662485	PF3D7_1143700	conserved protein, unknown function
PG0054-C.ERR019062	STR_EXP	4	Pf3D7_11_v3:2016514-2016581	PF3D7_1150100	rifin, pseudogene (RIF)
PG0072-C.ERR019057	MNP	75	PfHB3_12:768277-768511	PF3D7_1219400	PfEMP1 (VAR) pseudogene
PG0067-C.ERR019073	STR_EXP	2	Pf3D7_12_v3:875371-875426	PF3D7_1222000	conserved protein, unknown function
PG0055-C.ERR019066	STR_EXP	2	Pf3D7_12_v3:875371-875426	PF3D7_1222000	conserved protein, unknown function
PG0053-C.ERR019067	STR_EXP	2	Pf3D7_12_v3:875371-875426	PF3D7_1222000	conserved protein, unknown function
PG0057-C.ERR019069	SNP	0	Pf3D7_12_v3:2264188-2264282	PF3D7_1255200	PfEMP1 (VAR)
PG0054-C.ERR019062	DEL	87	Pf3D7_13_v3:412-600	PF3D7_1300100	PfEMP1 (VAR)
PG0061-C.ERR019059	SNP	0	Pf3D7_13_v3:773695-773789	PF3D7_1318800	secretory complex protein 63 (SEC63)
PG0070-C.ERR019056	DEL	12	Pf3D7_13_v3:843376-843468	PF3D7_1320500	SNARE protein, putative (SNAP23)
PG0067-C.ERR019073	SNP	0	Pf3D7_13_v3:2021904-2021998	PF3D7_1350600*	conserved protein, unknown function
PG0055-C.ERR019066	SNP	0	Pf3D7_13_v3:2021904-2021998	PF3D7_1350600*	conserved protein, unknown function
PG0053-C.ERR019067	SNP	0	Pf3D7_13_v3:2021904-2021998	PF3D7_1350600*	conserved protein, unknown function
PG0056-C.ERR019068	SNP	0	Pf3D7_13_v3:2021904-2021998	PF3D7_1350600*	conserved protein, unknown function
PG0063-C.ERR019060	STR_EXP	2	Pf3D7_13_v3:2871396-2871456	PF3D7_1373100	rifin (RIF)
PG0060-C.ERR019058	DEL	80	Pf3D7_13_v3:2922645-2922816	PF3D7_1373500	PfEMP1 (VAR)

PG0064-C.ERR019071	MNP	27	Pf3D7_14_v3:689-842	PF3D7_1400100	PfEMP1 (VAR) pseudogene
PG0071-C.ERR019074	MNP	3	Pf3D7_14_v3:40820-40922	PF3D7_1401100	DnaJ protein, putative
PG0068-C.ERR019065	STR_CON	2	Pf3D7_14_v3:135608-135681	PF3D7_1403800	nuclear formin-like protein (MISFIT)
PG0067-C.ERR019073	INS	15	Pf3D7_14_v3:1503807-1503892	PF3D7_1437000*	N-acetyltransferase, putative
PG0055-C.ERR019066	INS	15	Pf3D7_14_v3:1503807-1503892	PF3D7_1437000*	N-acetyltransferase, putative
PG0053-C.ERR019067	INS	15	Pf3D7_14_v3:1503807-1503892	PF3D7_1437000*	N-acetyltransferase, putative
PG0056-C.ERR019068	INS	15	Pf3D7_14_v3:1503807-1503892	PF3D7_1437000*	N-acetyltransferase, putative
PG0068-C.ERR019065	STR_CON	2	Pf3D7_14_v3:2024972-2025044	PF3D7_1449400	DNA replication related protein, putative
PG0070-C.ERR019056	INS	42	Pf3D7_14_v3:2021201-2021292	PF3D7_1449400*	DNA replication related protein, putative
PG0068-C.ERR019065	STR_CON	2	Pf3D7_14_v3:2212698-2212765	PF3D7_1453900	conserved protein, unknown function
PG0063-C.ERR019060	SNP	0	Pf3D7_14_v3:3016814-3016908	PF3D7_1474000*	probable protein, unknown function
PG0069-C.ERR019055	SNP	0	PfHB3_06:63123-63217	PFHG_01193	conserved hypothetical protein
PG0063-C.ERR019060	MNP	64	PfHB3_07:658-874	PFHG_03839	PfEMP1 (VAR)
PG0072-C.ERR019057	MNP	0	PfHB3_14:25601-25706	PFHG_04749*	conserved hypothetical protein
PG0073-C.ERR019075	DEL	327	PfHB3_00_20:40523-40933	PFHG_04943	predicted protein
PG0056-C.ERR019068	SNP	0	PfHB3_00_20:47284-47421	PFHG_04943	predicted protein
PG0064-C.ERR019071	MNP	20	PfHB3_11:361-483	PFHG_05272	conserved hypothetical protein
PG0068-C.ERR019065	DEL	3	PfHB3_00_1:45645-45739	PFHG_05612	predicted protein

Table 5.5: All allelic variants in the 3D7xHB3 cross that could be within the parental localized. Genes with an asterisk indicate variants that fall within the coding sequence.

The combined set of DNMs from the 3D7xHB3 dataset are displayed in Figure 5.6. Of the 119 allelic events found, 33 (mostly SNPs) could not be localized to some region of the genome (most likely, sufficient contextual sequence flanking the variant could not be assembled to enable the placement). The rest are shown in Table 5.5. This table indicates a number of interesting properties of our DNMs, including allele length (longest is a 947 bp deletion), affected gene (variants falling within the coding sequence are denoted with an asterisk), and annotated function of the gene. Entries are sorted by gene to highlight recurrent mutations (of which there are quite a few).

5.2.2.2 Non-allelic events

Special effort was made to reduce redundant calls of non-allelic events (as we've seen earlier, non-allelic events are occassionally too complex to reconstruct fully, yielding partial reconstructions instead that all map to roughly the same place in the genome). To do this, we considered NAHR or GC events within close proximity (within or close to the same gene) to be the same event. 30 putative events were found, listed below in Table 5.6.

sample	id	locus	closestGene	geneDescription
PG0073-C.ERR019075	1	11:190627	PF3D7_1104300	conserved Plasmodium protein
PG0073-C.ERR019075	2	5:584932	PF3D7_0513800	Rab GTPase 1a (RAB1a)
PG0073-C.ERR019075	3	7:261494	PFHG_05426*	hypothetical protein
PG0072-C.ERR019057	4(a)	12:2231574	PFHG_05455	conserved hypothetical protein
PG0072-C.ERR019057	4(b)	14:25661	PFHG_04749*	conserved hypothetical protein
PG0070-C.ERR019056	5(a)	10:10523658	PF3D7_1025100	glucosamine-fructose-6-phosphate aminotransferase, putative
PG0070-C.ERR019056	5(b)	5:208675	PF3D7_0505000	conserved Plasmodium membrane protein
PG0070-C.ERR019056	6(a)	1:249166	PF3D7_0105800*	conserved Plasmodium protein
PG0070-C.ERR019056	6(b)	12:1952170	PF3D7_1247300*	conserved protein
PG0070-C.ERR019056	7	13:700741	PF3D7_1316900	conserved Plasmodium protein
PG0070-C.ERR019056	8(a)	12:2027066	PF3D7_1249700	conserved Plasmodium protein
PG0070-C.ERR019056	8(b)	12:2032473	PFHG_03634	conserved hypothetical protein
PG0070-C.ERR019056	8(c)	12:2032473	PFHG_03634	conserved hypothetical protein
PG0070-C.ERR019056	8(d)	12:2027420	PF3D7_1249800	conserved Plasmodium protein
PG0070-C.ERR019056	8(e)	12:2027420	PF3D7_1249800	conserved Plasmodium protein
PG0070-C.ERR019056	8(f)	12:2027476	PF3D7_1249800	conserved Plasmodium protein
PG0070-C.ERR019056	8(g)	12:2027476	PF3D7_1249800	conserved Plasmodium protein
PG0070-C.ERR019056	8(h)	12:2032587	PFHG_03634	conserved hypothetical protein
PG0070-C.ERR019056	8(i)	12:2032587	PFHG_03634	conserved hypothetical protein
PG0070-C.ERR019056	8(j)	12:2027587	PF3D7_1249800	conserved Plasmodium protein
PG0070-C.ERR019056	8(k)	12:2027587	PF3D7_1249800	conserved Plasmodium protein
PG0070-C.ERR019056	8(l)	12:2032698	PFHG_03634	conserved hypothetical protein
PG0060-C.ERR019058	9(a)	9:373272	PF3D7_0908500*	conserved Plasmodium protein
PG0060-C.ERR019058	9(b)	9:392713	PF3D7_0908500*	conserved Plasmodium protein
PG0060-C.ERR019058	9(c)	9:392713	PF3D7_0908500*	conserved Plasmodium protein
PG0060-C.ERR019058	9(d)	9:374772	PFHG_00137	conserved hypothetical protein
PG0060-C.ERR019058	10(a)	13:2425469	PF3D7_1360700	SUMO ligase, putative
PG0060-C.ERR019058	10(b)	13:2458289	PF3D7_1360700	E3 SUMO-protein ligase PIAS, putative (PIAS)
PG0060-C.ERR019058	10(c)	13:2458289	PF3D7_1360700	E3 SUMO-protein ligase PIAS, putative (PIAS)

PG0060-C.ERR019058	10(d)	13:2425769	PF3D7_1360700*	SUMO ligase, putative
PG0063-C.ERR019060	11(a)	1:30339	PF3D7_0100100*	erythrocyte membrane protein 1, PfEMP1 (VAR)
PG0063-C.ERR019060	11(b)	2:922666	PF3D7_0223500*	erythrocyte membrane protein 1, PfEMP1 (VAR)
PG0063-C.ERR019060	12(a)	2:227	PF3D7_0200100	erythrocyte membrane protein 1, PfEMP1 (VAR)
PG0063-C.ERR019060	12(b)	1:613915	PF3D7_0115700*	erythrocyte membrane protein 1, PfEMP1 (VAR)
PG0063-C.ERR019060	12(c)	1:30503	PF3D7_0100100*	erythrocyte membrane protein 1, PfEMP1 (VAR)
PG0068-C.ERR019065	13(a)	8:196138	PF3D7_0803600	conserved Plasmodium protein
PG0068-C.ERR019065	13(b)	8:223392	PF3D7_0803600	conserved Plasmodium protein
PG0068-C.ERR019065	14	6:1299857	PF3D7_0631100	Plasmodium exported protein (PHISTb)
PG0068-C.ERR019065	15	12:2227873	PF3D7_1254800	rifin (RIF)
PG0067-C.ERR019073	16	13:700741	PF3D7_1316900	conserved Plasmodium protein
PG0067-C.ERR019073	17	5:1190881	PF3D7_0529100*	conserved Plasmodium protein
PG0067-C.ERR019073	18(a)	5:208676	PF3D7_0505000	conserved Plasmodium membrane protein
PG0067-C.ERR019073	18(b)	5:219779	PF3D7_0505000	conserved Plasmodium membrane protein
PG0071-C.ERR019074	19	7:767287	PF3D7_0717800*	conserved Plasmodium protein
PG0061-C.ERR019059	20	2:221	PF3D7_0200100	erythrocyte membrane protein 1, PfEMP1 (VAR)
PG0061-C.ERR019059	21	10:13	PF3D7_1000100	erythrocyte membrane protein 1, PfEMP1 (VAR)
PG0061-C.ERR019059	22	2:391186	PF3D7_0209500*	conserved Plasmodium protein
PG0054-C.ERR019062	23	11:495	PFHG_05272	conserved hypothetical protein
PG0054-C.ERR019062	24	9:901770	PF3D7_0922200	S-adenosylmethionine synthetase (SAMS)
PG0055-C.ERR019066	25(a)	7:518783	PF3D7_0711800	unspecified product
PG0055-C.ERR019066	25(b)	7:534499	PF3D7_0712100	unspecified product
PG0055-C.ERR019066	25(c)	7:534499	PF3D7_0712100	unspecified product
PG0055-C.ERR019066	25(d)	7:519201	PF3D7_0711800	unspecified product
PG0055-C.ERR019066	25(e)	7:519201	PF3D7_0711800	unspecified product
PG0055-C.ERR019066	25(f)	7:550446	PF3D7_0712400	erythrocyte membrane protein 1, PfEMP1 (VAR)
PG0055-C.ERR019066	25(g)	7:550446	PF3D7_0712400	erythrocyte membrane protein 1, PfEMP1 (VAR)
PG0055-C.ERR019066	25(h)	7:519363	PF3D7_0711800	unspecified product
PG0055-C.ERR019066	26(a)	11:1377073	PF3D7_1135200	conserved Plasmodium protein, pseudogene
PG0055-C.ERR019066	26(b)	14:2594198	PF3D7_1464100	conserved Plasmodium protein
PG0055-C.ERR019066	27	5:1190881	PF3D7_0529100*	conserved Plasmodium protein
PG0055-C.ERR019066	28(a)	11:121	PFHG_05272	conserved hypothetical protein

PG0055-C.ERR019066	28(b)	11:105	PFHG_05272	conserved hypothetical protein
PG0056-C.ERR019068	29	12:875380	PF3D7_1222000	conserved protein
PG0065-C.ERR019064	30	9:533496	PF3D7_0912400*	alkaline phosphatase, putative

Table 5.6: Putative NAHR events in the 3D7xHB3 cross

5.2.3 *De novo mutations in all crosses*

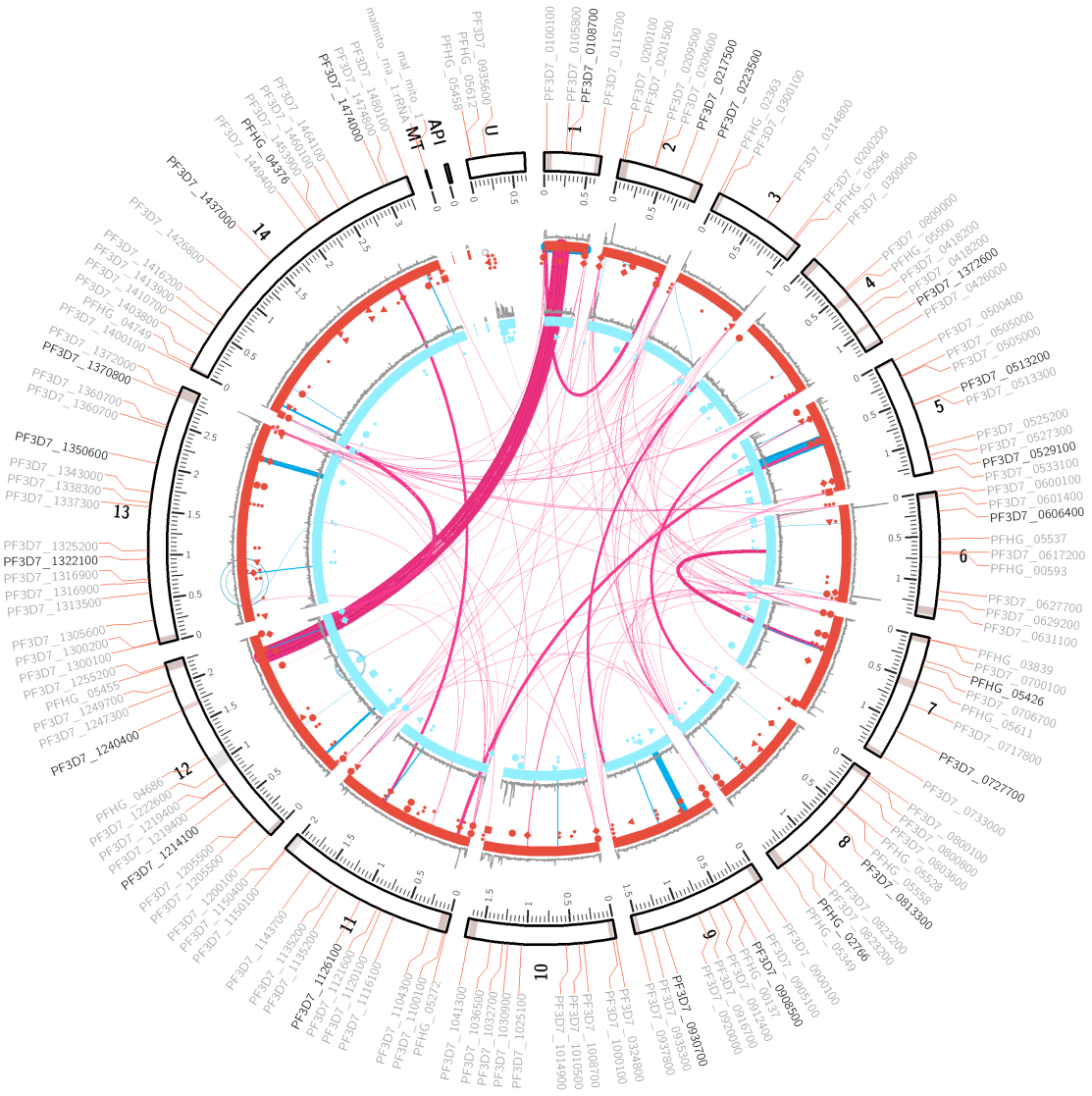

Figure 5.7: Combined *De novo* mutations calls across all progeny from the 3D7xHB3 cross.

All variants in all four crosses are shown in Figures 5.7 - 5.10, summarized in Table 5.8 (per-sample rates are shown in parentheses).

5.2.3.1 *Location bias*

As we observed earlier, many events seem to track closely with a measurement of sequence complexity, seemingly favoring regions of lower complexity. To dissect this further, we considered additive models of AT (GC) content, AT (GC) skew, CpG content, sequence complexity via Shannon, Wootton and Federhen, or Trifonov values, and se-

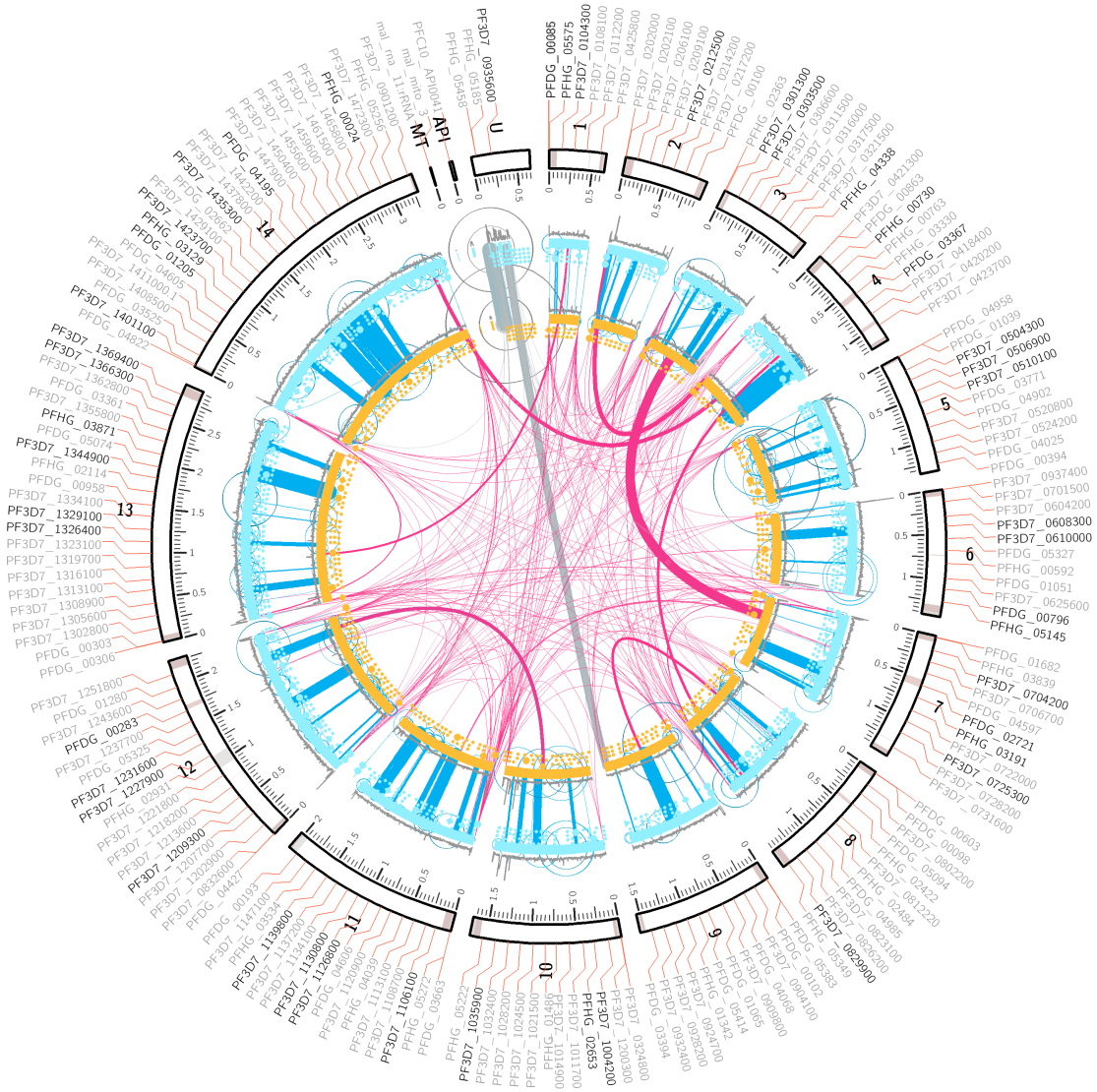

Figure 5.8: Combined *De novo* mutations calls across all progeny from the HB3xDD2 cross.

quence compression ratio. We extracted these features from all putative *de novo* variant regions that mapped somewhere in the genome. We excluded NAHR and GC events from our analysis, focusing solely on allelic variants. This yielded approximately 700 regions wherein the aforementioned metrics had been computed over 2,500 bp tiles. We then extracted 1,000 random feature tiles from the genome, taking care not to select any region that harbored a putative DNM. We then attempted a logistic regression and stepped through possible models, iteratively dropping features until the Akaike information cri-

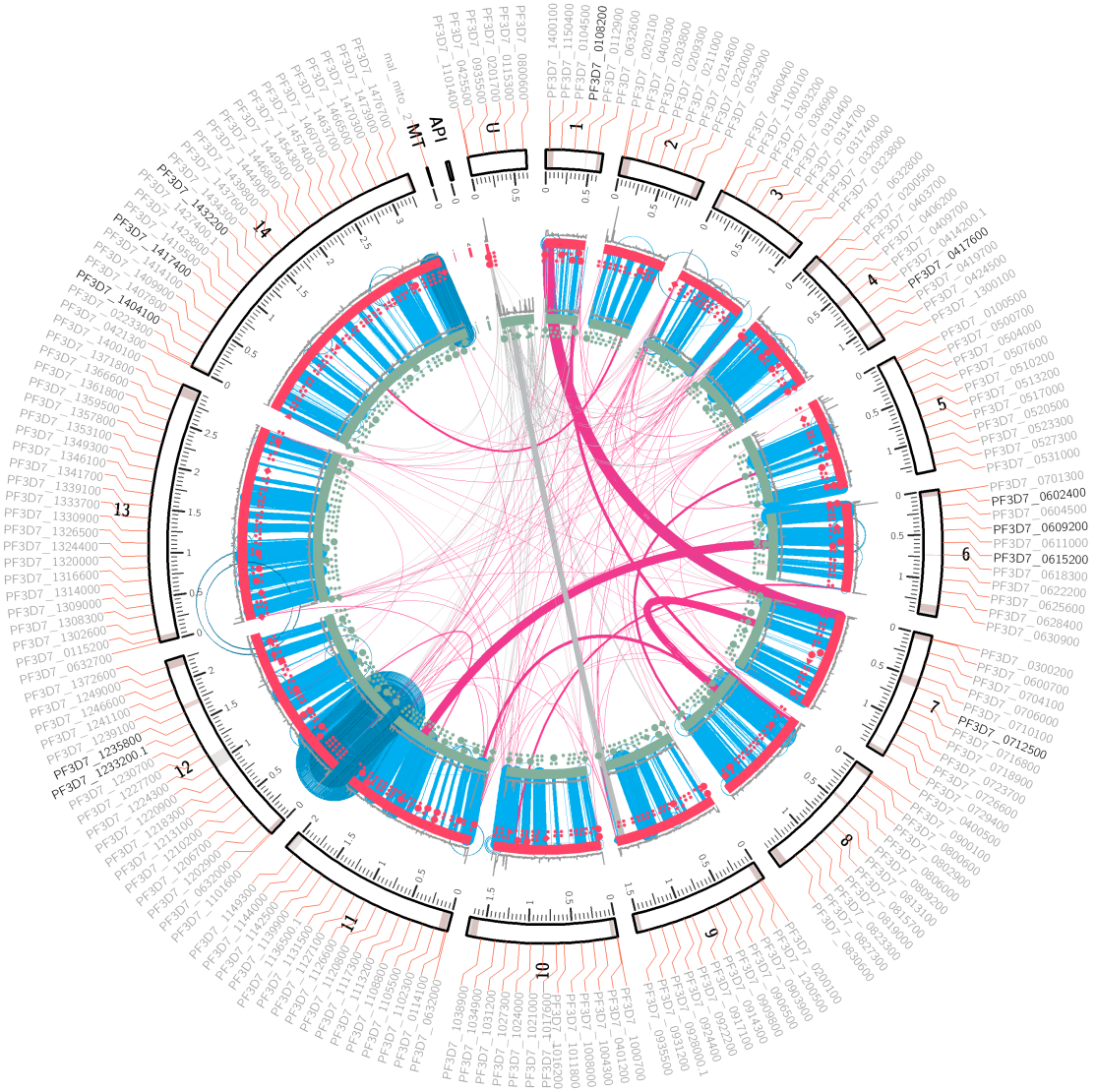

Figure 5.9: Combined *De novo* mutations calls across all progeny from the 7G8xGB4 cross.

terion (AIC) had been minimized. The final model was,

$$isDenovo\ at + ats + gcs + ce. \tag{5.3}$$

Details of the model are summarized in Table 5.8. According to the model, AT content, AT skew, and Shannon sequence entropy are significant predictors of where a DNM is likely to occur.

Table 5.7: Variants and rates of occurrence (in cross and per sample)

	3D7xHB3	HB3xDD2	7G8xGB4	803xGB4
Samples	20	36	26	33
SNP	38 (1.90)	179 (4.97)	57 (2.19)	120 (3.64)
Insertions	29 (1.45)	83 (2.31)	95 (3.65)	68 (2.06)
STR expansion	11 (0.55)	29 (0.81)	46 (1.77)	18 (0.55)
Tandem duplication	0 (0.00)	5 (0.14)	1 (0.04)	4 (0.12)
Other	18 (0.90)	49 (1.36)	48 (1.85)	46 (1.39)
Deletions	25 (1.25)	79 (2.19)	56 (2.15)	63 (1.91)
STR contraction	12 (0.60)	41 (1.14)	33 (1.27)	24 (0.73)
Other	13 (0.65)	38 (1.06)	23 (0.88)	39 (1.18)
MNPs	27 (1.35)	62 (1.72)	58 (2.23)	127 (3.85)
Inversion	0 (0.00)	0 (0.00)	4 (0.15)	0 (0.00)
Other	27 (1.35)	62 (1.72)	54 (2.08)	127 (3.85)
NAHR	30 (1.50)	161 (4.47)	177 (6.81)	218 (6.61)
GC	67 (3.35)	206 (5.72)	242 (9.31)	132 (4.00)

Table 5.8: Model parameters and significance

	Estimate	Std. Error	z value	Pr(>|z|)
(Intercept)	72.3701	8.6439	8.372	< 2e-16
at	-44.9120	4.9623	-9.051	< 2e-16
ats	-7.2731	0.8416	-8.642	< 2e-16
gcs	-0.9959	0.5699	-1.748	0.0805
ce	-42.4929	5.5050	-7.719	1.17e-14

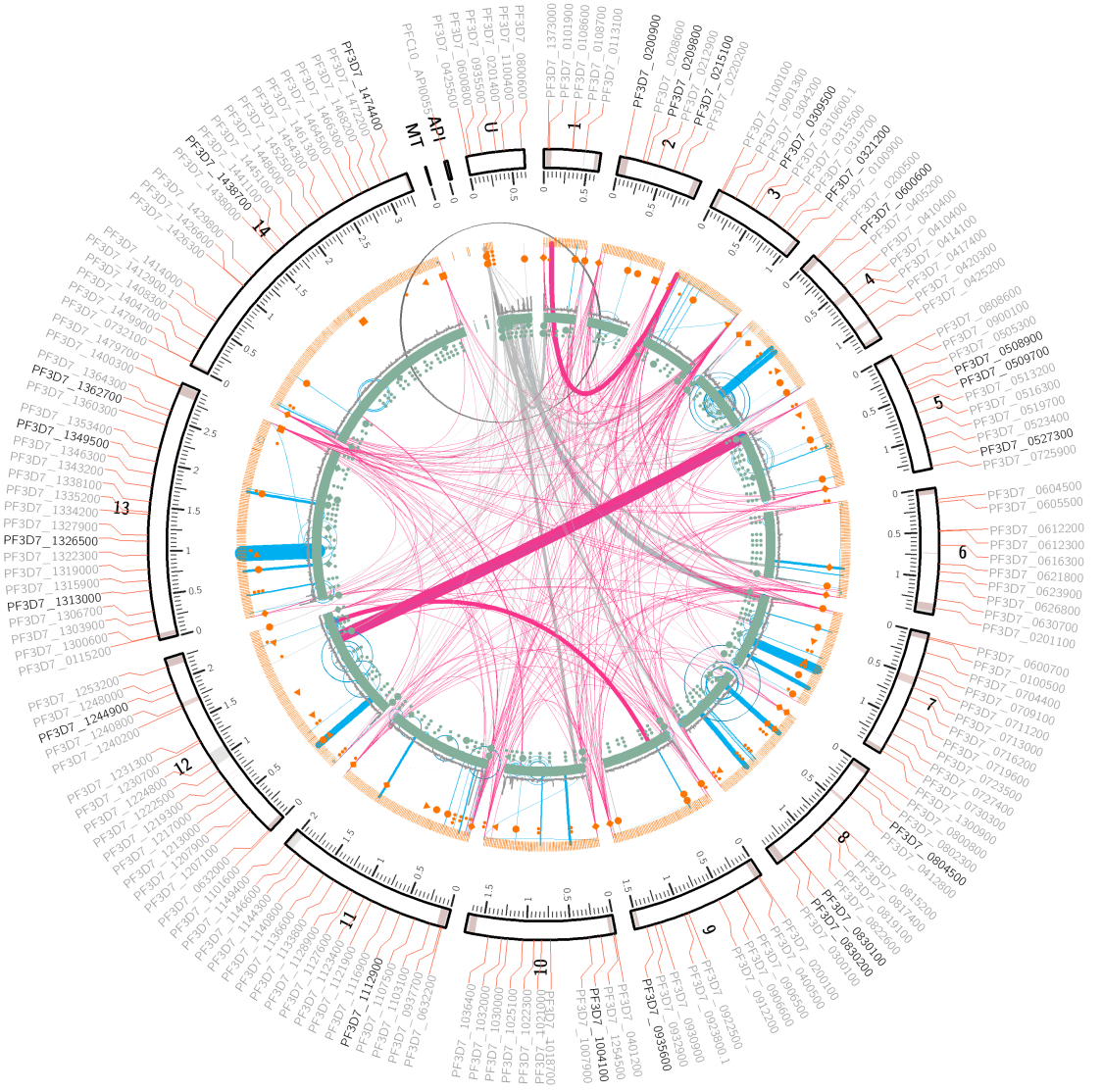

Figure 5.10: Combined *De novo* mutations calls across all progeny from the 803xGB4 cross.

6 *Pan troglodytes verus*

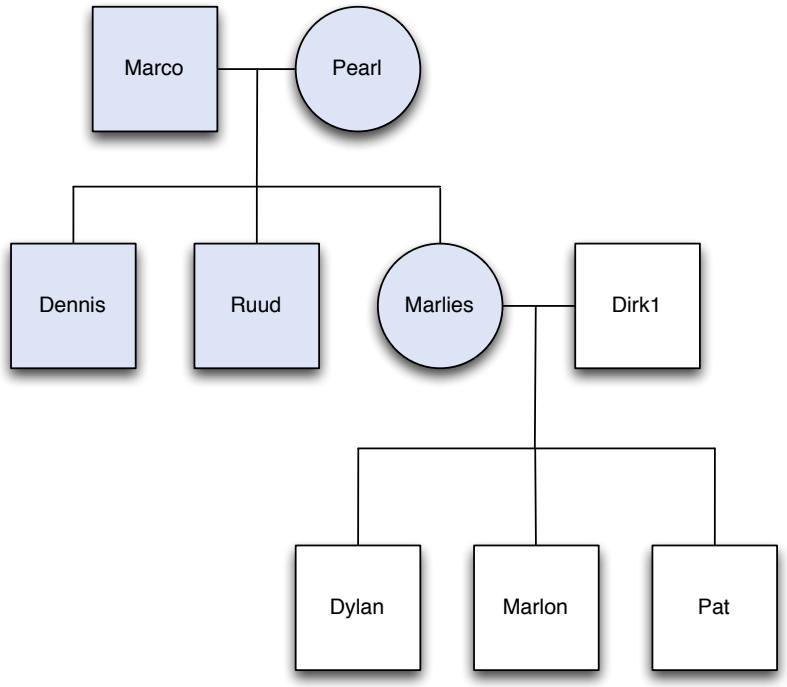

Figure 6.1: The three-generation chimpanzee pedigree. The highlighted quintet is discussed in this chapter.

Finally, we present our work on a second dataset: a quintet taken from a three-generation, nine member pedigree of West African chimpanzees (*Pan troglodytes verus*). The processed samples are highlighted in Figure 6.1. Venn et al. have previously examined this pedigree using reference-based methods for *de novo* variation discovery, reporting a substantial paternal age effect to the overall mutation rate.[21]

In many ways, the chimpanzee quartet is a more challenging dataset to process than the *falciparum* crosses. First, the genome is roughly two orders of magnitude larger; *Plasmodium falciparum* is approximately 23 Mbp, while *Pan troglodytes* is 3,300 Mbp (3.3 Gbp). Second, the genome is diploid rather than haploid, an additional challenge during variant detection as now our software must contend with the presence of heterozygotes. Third, we do not have draft-quality parental assemblies, and owing to the genome size, it is pro-

Table 6.1: Summary of *P. troglodytes* quintet data

	Marco	Pearl	Dennis	Ruud	Marlies
Platform			Illumina HiSeq 2000		
Read length (bp)			100		
Fragment size (bp)	369 ± 23	399 ± 31	377 ± 24	415 ± 27	383 ± 28
Coverage	60 ± 10	54 ± 8	35 ± 6	22 ± 3	29 ± 5
Cleaning threshold	10	9	8	4	6
Kmers					
dirty	$7.7e9$	$9.0e9$	$5.9e9$	$4.4e9$	$5.2e9$
clean	$2.6e9$	$2.7e9$	$2.5e9$	$2.7e9$	$2.6e9$
Novel kmers					
initial	-	-		348,374	121,834
confident	-	-		1,474	2,197
trusted	-	-		600	1,034

hibitively expensive to generate such data as we did in the previous chapter. We will be forced to rely solely on the Illumina data for the parents and children. Fourth, the chimpanzee reference genome is reported to be of lesser quality than the *falciparum* reference, misassemblies in which can contribute to false positive variant calls.[?] The chimpanzee assembly process employed a whole-genome shotgun sequencing approach yielding $5x$ coverage and 37,846 supercontigs that were aligned to the human reference build to reconstruct the autosomes and sex chromosomes.[59] The *falciparum* employed a whole-chromosome shotgun approach yielding approximately $14x$ coverage per chromosome. With myriad errors in the chimpanzee reference sequence, a method unbiased towards the reference sequence should prove quite useful. Finally, the coverage is substantially lower: $57x$ on average for the founders, $28x$ on average for the children, or one-half and one-third the coverage we had for samples in the previous chapter.

For precisely these reasons, the chimpanzee dataset is an important test-bed for our *de novo* mutation calling software. It permits a demonstration of our capacity to process much larger genomes than the *falciparum* parasite. Moreover, the problematic chimpanzee reference sequence and infeasibility of generating draft reference assemblies for the parents or children allow us to demonstrate the value of an approach that can leverage both, but requires neither.

6.1 Data processing

6.1.1 Initial data

We obtained the raw genomic sequencing data for the nine members of the pedigree. For simplicity, we chose to focus our efforts on three children in the F_1 generation: Dennis, Ruud, and Marlies. Their parents, Marco and Pearl, were sequenced to higher coverage. This should give us greater confidence in our ability to distinguish novel kmers, kmers present in the child but absent from the parents, from those only absent from the parental genomes due to issues with sequencing. The quintet is summarized in Table 6.1.

6.1.2 Sample processing

Precisely as we did for the *P. falciparum* samples in the previous chapter, we used the available Illumina data to construct the de Bruijn graph structures for each child with McCortex, using a kmer size of 47 bp and discarding bases with a quality score less than *Q*5. McCortex's automatic cleaning algorithm was applied to the dirty graph for each sample. We did not apply the paired-end read threading and contig emission steps as contigs were not required for our analysis.

6.1.3 Novel kmers

We produced a list of novel kmers per child in the manner described in Chapter 4, selecting kmers present in the child but absent in the parents ("initial" in Table 6.1), then applying coverage thresholds ("confident") and non-chimpanzee contamination checks ("trusted") to the resulting list[1].

6.2 De novo mutations in the P. troglodytes dataset

6.2.1 De novo mutations in a single sample

6.2.2 De novo mutations in all progeny

6.2.2.1 Mutational spectrum

6.2.2.2 Comparison to published calls

[1] Examining the results of the contamination check, it is evident that some samples contain small numbers of kmers that BLAST identifies as coming from human (hundreds) or gorilla (dozens). Given the evolutionary relationships between the three species, it is perhaps not unreasonable to allow these kmers into the analysis, as they may misattributed in the BLAST database. Instead, we have opted to remain conservative and exclude these from consideration.

7 Discussion

7.1 Lit review

7.1.1 Review of Kong et al., 2002

Augustine Kong et al. discuss a new genetic map of recombination rates using genotyping information from 869 individuals in 146 Icelandic families. This is the first such map made after the sequencing of the human genome, and is thus able to leverage the new reference sequence in order to correctly order the genotyped markers. It is a substantially higher-resolution map than provided by the former gold-standard, the Marshfield map. The Marshfield map contained data on only 188 meioses, whereas the Kong et al. map contained data on 1,257. The new map reveals marked differences in recombination rates between males and females (e.g. the recombination rate in female autosomes is a factor of 1.65 higher than that observed in males) for reasons beyond sequence features.

References

[1] World Health Organization. Antimicrobial Resistance, 2014.

[2] C Wang, K Takeuchi, L H Pinto, and R A Lamb. Ion channel activity of influenza A virus M2 protein: characterization of the amantadine block. *Journal of virology*, 67(9):5585–5594, September 1993.

[3] Martha I Nelson, Lone Simonsen, Cécile Viboud, Mark A Miller, and Edward C Holmes. The origin and global emergence of adamantane resistant A/H3N2 influenza viruses. *Virology*, 388(2):270–278, June 2009.

[4] Vegard Eldholm, Gunnstein Norheim, Bent von der Lippe, Wibeke Kinander, Ulf R Dahle, Dominique A Caugant, Turid Mannsåker, Anne T Mengshoel, Anne M Dyrhol-Riise, and Francois Balloux. Evolution of extensively drug-resistant Mycobacterium tuberculosis from a susceptible ancestor in a single patient. *Genome Biology*, 15(11):490, November 2014.

[5] Matthew T G Holden, Edward J Feil, Jodi A Lindsay, Sharon J Peacock, Nicholas P J Day, Mark C Enright, Tim J Foster, Catrin E Moore, Laurence Hurst, Rebecca Atkin, Andrew Barron, Nathalie Bason, Stephen D Bentley, Carol Chillingworth, Tracey Chillingworth, Carol Churcher, Louise Clark, Craig Corton, Ann Cronin, Jon Doggett, Linda Dowd, Theresa Feltwell, Zahra Hance, Barbara Harris, Heidi Hauser, Simon Holroyd, Kay Jagels, Keith D James, Nicola Lennard, Alexandra Line, Rebecca Mayes, Sharon Moule, Karen Mungall, Douglas Ormond, Michael A Quail, Ester Rabbinowitsch, Kim Rutherford, Mandy Sanders, Sarah Sharp, Mark Simmonds, Kim Stevens, Sally Whitehead, Bart G Barrell, Brian G Spratt, and Julian Parkhill. Complete genomes of two clinical Staphylococcus aureus strains: evidence for the rapid evolution of virulence and drug resistance. *Proceedings of the National Academy of Sciences of the United States of America*, 101(26):9786–9791, June 2004.

[6] D Walliker, I Quakyi, T Wellems, T McCutchan, A Szarfman, W London, L Corcoran, T Burkot, and R Carter. Genetic analysis of the human malaria parasite Plasmodium falciparum. *Science (New York, NY)*, 236(4809):1661–1666, June 1987.

[7] D S Peterson, D Walliker, and T E Wellems. Evidence that a point mutation in dihydrofolate reductase-thymidylate synthase confers resistance to pyrimethamine in falciparum malaria. *Proceedings of the National Academy of Sciences of the United States of America*, 85(23):9114–9118, December 1988.

[8] T E Wellems, L J Panton, I Y Gluzman, V E do Rosario, R W Gwadz, A Walker-Jonah, and D J Krogstad. Chloroquine resistance not linked to mdr-like genes in a Plasmodium falciparum cross. *Nature*, 345(6272):253–255, May 1990.

[9] A B Vaidya, O Muratova, F Guinet, D Keister, T E Wellems, and D C Kaslow. A genetic locus on Plasmodium falciparum chromosome 12 linked to a defect in mosquito-infectivity and male gametogenesis. *Molecular and biochemical parasitology*, 69(1):65–71, January 1995.

[10] T Furuya, J Mu, K Hayton, A Liu, J Duan, L Nkrumah, D A Joy, D A Fidock, H Fujioka, A B Vaidya, T E Wellems, and X z Su. Disruption of a Plasmodium falciparum gene linked to male sexual development causes early arrest in gametocytogenesis. *Proceedings of the National Academy of Sciences of the United States of America*, 102(46):16813–16818, November 2005.

[11] L H Freitas-Junior, E Bottius, L A Pirrit, K W Deitsch, C Scheidig, F Guinet, U Nehrbass, T E Wellems, and A Scherf. Frequent ectopic recombination of virulence factor genes in telomeric chromosome clusters of P. falciparum. *Nature*, 407(6807):1018–1022, October 2000.

[12] Michael F Duffy, Timothy J Byrne, Celine Carret, Alasdair Ivens, and Graham V Brown. Ectopic recombination of a malaria var gene during mitosis associated with an altered var switch rate. *Journal of molecular biology*, 389(3):453–469, June 2009.

[13] E W Myers. Toward simplifying and accurately formulating fragment assembly. *Journal of computational biology : a journal of computational molecular cell biology*, 2(2):275–290, 1995.

[14] Elaine R Mardis. A decade's perspective on DNA sequencing technology. *Nature*, 470(7333):198–203, February 2011.

[15] M C Schatz, A L Delcher, and S L Salzberg. Assembly of large genomes using second-generation sequencing. *Genome research*, 20(9):1165–1173, September 2010.

[16] Paul Flicek and Ewan Birney. Sense from sequence reads: methods for alignment and assembly. *Nature methods*, 6(11s):S6–S12, November 2009.

[17] Rasmus Nielsen, Joshua S Paul, Anders Albrechtsen, and Yun S Song. Genotype and SNP calling from next-generation sequencing data. *Nat Rev Genet*, 12(6):443–451, June 2011.

[18] N Woodford and M J Ellington. The emergence of antibiotic resistance by mutation. *Clinical Microbiology and Infection*, 13(1):5–18, 2007.

[19] Benjamin M Neale, Yan Kou, Li Liu, Avi Ma'ayan, Kaitlin E Samocha, Aniko Sabo, Chiao-Feng Lin, Christine Stevens, Li-San Wang, Vladimir Makarov, Paz Polak, Seungtai Yoon, Jared Maguire, Emily L Crawford, Nicholas G Campbell, Evan T Geller, Otto Valladares, Chad Schafer, Han Liu, Tuo Zhao, Guiqing Cai, Jayon Lihm, Ruth Dannenfelser, Omar Jabado, Zuleyma Peralta, Uma Nagaswamy, Donna Muzny, Jeffrey G Reid, Irene Newsham, Yuanqing Wu, Lora Lewis, Yi Han, Benjamin F Voight, Elaine Lim, Elizabeth Rossin, Andrew Kirby, Jason Flannick, Menachem Fromer, Khalid Shakir, Tim Fennell, Kiran Garimella, Eric Banks, Ryan Poplin, Stacey Gabriel, Mark Depristo, Jack R Wimbish, Braden E Boone, Shawn E Levy, Catalina Betancur, Shamil Sunyaev, Eric Boerwinkle, Joseph D Buxbaum, Edwin H Cook, Bernie Devlin, Richard A Gibbs, Kathryn Roeder, Gerard D Schellenberg, James S Sutcliffe, and Mark J Daly. Patterns and rates of exonic de novo mutations in autism spectrum disorders. *Nature*, 485(7397):242–245, May 2012.

[20] Donald F Conrad, Jonathan E M Keebler, Mark A DePristo, Sarah J Lindsay, Yujun Zhang, Ferran Casals, Youssef Idaghdour, Chris L Hartl, Carlos Torroja, Kiran V Garimella, Martine Zilversmit, Reed Cartwright, Guy A Rouleau, Mark Daly, Eric A Stone, Matthew E Hurles, Philip Awadalla, and 1000 Genomes Project. Variation in genome-wide mutation rates within and between human families. *Nature genetics*, 43(7):712–714, July 2011.

[21] Oliver Venn, Isaac Turner, Iain Mathieson, Natasja de Groot, Ronald Bontrop, and Gil McVean. Strong male bias drives germline mutation in chimpanzees. *Science (New York, NY)*, 344(6189):1272–1275, June 2014.

[22] Wigard P Kloosterman, Laurent C Francioli, Fereydoun Hormozdiari, Tobias Marschall, Jayne Y Hehir-Kwa, Abdel Abdellaoui, Eric-Wubbo Lameijer, Matthijs H Moed, Vyacheslav Koval, Ivo Renkens, Markus J van Roosmalen, Pascal Arp, Lennart C Karssen, Bradley P Coe, Robert E Handsaker, Eka D Suchiman, Edwin Cuppen, Djie T Thung, Mitch McVey, Michael C Wendl, Andre Uitterlinden, Cornelia M van Duijn, Morris Swertz, Cisca Wijmenga, Gertjan van Ommen, P Eline Slagboom, Dorret I Boomsma, Alexander Schönhuth, Evan E Eichler, Paul I W

de Bakker, Kai Ye, and Victor Guryev. Characteristics of de novo structural changes in the human genome. *Genome research*, page gr.185041.114, 2015.

[23] Laurent C Francioli, Paz P Polak, Amnon Koren, Androniki Menelaou, Sung Chun, Ivo Renkens, Cornelia M van Duijn, Morris Swertz, Cisca Wijmenga, Gertjan van Ommen, P Eline Slagboom, Dorret I Boomsma, Kai Ye, Victor Guryev, Peter F Arndt, Wigard P Kloosterman, Paul I W de Bakker, and Shamil R Sunyaev. Genome-wide patterns and properties of de novo mutations in humans. *Nature genetics*, 47(7):822–826, May 2015.

[24] Mark A DePristo, Eric Banks, Ryan Poplin, Kiran V Garimella, Jared R Maguire, Christopher Hartl, Anthony A Philippakis, Guillermo del Angel, Manuel A Rivas, Matt Hanna, Aaron McKenna, Tim J Fennell, Andrew M Kernytsky, Andrey Y Sivachenko, Kristian Cibulskis, Stacey B Gabriel, David Altshuler, and Mark J Daly. A framework for variation discovery and genotyping using next-generation DNA sequencing data. *Nature genetics*, 43(5):491–498, May 2011.

[25] Andy Rimmer, Hang Phan, Iain Mathieson, Zamin Iqbal, Stephen R F Twigg, Andrew O M Wilkie, Gil McVean, and Gerton Lunter. Integrating mapping-, assembly- and haplotype-based approaches for calling variants in clinical sequencing applications. *Nature genetics*, 46(8):912–918, July 2014.

[26] Eric S Lander and Michael S Waterman. Genomic mapping by fingerprinting random clones: A mathematical analysis. *Genomics*, 2(3):231–239, April 1988.

[27] Zamin Iqbal, Mario Caccamo, Isaac Turner, Paul Flicek, and Gil McVean. De novo assembly and genotyping of variants using colored de Bruijn graphs. *Nature genetics*, 44(2):226–232, February 2012.

[28] Malcolm J Gardner, Neil Hall, Eula Fung, Owen White, Matthew Berriman, Richard W Hyman, Jane M Carlton, Arnab Pain, Karen E Nelson, Sharen Bowman, Ian T Paulsen, Keith James, Jonathan A Eisen, Kim Rutherford, Steven L Salzberg, Alister Craig, Sue Kyes, Man-Suen Chan, Vishvanath Nene, Shamira J Shallom, Bernard Suh, Jeremy Peterson, Sam Angiuoli, Mihaela Pertea, Jonathan Allen, Jeremy Selengut, Daniel Haft, Michael W Mather, Akhil B Vaidya, David M A Martin, Alan H Fairlamb, Martin J Fraunholz, David S Roos, Stuart A Ralph, Geoffrey I McFadden, Leda M Cummings, G Mani Subramanian, Chris Mungall, J Craig Venter, Daniel J Carucci, Stephen L Hoffman, Chris Newbold, Ronald W Davis, Claire M Fraser, and Bart Barrell. Genome sequence of the human malaria parasite Plasmodium falciparum. *Nature*, 419(6906):498–511, October 2002.

[29] C Aurrecoechea, J Brestelli, B P Brunk, J Dommer, S Fischer, B Gajria, X Gao, A Gingle, G Grant, O S Harb, M Heiges, F Innamorato, J Iodice, J C Kissinger, E Kraemer, W Li, J A Miller, V Nayak, C Pennington, D F Pinney, D S Roos, C Ross, C J Stoeckert, C Treatman, and H Wang. PlasmoDB: a functional genomic database for malaria parasites. *Nucleic acids research*, 37(Database):D539–D543, January 2009.

[30] Heng Li. Aligning sequence reads, clone sequences and assembly contigs with BWA-MEM. March 2013.

[31] Aaron McKenna, Matthew Hanna, Eric Banks, Andrey Sivachenko, Kristian Cibulskis, Andrew Kernytsky, Kiran Garimella, David Altshuler, Stacey Gabriel, Mark Daly, and Mark A DePristo. The Genome Analysis Toolkit: a MapReduce framework for analyzing next-generation DNA sequencing data. *Genome research*, 20(9):1297–1303, September 2010.

[32] Antoine Claessens, William L Hamilton, Mihir Kekre, Thomas D Otto, Adnan Faizullabhoy, Julian C Rayner, and Dominic Kwiatkowski. Generation of Antigenic Diversity in Plasmodium falciparum by Structured Rearrangement of Var Genes During Mitosis. *PLoS genetics*, 10(12):e1004812, December 2014.

[33] Thomas S Rask, Daniel A Hansen, Thor G Theander, Anders Gorm Pedersen, and Thomas Lavstsen. Plasmodium falciparum Erythrocyte Membrane Protein 1 Diversity in Seven Genomes – Divide and Conquer. *PLoS computational biology*, 6(9):e1000933, September 2010.

[34] Mark J P Chaisson, Richard K Wilson, and Evan E Eichler. Genetic variation and the de novo assembly of human genomes. *Nature Reviews Genetics*, 16(11):627–640, November 2015.

[35] Petr Danecek, Adam Auton, Goncalo Abecasis, Cornelis A Albers, Eric Banks, Mark A DePristo, Robert Handsaker, Gerton Lunter, Gabor Marth, Stephen T Sherry, Gilean McVean, Richard Durbin, and 1000 Genomes Project Analysis Group. The Variant Call Format and VCFtools. *Bioinformatics (Oxford, England)*, June 2011.

[36] Luc Devroye. *Non-Uniform Random Variate Generation*. Springer Science & Business Media, New York, NY, November 2013.

[37] Alistair Miles, Zamin Iqbal, Paul Vauterin, Richard Pearson, Susana Campino, Michel Theron, Kelda Gould, Daniel Mead, Eleanor Drury, John O'Brien, Valentin Ruano Rubio, Bronwyn MacInnis, Jonathan Mwangi, Upeka Samarakoon,

Lisa Ranford-Cartwright, Michael Ferdig, Karen Hayton, Xinzhuan Su, Thomas Wellems, Julian Rayner, Gil McVean, and Dominic Kwiatkowski. Genome variation and meiotic recombination in Plasmodium falciparum: insights from deep sequencing of genetic crosses. *bioRxiv*, page 024182, August 2015.

[38] Thomas S Rask, Daniel A Hansen, Thor G Theander, Anders Gorm Pedersen, and Thomas Lavstsen. Plasmodium falciparum erythrocyte membrane protein 1 diversity in seven genomes–divide and conquer. *PLoS computational biology*, 6(9), 2010.

[39] Susan M Kraemer and Joseph D Smith. A family affair: var genes, PfEMP1 binding, and malaria disease. *Current Opinion in Microbiology*, 9(4):374–380, August 2006.

[40] Heng Li, Bob Handsaker, Alec Wysoker, Tim Fennell, Jue Ruan, Nils Homer, Gabor Marth, Goncalo Abecasis, Richard Durbin, and 1000 Subgroup. The Sequence Alignment/Map format and SAMtools. *Bioinformatics (Oxford, England)*, 25(16):2078–2079, August 2009.

[41] H Bao, H Guo, J Wang, R Zhou, X Lu, and S Shi. MapView: visualization of short reads alignment on a desktop computer. *Bioinformatics (Oxford, England)*, 25(12):1554–1555, May 2009.

[42] James T Robinson, Helga Thorvaldsdóttir, Wendy Winckler, Mitchell Guttman, Eric S Lander, Gad Getz, and Jill P Mesirov. Integrative genomics viewer. *Nature biotechnology*, 29(1):24–26, January 2011.

[43] Iain Milne, Gordon Stephen, Micha Bayer, Peter J A Cock, Leighton Pritchard, Linda Cardle, Paul D Shaw, and David Marshall. Using Tablet for visual exploration of second-generation sequencing data. *Briefings in bioinformatics*, 14(2):193–202, March 2013.

[44] Helga Thorvaldsdóttir, James T Robinson, and Jill P Mesirov. Integrative Genomics Viewer (IGV): high-performance genomics data visualization and exploration. *Briefings in bioinformatics*, 14(2):178–192, March 2013.

[45] Isaac Turner. McCortex Workflow Examples. November 2015.

[46] Daphne Koller and Nir Friedman. *Probabilistic Graphical Models*. Principles and Techniques. MIT Press, 2009.

[47] N G Bruijn. *A combinatorial problem*. ... Nederlandse Akademie van Wetenschappen. Series A, 1946.

[48] John Hopcroft and Robert Tarjan. Efficient algorithms for graph manipulation, 1971.

[49] S F Altschul, W Gish, W Miller, E W Myers, and D J Lipman. Basic local alignment search tool. *Journal of molecular biology*, 215(3):403–410, October 1990.

[50] E W Dijkstra. A note on two problems in connexion with graphs. *Numerische mathematik*, 1(1):269–271, 1959.

[51] Karen Hayton, Deepak Gaur, Anna Liu, Jonathan Takahashi, Bruce Henschen, Subhash Singh, Lynn Lambert, Tetsuya Furuya, Rachel Bouttenot, Michelle Doll, Fatima Nawaz, Jianbing Mu, Lubin Jiang, Louis H Miller, and Thomas E Wellems. Erythrocyte Binding Protein PfRH5 Polymorphisms Determine Species-Specific Pathways of Plasmodium falciparum Invasion. *Cell Host & Microbe*, 4(1):40–51, January 2008.

[52] Chen-Shan Chin, David H Alexander, Patrick Marks, Aaron A Klammer, James Drake, Cheryl Heiner, Alicia Clum, Alex Copeland, John Huddleston, Evan E Eichler, Stephen W Turner, and Jonas Korlach. Nonhybrid, finished microbial genome assemblies from long-read SMRT sequencing data. *Nature methods*, 10(6):563–569, June 2013.

[53] Martin I Krzywinski, Jacqueline E Schein, Inanc Birol, Joseph Connors, Randy Gascoyne, Doug Horsman, Steven J Jones, and Marco A Marra. Circos: An information aesthetic for comparative genomics. *Genome research*, 19(9):1639–1645, June 2009.

[54] C E Shannon. A mathematical theory of communication. *Bell System Technical Journal, The*, 27(3):379–423, July 1948.

[55] E N Trifonov. Making sense of the human genome. *Structure and methods : proceedings of the Sixth Conversation in the Discipline Biomolecular Stereodynamics held at the State University of New York at Albany, June 6-10, 1989 / edited by R.H. Sarma & M.H. Sarma*, 1990.

[56] J C Wootton and S Federhen. Analysis of compositionally biased regions in sequence databases. *Methods in enzymology*, 266:554–571, 1996.

[57] Adam F Sander, Thomas Lavstsen, Thomas S Rask, Michael Lisby, Ali Salanti, Sarah L Fordyce, Jakob S Jespersen, Richard Carter, Kirk W Deitsch, Thor G Theander, Anders Gorm Pedersen, and David E Arnot. DNA secondary structures are associated with recombination in major Plasmodium falciparum variable surface antigen gene families. *Nucleic acids research*, November 2013.

[58] Eric Talevich, Amar Mirza, and Natarajan Kannan. Structural and evolutionary divergence of eukaryotic protein kinases in Apicomplexa. *BMC Evolutionary Biology*, 11(1):1, November 2011.

[59] The Chimpanzee Sequencing and Analysis Consortium and Chimpanzee Sequencing and Analysis Consortium. Initial sequence of the chimpanzee genome and comparison with the human genome. *Nature*, 437(7055):69–87, August 2005.